CELL-BASED VASCULAR THERAPEUTICS FOR BONE REGENERATION

A Dissertation
Presented to
The Academic Faculty

by

Marissa Ashley Ruehle

In Partial Fulfillment
of the Requirements for the Degree
Doctor of Philosophy in the
Wallace H. Coulter Department of Biomedical Engineering

Georgia Institute of Technology & Emory University
August 2019

CELL-BASED VASCULAR THERAPEUTICS FOR ENHANCED BONE REGENERATION

Approved by:

Dr. Robert E. Guldberg, Advisor
Phil and Penny Knight Campus for Accelerating Scientific Impact
University of Oregon

Dr. Nick J. Willett, Advisor
School of Medicine
Emory University

Dr. Joel D. Boerckel
Perelman School of Medicine
University of Pennsylvania

Dr. Andrés J. García
George W. Woodruff School of Mechanical Engineering
Georgia Institute of Technology

Dr. James B. Hoying
Chief Scientist
Advanced Solutions – Life Sciences

Dr. Rebecca D. Levit
School of Medicine
Emory University

Date Approved: May 6, 2019

To my family, Jamie, Steve, Ceanna, and Betty, for preparing me for and supporting me through this journey, and to Travis for walking with me every step of the way.

ACKNOWLEDGEMENTS

I am immensely fortunate to have an acknowledgements section that is so long but so easy to write. This thesis could not have existed without the technical, scientific, and moral support provided by the individuals below – thank you all so much.

First and foremost, I thank my thesis advisors, Bob Guldberg and Nick Willett. Bob and Nick took me on as a new student to work on a project involving osteopontin knockout MSCs – a topic not even remotely related to this thesis. I appreciate now even more than I did at the time how lucky I was to be given the freedom to explore an initially unfunded project following my own interests. From Bob, I have learned how to see my work through a wider lens and how to let the remaining unanswered questions drive research forward. Bob always allowed me to consider which questions we would answer and how best to answer them; these are invaluable skills I know I gained from Bob's mentorship style. From Nick, I have learned how to place my research into a more clinical context, a skill I know will be valuable moving forward in my career. Nick always made himself available for questions and feedback, and I am grateful that I could always count on Mondays and Thursdays for guidance and/or general conversation. Nick has placed great emphasis on creating a cohesive, supportive lab culture, and I am honored to be the first graduate of the Willett Lab!

This thesis ultimately took on a new and bigger life than it could have without the input of my thesis committee, each of whom has been exceptionally involved and has been happy to meet with me outside the formal committee updates. Joel Boerckel led the study that motivated the third aim of my thesis and has been a wonderful resource to incorporate

the findings of his original study and his newer work into mine. Joel's YAP/TAZ expertise was invaluable, and even more so were his excitement and encouragement in discussing hypotheses, results, and future directions. Andrés García provided his biomaterials expertise in Aim 2 of the thesis, and I am grateful that he challenged me to answer deeper questions in Aim 3 than I originally proposed. Despite his incredibly busy schedule, Andrés was always happy to talk about experimental design and troubleshooting (a lot of troubleshooting), and his ability to remember the details of my previous experiments even in an impromptu hallway chat has never ceased to impress me. Jay Hoying developed the adipose-derived microvascular fragments system this entire thesis relied upon. Jay's expertise in cardiovascular physiology and in the subtleties of this model have been incredible resources in guiding experimental design and data interpretation. As the only MD on the committee, Rebecca Levit continually encouraged me to think about my project in terms of clinical relevance, and this thesis has benefitted from her valuable perspective.

To my lab members, thank you for the innumerable hours spent on practice presentations and in the surgical suite and for being such a fantastic group of people to work with. Fabrice Bernard said it best: "when you're in two labs, you have twice as many meetings but twice as many friends." It has been inspiring to watch Guldberg lab members graduate and begin the next steps of their lives, and it has been a joy to watch the Willett lab grow and take form. Alice Li was instrumental in laying the groundwork for what would become this thesis, and my fellow Texas Longhorn introduced me to some delicious food in Atlanta. Ashley Allen trained me in the ways of Guldberg lab cell culture and has given me tons of advice about grad school, hiking Half Dome, and life after grad school – all while making wherever she is fun with her infectious bubbliness. Lauren Priddy was an

excellent desk neighbor, and it has been so fun to see her (and her students!) at conferences throughout the years since she graduated. Marian Hettiaratchi shared proposal and thesis documents with me and singlehandedly increased the average niceness of the lab by about ten-fold; I know her kindness and biomaterials expertise will make her a coveted advisor very soon. David Reece brought his positive energy to the lab, and sometimes brought baby Jane too! Olivia Burnsed and I joined the Guldberg lab at the same time, which was during her third year of the program, and she was a great example of what you can learn in just a few years of grad school. Jason Wang answered many an email from me about perfusions and blood draws, even after I killed the pepper plants he gave me. Brennan Torstrick always asked helpful questions in lab meetings, and it has been fun to continue seeing him post-graduation at lab social events in Atlanta. Albert Cheng taught me nearly all the bone regeneration analysis techniques fundamental to our lab and could always be relied on for help inside or outside of the lab; he was a great Metropolis neighbor, too. Albert was part of the Guldberg lab through 90% of my PhD, and the lab hasn't been the same without him! Giuli Salazar-Noratto brought her lively spirit to our lab and was a great friend. We made the back row of the lair the best row, and it has been much quieter now that she is living her best life in Paris. Lina Mancipe-Castro brightened the lab with music and is an excellent singer; days in the TC room with her were significantly more fun with her there too. Lina is also the authority on free food on the Georgia Tech campus. Ryan Akman helped get the static compression system used in Aim 3 off the ground while I was doing an internship, which I very much appreciate. Ryan was always willing to help, which is best exemplified by the fact that he consistently continued to help with our surgeries even after joining the Hollister lab. Casey Vantucci joined Giuli and me in back-row-best-row

and quickly become a close friend. I am honored that Tina Guldberg was convinced we are sisters or at least roommates, and there is no one else I would take Taco Bell out of the trash can for after accidentally throwing it away (still sorry about that). I appreciate Casey's help with FlowJo, letting me live vicariously through Camden, and especially the many rants and laughs we shared. Gilad Doron was my fellow Guldberg lab CMaT person, and I am very grateful that he picked up the CMaT leadership mantle from me. Ramesh Subbiah is best summarized by a Brennan quote from ORS 2018: "Do you wake up and immediately start giggling?" Ramy's kindness and constant smile were wonderful additions to the lab, and he is great chef of Tamil cuisine! Angela Lin helped me immensely with all things mechanical testing and μCT (more about that later) and showed me the ropes of working with rats. We have missed her in Atlanta, but Oregon is lucky to have her. It was so fun to meet Denise Niell and Kelly Hyland at ORS in Austin, and I know the Oregon Guldberg Lab is in good hands with them. Brett Klosterhoff has been a great labmate in both the Guldberg and Willett labs. We stepped through all the major milestones of the PhD at the same time, which made for good commiseration. Brett was always willing to help with 3D printing, machining, etc. and asked perceptive questions through his lens as a mechanical engineer. Brett was also a great friend, and I have enjoyed getting to know both him and Kayla. I appreciate that Fabrice Bernard drove the Georgia Tech contingent to lab meetings every week, and his sense of humor (ask him if he's vegan today) brightened each of those car rides and the lab in general. Shannon Anderson has great taste in podcasts and can kick a mean field goal, both of which have been subjects of great conversation and great fun. Fabrice and Shannon have both been more than willing to help with surgeries, which was especially appreciated after the Guldberg lab move. Jay McKinney is the newest graduate

student of the group, and he is already off to a great start. Thanh Doan taught me how to work with RNA and always asked questions in lab meeting that helped consolidate and solidify the big picture story. Hyunhee Anh was a friendly, smiling presence in the lab, and she was an above-and-beyond conference roommate. Emily Devereaux was always willing to help and saved me several trips to (and parking at) the VA, which I very much appreciate. Jarred Kaiser has brought his unique skillset to the lab, which will enable the exploration of some new directions. He also has a wonderful sense of humor that kept me laughing. I am immeasurably grateful that I found not one but two groups of incredibly helpful, supportive, and wonderful labmates.

I owe special thanks to Laxmi Krishnan and Hazel Stevens. It is not an exaggeration to say that this thesis was only possible because of Laxmi. He taught me everything I know about microvessels, secured funding for all three of my aims at some level, and was a blend of third advisor, collaborator, and friend. Laxmi was always willing to help in whatever way I needed, from being an extra pair of hands in the lab to lengthy discussions about how to choose which arm of a scientific question to answer. I am immeasurably grateful to him. Hazel kept the lab running smoothly, and I can say that even more confidently now that I have absorbed some of those responsibilities. More than that though, Hazel was a trusted set of first eyes on many lab meeting presentations, publications, and experimental designs. Getting to work closely with Hazel on our MSC aggregate project was a privilege, and I enjoyed our trips to Athens in the Mini. Most of all, Hazel has been a dear friend throughout my entire PhD. I am so thankful that she is still on campus for coffee breaks, although I miss being able to just stop by her office and monopolize unscheduled time (we might both be more productive now, though…). I am fortunate that Hazel and Laxmi were with me

through the first years of my PhD, and they have both continued to help me via (sometimes panicked) email and text message. While I have missed them both here at the end, I am confident in myself as an independent researcher in large part because of what I learned from them.

I had the good fortune to mentor four excellent undergraduate students during my PhD. Yuyan Wang joined the lab her senior year, and I wish I could take more credit for her abilities to work independently, handle unexpected results, and ask astute questions that impress even Hazel. She truly led the flow cytometry work included in Aim 1 as her undergraduate thesis work and is now a graduate student at Cornell. Emily Eastburn also came to me as an experienced researcher, and she has been a trusted partner in all of the imaging and associated analysis in Aim 3 as a PURA recipient. Emily thinks critically about methods and results, making her remarkably independent in the lab. Luckily for me, our graduations are synchronous, and she is off to Penn in the fall. I know she will do great things in the Boerckel lab. Peyton Holzworth joined the lab as a high school student and has continued working with us through her demanding freshman year at Georgia Tech. Peyton and I have shared many conversations and laughs in the tissue culture room, and I am excited to see all of what she will accomplish. Joann Gu, a fellow Texas Longhorn, worked with me as a summer student through the SURE program. She jumped into a project that was completely unfamiliar to her with enthusiasm and helped me establish the methods for working with our then-new dynamic loading system. She also took the initiative to learn mesenchymal stem cell culture basics. Joann is also off to graduate school in the fall and will be an asset to Berkeley's bioengineering program.

Rose Brito, Vivian Johnson, and Julie Langenberg have helped me navigate Bob's calendar, which is no small feat. I especially thank Rose, who also helped find those rare moments when both Bob and Andrés are free, and for continuing to help the Guldberg lab students after it was no longer her formal responsibility. She has taken excellent care of us just because she cares, and we are all grateful.

The animal work in this thesis would not have been possible without the highly capable PRL staff we are lucky to have at Georgia Tech, and it certainly would not have been nearly as enjoyable either. I appreciate the many hours of work they do to enable our research, and they always brightened my day – even the very, very long surgery days. I give an extra special shout-out to Altair, Andrea, Ogeda, and Rebecca.

The IBB core staff have also enabled this research. I and my undergraduate mentees have logged many, many hours on the confocal microscope thanks to Andrew Shaw. Andrew always had ideas of how to meet the specific imaging challenges of my project and was happy to help me learn how to implement them. Aaron Lifland was also happy to help me explore new imaging options. Sommer Durham patiently answered all my many questions about flow cytometry and did it all with a smile. Dalia Gulick enabled the gene expression arrays in Aim 3, which opened new directions for the project. Angela Lin always replied to my CT and mechanical testing texts, and without her the Scanco systems would be mysteries to us all. Special thanks to Angela for verbally telling me how to disassemble the Viva while she was doing surgery so I could rescue a stowaway…

Laura Paige adopted me as one of her students, and she always knew the answers to my questions for not only my department that she doesn't actually work for but also

several others. Laura goes above and beyond for her students (even the adopted ones). For example, when the IBB printer was down, she printed my poster for a conference in MRDC and walked with me to pick it up, even though she had walked tens of miles for breast cancer the weekend before. She also frequently emailed me about leftover free food in the IBB kitchen and came to work the day after a trans-Atlantic flight to come to my defense. I am grateful to Laura most of all for sharing many laughs with me in her office; they provided an outlet for joy on the good days and a comfort on the days when I could have either laughed or cried.

A number of other people have helped shape this thesis and my PhD experience more broadly. Jeff Weiss has been an exceptional collaborator, and he led us to the idea of decorin-supplemented collagen gels developed and utilized in Aims 2-3. He and his student Steven LaBelle have contributed to subsequent experiments through our monthly conference calls. Todd McDevitt and Bob Nerem's NSF Stem Cell Biomanufacturing IGERT funded me for the first three years. Krish Roy and Johnna Temenoff asked me to co-lead the inaugural CMaT student leadership council, which I was honored to do. Krish also deserves some of the credit for bringing Georgia Tech to the top of my list of graduate schools to apply to. He was an excellent professor to TA for, and he has been happy to discuss my future career plans. Colly Mitchell and Floyd Wood helped make my time as a BBUGS education and outreach chair successful, especially with Buzz on Biotech.

Finally, this thesis was enabled by my family. I could write a thesis-length document just to express gratitude to them, but I will keep it brief here. I credit my interest in biological systems to my mom, who always encouraged me to think about the "why" and "how" of a variety of health-related questions, both human and veterinary, and to

always question deeply. I credit my (eventual) love of math to my dad, who encouraged me from a young age to see the power of numbers and still impresses me with his mental math skills. Both parents helped me develop the curiosity and pragmatism that led me to engineering. They have always been endlessly supportive of both me and my sister, Ceanna, in every way, encouraging us to follow our interests and doing all they can to help us succeed. My parents have listened with interest to the details of every experiment that went especially well or exceedingly poorly, including the minutia of vascular perfusion; see the Appendix A.4 to become more impressed. They and Ceanna (and Nacho) have made every visit home a cherished reprieve. I am so proud of Ceanna, who has sought out opportunities to explore her numerous passions at UT and truly excelled at all of them. I am so excited to see what she will do next, but I already know that whatever it is will be exceptional. I also thank Travis's parents, Jannelle and Gary, for making their home in Austin feel like home to me too, for sharing their time in California with me, and for welcoming me into their family with open arms. Finally, I am so fortunate to have had Travis as my partner through this journey. He has listened to all the ups and downs of grad school and has been my personal MATLAB wizard. More importantly, Travis has served as a constant reminder that life is so much bigger than this PhD. While the 2000 mile, three time zone distance has been non-ideal, I am so proud of what we have both achieved in these years, and I treasure the adventures it has enabled us to have. That said, I am boundlessly excited to live in the same place (!!!) and for all our adventures yet to come.

TABLE OF CONTENTS

LIST OF TABLES

LIST OF FIGURES

LIST OF SYMBOLS AND ABBREVIATIONS

α MEM	Minimum Essential Medium Eagla α Modification
Ang	Angiopoietin
ANOVA	Analysis of Variance
αSMA	Alpha Smooth Muscle Actin
BMP	Bone Morphogenetic Protein
BTE	Bone Tissue Engineering
cAMP	Cyclic Adenosine Monophosphate
cDNA	Complementary Deoxyribonucleic Acid
CtsK	Cathepsin K
DAPI	4′,6-diamidino-2-phenylindole
DBM	Demineralized Bone Matrix
DCN	Decorin
Dll4	Delta-like Ligand 4
DMB	Dimethylmethylene Blue
DMEM	Dulbecco's Modified Eagle Medium
DMSO	Dimethyl sulfoxide
EC	Endothelial Cell
ECM	Extracellular Matrix
EdU	5-ethynyl-2′-deoxyuridine
ELISA	Enzyme-Linked Immunosorbent Assay
ET-1	Endothelin-1
FBS	Fetal Bovine Serum

FDA	Food and Drug Administration
FGF	Fibroblast Growth Factor
FMO	Fluorescence Minus One
GAG	Glycosaminoglycan
GFP	Green Fluorescent Protein
GS	Griffonia Simplicifolia
H&E	Hematoxylin & Eosin
HA	Hydroxyapatite
HO	Heterotopic Ossification
Hz	Hertz (1/seconds)
IACUC	Institutional Animal Care and Use Committee
ICBG	Iliac Crest Bone Graft
IGF	Insulin-like Growth Factor
IL	Interleukin
LV	Latent Variable
MMP	Matrix Metalloprotein
MSC	Mesenchymal Stem Cell
MVF	Microvascular Fragment
NBF	Neutral Buffered Formalin
NO	Nitric Oxide
OP-1	Osteogenic Protein-1
PBS	Phosphate Buffered Saline
PCR	Polymerase Chain Reaction
PDGF-B	Platelet-Derived Growth Factor subunit B
PEEK	Polyetheretherketone

PEG	Polyethylene Glycol
PFA	Paraformaldehyde
PLGA	Poly Lactic-co-Glycolic Acid
PLSDA	Partial Least Squares Discriminant Analysis
pMOI	Polar Moment of Inertia
rhVEGF	Recombinant Human Vascular Endothelial Growth Factor
RIA	Reamer-Irrigator-Aspirator
RM-ANOVA	Repeated Measures Analysis of Variance
RNA	Ribonucleic Acid
ROI	Region of Interest
SDS-PAGE	Sodium Dodecyl Sulfate Polyacrylamide Gel Electrophoresis
SEM	Standard Error of the Mean
SHG	Second Harmonic Generation
SLRP	Small Leucine-Rich Proteoglycan
SMC	Smooth Muscle Cell
SVF	Stromal Vascular Fraction
TCPS	Tissue Culture Polystyrene
TGF β1	Transforming Growth Factor β1
VEGF	Vascular Endothelial Growth Factor
VP	Verteporfin
VML	Volumetric Muscle Loss
VOI	Volume of Interest
YAP	Yes-Associated Protein
TAZ	Transcriptional coactivator with PDZ-binding Motif
μCT	Micro-Computed Tomography

SUMMARY

Bone is a highly vascularized tissue, and adequate vascularity is an essential requirement for proper bone healing. Revascularization is a challenge in critical-sized defects, especially those with concomitant muscle damage typical of traumatic injury. Patients with these injuries heal slowly and exhibit higher rates of infection and non-union, underscoring the critical importance of vasculature to bone healing. Additionally, the bone defect environment is a complex niche, involving mechanical cues in addition to a host of biochemical signals. It is well known that mechanical loading affects bone growth and remodeling, and while flow-mediated mechanics influence the vasculature, remarkably little is known about the effects of bulk matrix deformation on neovascularization. The overall objective of this thesis was to leverage mechanical cues to enhance vascular network formation and to use enhanced vascularization to improve bone regeneration.

First, we evaluated the effect of multicellular microvascular fragments (MVF) co-delivered with BMP-2 to a model of composite bone-muscle trauma using collagen sponge, the clinically available BMP-2 delivery vehicle. MVF did not improve bone healing as hypothesized; however, we also investigated the effect of a modestly increased BMP-2 dose, which did significantly improve functional healing. While MVF maintained viability within the collagen sponge in vitro, they first dissociated to single cells, which we speculated may have prevented their inosculation with the host vasculature. Next, we developed and characterized decorin-supplemented collagen gels for use as both an in vivo co-delivery vehicle for MVF and BMP-2 and as a dimensionally stable biomaterial scaffold to investigate the effects of compressive loading on MVF growth in vitro. Despite in vitro

results demonstrating synergistic effects of BMP-2 and MVF, there was no effect of MVF on bone healing, and MVF significantly decreased early revascularization following injury. However, the addition of decorin increased the compressive properties and dimensional stability of collagen while still supporting robust in vitro MVF growth.

We then evaluated the effects of dynamic compressive loading on MVF growth. While the vasculature has long been recognized as mechanosensitive, the effects of abluminal forces experienced by healing tissues on angiogenesis are poorly understood. We demonstrated that delayed compressive loading led to longer, more extensively branched microvascular networks than early loading at all strain magnitudes tested. Across strain magnitudes, delayed loading increased vascular network length and branching compared to non-loaded controls; however, early high strain loading inhibited network formation. Gene expression analysis revealed differential mechanoregulation of gene expression profiles by early vs. delayed loading. Genes associated with angiogenic sprout tip cells were downregulated by early loading and upregulated by delayed loading. Delayed loading also led to the upregulation of genes involved in cell adhesion and migration. Using a pharmacological inhibitor, we established that the YAP mechanotrasduction pathway is involved in the pro-angiogenic response to delayed loading.

Overall, this thesis has tested MVF as a therapeutic for bone healing, developed and characterized a novel biomaterial for in vitro and in vivo applications, and increased fundamental knowledge about the effects of bulk loading on neovascularization. These findings can be leveraged to more effectively treat composite bone-muscle defects, both through future tissue engineering work and with physical rehabilitation regimens informed by knowledge of loading effects on nascent vasculature.

CHAPTER 1. INTRODUCTION

1.1 Motivation

Bone is a highly vascularized tissue, and adequate vascularity is an essential requirement for proper bone healing. Revascularization is a challenge in critical-sized defects, especially those with concomitant muscle damage typical of traumatic injury. The Gustilo Classification system scores open fractures from I to IIIC in order of increasing severity, increasing complication rate, and increasing patient morbidity. The hallmark of the most severe class IIIC injuries is the presence of vascular damage. Patients with these injuries heal slowly and exhibit higher rates of infection and non-union, underscoring the critical importance of vasculature to bone healing. Additionally, the bone defect environment is a complex niche, involving mechanical cues in addition to a host of biochemical signals. It is well known that mechanical loading affects bone growth and remodeling, and while flow-mediated mechanics influence the vasculature, remarkably little is known about the effects of bulk matrix deformation on neovascularization. To most effectively leverage the use of a vascular therapeutic in this space, we must better understand the effect of the relevant mechanical loading environment on the vasculature. Microvascular fragments (MVF), multicellular structures derived from mature vasculature, form networks in vitro and anastamose with the host vasculature when implanted in vivo. As such, they are a useful in vitro model of mature vasculature and are an attractive therapeutic candidate. Stromal vascular fraction (SVF) is a single cell digestion of mature vasculature that also forms networks in vitro and has been used as an in vivo therapeutic.

The overall objective of this thesis is to leverage mechanical cues to enhance vascular network formation and to use enhanced vascularization to improve bone regeneration. The overarching hypothesis is that cell source, biomaterial scaffold, and mechanical environment each influence the formation of engineered vascular networks.

1.2 Specific Aims

Specific Aim 1: Evaluate effect of vascular cell source co-delivered with BMP-2 to composite defect model. The primary objective of this aim was to overcome the bone healing deficit observed in composite tissue injuries. Microvascular fragments (MVF) and stromal vascular fraction (SVF) were cultured in the presence of BMP-2 in a collagen sponge in vitro. Cell viability and BMP-2 release kinetics were assessed. MVF-seeded sponges released significantly more BMP-2 than acellular or SVF-seeded sponges. Based on these in vitro results and those of a pilot in vivo study, MVF were co-delivered with two doses of BMP-2 in collagen sponge to a critical sized bone defect within a composite bone-muscle defect model. Bone regeneration was evaluated with x-ray radiography and μCT along with endpoint mechanical testing. Inflammatory serum cytokine levels were also quantified. We hypothesized that BMP-2-mediated functional regeneration of composite extremity injuries is dose dependent and can be further enhanced via co-delivery of adipose-derived MVF.

Specific Aim 2: Develop a biomaterial for in vitro studies and in vivo delivery of microvascular fragments. The primary objective of this aim was to develop a dimensionally stable biomaterial to evaluate effects of in vitro loading on MVF over time and to co-deliver MVF and BMP-2 in vivo. Candidate materials were assessed in vitro based on four criteria: 1) robust MVF growth, 2) dimensional stability over time in culture, 3) suitable compressive properties, and 4) sustained BMP-2 release. The material meeting all criteria, decorin (DCN)-supplemented collagen hydrogels, was used to co-deliver MVF and BMP-2 to a composite defect model. We hypothesized that using a biomaterial designed to meet these criteria to deliver MVF and BMP-2 would increase early vascularization and facilitate improved bone healing.

Specific Aim 3: Investigate effects of mechanical loading on microvascular growth and remodeling. The primary objectives of this aim were to elucidate the effects of different abluminal mechanical loading regimes on in vitro MVF growth and network remodeling and to determine the molecular changes associated with observed morphological changes. MVF seeded in collagen+DCN gels were dynamically loaded in either unconfined compression or compression with a shear interface zone to mimic the loading experienced in an in vivo bone defect environment. Vascular growth under loading was assessed by quantifying network length and branch number. We hypothesized that vascular growth would be enhanced by delayed, moderate compression and inhibited by early, high magnitude compression and in regions of high shear. We subsequently investigated the changes in viability, proliferation, perivascular coverage, and gene expression profiles associated with early vs. delayed loading. Based on our morphological results, we

hypothesized that early loading would decrease cell viability, pericyte-vessel attachment, and expression of genes associated with early stage angiogenesis, such as sprout tip cell selection, thereby leading to impaired vascular networks. Conversely, we hypothesized that delayed loading would increase cellular proliferation and increase expression of genes associated with later stages of angiogenesis, such as matrix invasion, collective cell migration, and cell recruitment, thereby leading to more extensive and mature vascular networks. Finally, we investigated the role of YAP mechanotransduction in the differential angiogenic responses to early and delayed loading.

1.3 Significance

A clinically available delivery vehicle was utilized in Aim 1, while Aim 2 developed a material designed to criteria specific to this application to improve its efficacy. Aim 3 then used the material developed in Aim 2 to study MVF networks under the types of loading they experience in vivo and interrogated the molecular changes accompanying morphological changes. Overall, this thesis has tested MVF as a therapeutic for bone healing, developed and characterized a novel biomaterial for in vitro and in vivo applications, and increased fundamental knowledge about the effects of abluminal loading on neovascularization. These findings can be leveraged to more effectively treat composite bone-muscle defects, both through future tissue engineering work and potentially with physical rehabilitation regimens informed by knowledge of loading effects on nascent vasculature.

CHAPTER 2. BACKGROUND AND LITERATURE REVIEW

2.1 Bone

2.1.1 Function and Structure

While often regarded as primarily structural, bone is a dynamic living tissue that performs multiple vital physiological functions. In addition to providing structural support, protection for other organ systems, and leverage for movement, bone also regulates systemic calcium homeostasis and is the primary site of hematopoiesis [1]. Calcium is a crucial element for regulating cell survival and signalling [2], and its systemic concentration is maintained in a delicate balance through coordinated bone resorption and deposition [1]. As the site of immune cell production, bone marrow is intimately linked to systemic immune system function [3]. Bone marrow is also rich in other stem and progenitor cells, including multipotent mesenchymal stem cells [4].

Bone is composed of both inorganic and organic phases. Inorganic mineral, primarily hydroxyapatite (HA; $Ca_{10}(PO_4)_6(OH)_2$), comprises approximately 67% of bone by weight, and organic matrix material, primarily type I collagen, comprises the remaining 33%. The organic phase of bone also includes the primary cells of bone tissue: osteoblasts, osteoclasts, and osteocytes. Osteoblasts, derived from mesenchymal lineage, are responsible for bone formation. Osteoblasts secrete extracellular matrix proteins, including type I collagen, to form osteoid – the template for mineralized bone tissue. In addition to type I collagen, osteoblasts also secrete proteins with high affinity for calcium, such as bone sialoprotein and osteonectin [1]. Following matrix protein secretion, osteoblasts

increase expression of alkaline phosphatase, which cleaves surrounding phosphate groups. Together with calcium, these phosphate groups form crystals that mineralize the osteoid matrix [5]. Osteoblasts also participate in bone resorption through signalling activity that regulates the activity of osteoclasts, the cell type responsible for bone resorption [1]. Osteoclasts are derived from monocytic lineage and thus represent an additional link between bone and the immune system [3]. Rather than matrix proteins, osteoclasts instead secrete acids and proteases that lead to the breakdown of the organic matrix and dissolution of HA, releasing calcium into circulation [1]. After matrix deposition activity, osteoblasts can undergo apoptosis (approximately 60%), become quiescent bone lining cells (~10-30%), or mature into osteocytes that are embedded within the bone matrix (~10-30%) [6]. Osteocytes represent nearly 95% of bone cells and reside within cavities called lacunae, which are embedded within concentric layers of mineralized tissue. Osteocytes have a dendritic phenotype, with extended processes called canaliculi. The canaliculi of distinct osteocytes form gap junctions with one another to allow for cell-cell communication, which is thought to play a key role in bone mechanosensation [1].

Bone can be classified as either cortical bone or trabecular bone. Cortical bone forms the dense exterior of long bones, while trabecular bone makes up the spongy interior. In cortical bone, the concentric mineral layers containing embedded lacunae are called lamellae, which are organized into packed, circular structures called osteons. At the center of each osteon is a Haversian canal, which contains the blood vessels that supply osteocytes through the lacunar-canalicular network. This complex network is required for survival of such a densely structured tissue. In contrast, trabecular bone is organized into rod-like structures surrounding pores filled with bone marrow and blood vessels. The cortical bone

of long bones is lined on its exterior by the periosteum and on its interior (along the medullary canal, which houses bone marrow) by the endosteum, both of which are involved in bone remodelling. As such, the endosteum is particularly rich in osteoblasts, osteoclasts, and bone lining cells. The periosteum has a fibrous outer layer and a highly vascularized inner layer rich in progenitor cells [1]. Structures called Volkmann's canals connect the vasculature of the periosteum to the Haversian canal system and interconnect Haversian canals to one another [7].

2.1.2 Normal Bone Healing Cascade

Bone tissue has a native capacity for repair, and the majority of fractures heal with only immobilization as primary treatment [8]. Fracture healing follows the typical stages of wound healing cascade: hemostasis, inflammation, proliferation, and remodeling [9, 10]. During the proliferation stage, fractures can heal through either of the two modes of bone development: endochondral ossification or intramembranous ossification. In endochondral ossification, typical of long bone development, a cartilaginous template becomes mineralized, whereas in intramembranous ossification, typical of flat bone development, mesenchymal stem cells differentiate into osteoblasts that directly mineralize [11]. In some cases, the two modes can occur simultaneously [12, 13].

Hemostasis, the first stage of fracture healing, is simply the stoppage of active bleeding through coagulation [9]; this forms a hematoma surrounding the fracture. Inflammatory cells, including neutrophils, monocytes, macrophages, T cells, and B cells, then invade the hematoma. Phagocytic cells remove necrotic tissue and, along with other

immune cells, secrete cytokines and chemokines that recruit and mature stem and progenitor cells [10]. A critical event demarcating the transition from the inflammatory stage, which persists on the order of days, to the proliferative stage of wound healing is the invasion of new blood vessels in response to the hypoxic injury niche [14]. Without adequate angiogenesis, bone healing cannot proceed [15, 16]. Osteoprogenitor cells, which can occupy a perivascular niche [17], invade into the injury site along with vasculature [18]. Additional progenitor cells are recruited from the periosteum. Once within the hematoma, osteoprogenitors proliferate, differentiate, and lay down a provisional extracellular matrix that constitutes the initial, nonmineralized fracture callus [10]. In endochondral ossification, chondrocytes deposit a cartilaginous matrix, become hypertrophic, and begin mineralizing. In intramembranous ossification, mesenchymal condensates differentiate into osteoblasts, which begin to mineralize the callus [11]. In both modes of ossification, the soft callus eventually (on the order of weeks) becomes a hard, mineralized structure made of woven bone that is relatively disorganized and mechanically weak compared to mature bone [12]. In the final stage of wound healing, woven bone is remodeled to achieve a mature structure through a balance of osteoclast-mediated bone resorption and osteoblastic deposition of lamellar bone [10]. The remodeling process, which is important for the restoration of intact bone mechanical properties, can take weeks or even years to complete [12].

2.2 Vasculature

2.2.1 Function and Structure

Bone receives up to 15% of cardiac output [11, 19, 20] and is well-vascularized at both the macroscopic scale, with the periosteum serving as a rich vascular source, and at the microscopic scale, with the intricate Haversian canal system supporting the interior of mineralized bone tissue. Vasculature itself also exhibits multiple size scales. Arteries are the largest vessels in a hierarchical structure and transport blood out of the heart. Arteries branch into smaller arterioles, which branch into smaller still capillaries. Capillaries are the vessels through which tissues exchange oxygen and nutrients [21], and diffusion limitations require tissues be within a few hundred microns of a capillary to survive [22]. Capillaries transport deoxygenated blood into venules, veins, and ultimately back to the heart [21]. Arterioles, capillaries, and venules constitute the microvasculature [23].

Both arterial and venous structures consist of three structurally distinct layers: tunica intima, media, and adventitia. Capillaries consist only of the tunica intima. The tunica intima is directly adjacent to the vessel lumen and is composed of monolayer of endothelial cells (ECs) apposed to pericyte support cells [21]. ECs are the cell type closest to blood and form a permeable barrier that selectively allows for transport of metabolites, hormones, proteins, and cells across the vascular system [21, 24]. The endothelial glycocalyx, a layer of proteoglycans and glycoproteins bound to EC membranes, plays an important role in determining the degree of EC permeability and is thought to be involved in vessel mechanotransduction [25]. Pericytes support the thin EC monolayer and are a hallmark of mature vasculature [26]. Without pericytes, vessels are leaky and can become hemorrhagic [27]. Additionally, pericytes are multipotent and capable of differentiating into mesenchymal lineage cells [21, 27, 28]. The tunica media is composed of multiple

layers of perivascular smooth muscle cells within a collagen and elastin matrix, and the tunica adventitia is primarily fibro-elastic connective tissue. These two outer layers allow vessels to contract and dilate in response to physiological demands and tend to be thicker in arterial than venous structures [21].

2.2.2 Angiogenesis

Angiogenesis is the process of new blood vessels forming by sprouting from existing vessel structures. This is in contrast to vasculogenesis, in which progenitor cells assemble into de novo tubular structures. Angiogenesis follows vasculogenesis in embryonic development and continues throughout life to accommodate tissue growth, metabolic demands, and tissue regrowth/healing [29]. In response to hypoxia, cells within an inadequately perfused tissue secrete vascular endothelial growth factor (VEGF), which acts in concert with additional factors as a stimulus to trigger sprouting angiogenesis [22]. Sprouting angiogenesis can be considered in three main steps: tip cell selection, sprout formation, and sprout elongation.

In response to a VEGF gradient, ECs become activated and express a balance of both notch, a receptor, and delta-like ligand 4 (Dll4), its ligand. To prevent complete destabilization of the parent vessel, ECs become either migratory leader tip cells or follower stalk cells through notch-mediated lateral inhibition. Those ECs that express slightly more Dll4 than notch will be selected as tip cells, while those that express slightly more notch become stalk cells. Stalk cells will then also express Jagged-1 (Jag1), which acts as a competitive antagonist and binds notch without activating it, to reinforce the

lateral inhibition signalling [30]. Once selected, the tip cell extends filopodia [22] and begins to migrate along the VEGF gradient into the surrounding matrix. Tip cells upregulate VEGF receptor 2 (VEGFR2) to increase sensitivity to VEGF, and surrounding stalk cells produce soluble VEGF receptor 1 (VEGFR1), which may both reinforce tip-stalk cell dynamics and provide directional guidance to the outgrowing sprout [30]. As the tip and stalk cells collectively migrate, stalk cell proliferation allows sustained sprout elongation [30]. To migrate, cells must interact with the surround matrix through adhesion molecules such as integrins [31]. Proteases, especially matrix metalloproteases (MMPs), also play an important role in sprout elongation, as the surrounding matrix must be disrupted for an elongating sprout to invade. MMP-2, MMP-9, [31, 32] and MMP-14 [30, 33] are known to be especially critical for angiogenesis.

A key step of the maturation of newly formed sprouts is pericyte recruitment, which is mediated through paracrine secretion of factors including platelet-derived growth factor B (PDGF-B) and transforming growth factor β1 (TGF-ß1) [30, 31]. Angiopoietin-1 (Ang1)-Tie2 signalling also promotes the attachment of pericytes to endothelial cells, stabilizing mature vessels [34]. Following lumenization and pericyte recruitment, ECs transition into a quiescent phalanx phenotype [30]. However, in the presence of destabilizing Angiopoietin-2 (Ang2) and VEGF, ECs will become activated and begin sprout angiogenesis [34].

2.3 Composite Bone-Muscle Injuries

2.3.1 Epidemiology and Classification

Fracture healing is a well-orchestrated process that typically restores full function to the affected bone. However, of the six million fractures that occur each year in the United States alone, about 5-10% do not heal with standard treatment and are termed non-unions [35]. Open fractures, which penetrate the soft tissue surrounding the bone, have a higher incidence of complication, with a 25% rate of delayed or nonunion [36]. These complications often involve infection, rehospitalization, and additional surgeries, all of which contribute to a financial burden of over $4 billion on the American healthcare system [37].

Open fractures are commonly classified according to the Gustilo classification systems, which grades fractures in increasing severity from I-IIIC. Class I open fractures are smaller than 1 cm with a relatively clean wound, and class II injuries range from 1 to 10 cm but have only minimal soft tissue damage. Class III injuries are further classified from A-C. Injuries falling into IIIA are larger than 10 cm with extensive soft tissue damage but retain periosteal coverage, while IIIB injuries are stripped of periosteum. Finally, the hallmark of class IIIC injuries is vascular damage – regardless of the degree of soft tissue damage [38]. The fact that the degree of vascular damage is considered the "single most important determinant of complications after an open fracture" [39] underscores the critical importance of vasculature to bone healing. Attenuated healing of bone defects with concomitant muscle damage has also been observed in pre-clinical animal models [40-42], as has reduced vascularity [43, 44].

2.3.2 Current Clinical Treatment Strategies

The current clinical standard of care for long bone defects is an autologous iliac crest bone graft (ICBG) [45], which is osteoconductive, osteoinductive, and osteogenic [46]. Recently, the reamer-irrigator-aspriator (RIA) technique, an alternative autograft source, has become more widely used. RIA harvests a large volume of graft material from the intramedullary canal or either the femur or the tibia and has shown similar efficacy as ICBG [47]. Although RIA is associated with significantly less donor site pain pain than ICBG [47], tissue availability and donor site morbidity are serious disadvantages inherent to any autograft procedure [48]. Allografting is an option but is also challenged by tissue availability. Additionally, relying on an allogeneic source introduces risks of tissue rejection and disease transmission [46]. Several bone graft substitutes, commonly referred to as bone void fillers, are currently clinically available. One commonly used material is demineralized bone matrix (DBM), which is demineralized, sterilized allograft tissue [49]. DBM retains many of the osteoinductive growth factors natively present within bone but is less osteogenic than vital bone graft. Both allograft tissue and DBM are less consistently successful than autografting, which may be driven at least in part by donor-to-donor variability [46].

In addition to the above bone grafting techniques, the standard of care for open fractures includes debriding the wound and covering the bone defect/graft with a flap of intact local muscle, if available, or with muscle tissue from an uncompromised donor site [38, 39]. Coverage with a vascularized muscle flap improves patient outcomes [50], but the mechanism of action is unknown; increased angiogenesis, growth factor availability, and cell recruitment may all be involved [42]. However, functional outcomes of severe

traumatic injuries remain poor. Two-thirds of patients experience long-term (≥ 7 years) disability [51], and limb function often cannot be restored to above that of a prosthesis [52] – particularly for Gustilo type IIIC open fractures with vascular damage [53]. Current treatment strategies can be used to salvage the limb in most cases, but the painful and protracted limb salvage process may actually significantly impair patient quality of life compared to amputation [54]. Some patients even elect to amputate the limb even after enduring the salvage process due to severe lack of function [55].

2.4 Bone Tissue Engineering (BTE)

The limitations of current treatments present a clear need for tissue engineered therapeutics for bone defects with concomitant muscle injury. Key factors to consider in BTE include biochemical cues such as growth factors, biomaterial scaffold, and cell source – either exogenously delivered within the construct or recruited from endogenous populations.

2.4.1 Biological Factors: Growth Factors and Cells

Biochemical signaling plays a key regulatory role in the endogenous fracture healing process, providing many of the cell recruitment and differentiation stimuli required for healing [12]. The bulk of the existing literature has focused on growth factors involved in the proliferative stage of wound healing, including approaches focusing on augmenting vascularization [56], which will be highlighted in 2.4.3. More recent work has also begun

to focus on modulating the cytokine signaling characteristic of the early inflammatory stage of wound healing [57].

There are at least 20 members of the BMP family of growth factors, seven of which have known osteogenic activity [56]. Two of these growth factors, BMP-2 and BMP-7, also known as osteogenic protein-1 (OP-1), have been commercialized within collagen delivery vehicles as Metronic's Infuse and Stryker's OP-1 Putty, respectively [48, 58]. BMP-2 is one of the earliest expressed proteins during osteogenesis and can regulate the subsequent expression of additional BMPs. BMP-2 plays a central role in MSC recruitment and osteoblastic differentiation as well as chondrogenesis, relevant to endochondral ossification [59]. BMP-7 expression temporally follows BMP-2 during endogenous healing. BMP-7 has demonstrated potent osteogenic effects [60] as well as regulatory roles in both endochondral and intramembranous ossification [59]. BMPs are members of the TGF-ß super family along with TGF-ß1, -ß2, and -ß3, which also act as potent chemoattractants for osteoprogenitor cells. Fibroblast growth factor (FGF) and insulin-like growth factor (IGF) are additional factors involved in progenitor cell recruitment and proliferation [59]. TGF-ß [61], FGF [62, 63], and IGF [62] have all been co-delivered with BMPs in preclinical bone defect models. [64] Depending on the growth factor dose ratios and model used, studies have demonstrated synergistic, null, and even inhibitory effects of the additional growth factor as compared to BMP alone [56]. BMP alone, however, consistently displays potent osteoinductive activity.

When exogenous cells are delivered, mesenchymal stem cells (MSCs) are most common. While MSCs have been shown to improve healing pre-clinically [65-67], other similar studies have shown no benefit [67, 68]. This may be due in part to the relatively

poor definition of MSC potency and thus high degree of variability. For example, MSCs that express the same surface markers but are isolated from different tissues can have differential effects on bone healing; bone marrow-derived MSCs augmented BMP-2-mediated mineralization, whereas adipose-derived MSCs inhibited mineralization [67]. This study and others have seen that BMP-2 delivery alone tends to have a much stronger effect than MSCs alone and that co-delivery of MSCs often provides only marginal enhancement of BMP-2-mediated healing [67, 68].

2.4.2 Biomaterials

The biomaterial delivery vehicle for BMP-2 in the clinically approved Medtronic Infuse product is absorbable collagen sponge. Infuse was first clinically approved for and is still most commonly used in spinal fusion cases [69] but has also demonstrated clinical success in open tibia fractures [70]. However, BMP-2 is retained by collagen sponge only through weak electrostatic interactions, leading to an initial burst release of growth factor and therefore requiring supraphysiological doses to be delivered [71]. This release profile, which does not match the natural expression of BMP-2 [72], can lead to adverse effects including extensive local inflammation, ectopic bone formation, and even bone resorption [73]. These challenges motivate the development of a superior delivery vehicle [73].

Biomaterial delivery systems that better control BMP-2 release both spatially and temporally, such as a nanofiber mesh surrounding a BMP-2-laden alginate hydrogel, have shown improved pre-clinical bone healing as compared to collagen sponge [74, 75]. Other naturally derived materials, including chitosan [76], fibrin [77], hyaluronic acid [78], and

silk fibroin [79] have been used as pre-clinical hydrogel delivery vehicles for BMP-2. While natural polymers are often biodegradable and offer bioactivity in the form of native cell binding motifs, they also tend to be more immunogenic, challenging to process, and difficult to modify. Synthetic polymers with tunable chemical and mechanical properties such as poly-ethylene glycol (PEG) [80] and poly-lactic-co-glycolic acid (PLGA) [81] based materials have also been explored in bone regeneration applications [82, 83]. Ceramic materials including hydroxyapatite (HA) and tri-calcium phosphate have also been widely utilized in pre-clinical studies [83, 84]. While ceramics better match the composition of native bone than hydrogels, they are brittle. Composite materials that combine two or more materials (e.g. alginate+PEG or HA+PLGA) into a single construct have also begun to be investigated to combine the desirable properties of two different materials [85-87]. Regardless of the specific material chosen, growth factor release kinetics and support of cellular invasion and viability are critical.

2.4.3 Vascularization Strategies

Vascularization is critically important to bone regeneration and remodeling and plays an enabling role in the wound healing cascade [11, 88]. Moreover, tissue engineered constructs are diffusion-limited in terms of nutrient and oxygen transport, meaning that any implanted cells beyond the range of ~200 μm will die unless perfused [89]. Previous research has investigated co-delivery of BMP-2 and VEGF), a key regulator of angiogenesis during bone repair [90]. A number of studies suggest that these two growth factors have a synergistic effect on healing [91-93], while others note no improvement as

compared to BMP alone [94]. Several studies note an initial improvement in bone volume at early time points (4 weeks) but no ultimate effect at terminal time points (8-12 weeks) [56, 95, 96]. In vitro studies have demonstrated positive, bi-directional signaling crosstalk between the two growth factors [97, 98], but the balance of BMP and VEGF ratios and differential release profiles may require optimization before this strategy can be reliably effective in vivo [94, 99]. Additional studies have delivered VEGF without BMP and seen no improvement in bone healing [96, 100], suggesting that some osteoinductive signaling is required in addition to targeting vascularization alone.

Another approach to promote both angiogenesis and osteogenesis is the delivery of cells rather than growth factors. Co-implantation of endothelial cells and MSCs within a bone defect has shown increased vascularity and bone volume [101], particularly when the cells have been pre-cultured prior to implantation to allow for effective pre-vascularization of the constructs [102, 103]. Mechanical properties of regenerate bone have also been improved by increased vascularization facilitated by implanted endothelial cells [104]. However, vascularization formed from implanted endothelial cells tends to be leaky and immature [105]. Cell-based therapies in general tend to display low survival and retention rates [68, 106], perhaps due in part to hypoxia created by delayed anastomosis with the host vasculature.

2.5 Adipose-Derived Vascular Cell Sources

2.5.1 Microvascular Fragments

Microvascular fragments (MVF) are multicellular segments of intact vasculature that can sprout and form networks in vitro. They are isolated from mature vasculature and are composed of a variety of cell populations including endothelial cells, smooth muscle cells, pericytes, mesenchymal stem cells, and endothelial progenitor cells [107, 108]. While MVF are typically isolated from adipose tissue, their angiogenic potential is independent of tissue source [109]; the adipose site has translational advantages, with potential for autologous use. MVF are typically cultured in a low-density type I collagen gel [110-113] and are sensitive to matrix properties such as density and stiffness [110, 113]. In combination with an appropriate 3D matrix, MVF allow for cell-cell interactions among multiple cell types and cell-matrix interactions, thereby better representing the complex in vivo processes of angiogenesis than models utilizing single cells or 2D substrates. As such, they are a useful in vitro model system for angiogenesis.

Additionally, MVF have been implanted in vivo, where they have been shown to inosculate with the host vasculature [114, 115], increase vascularity of tissue defects [116, 117], and improve tissue grafting in pre-clinical models [118, 119]. Many therapeutic applications have used freshly isolated MVF, although inosculation has been shown to occur more rapidly when MVF are precultured prior to implantation [115]. Due to their lumenized structure and retention of support cells [107], MVF are an attractive therapeutic option to restore mature vascular networks.

2.5.2 Stromal Vascular Fraction

Stromal vascular fraction (SVF) is a single cell level digestion consisting of a heterogeneous mixture of endothelial cells, mesenchymal stem cells, smooth muscle cells, fibroblasts, and macrophages and is also most commonly obtained from adipose tissue [120]. SVF also forms interconnected, lumenized networks in vitro [121], but because they must first assemble into tubular structures, the timescale is longer for SVF than for MVF. In vivo, SVF forms vascular networks along with endogenous cells that inosculate with host vasculature and become perfused. This is true using both freshly isolated and pre-cultured SVF [122]. SVF has been isolated clinically from liposuction aspirates and used as a therapeutic [123], representing a significant translational advantage over MVF.

2.6 Mechanics

2.6.1 Effect of Mechanical Stimulation on Bone

Normal bone physiology is strongly influenced by mechanical loading. Physiological levels of loading typical of normal use prevent bone resorption, while greater loading promotes an increase in bone mass [124, 125]. This is a cell-mediated process, in which osteocytes are thought to act as the primary mechanotransducers [126]. Mechanics also influence bone healing, and these effects are driven primarily by osteoblast differentiation, proliferation, and matrix production [127-129]. The interfragmentary strain hypothesis postulates that cells present within the defect repair tissue sequentially differentiate to form tissues with higher ultimate strain than the interfragmentary strain presently experienced. Thus, as tissue grows and differentiates within the defect space, the interfragmentary strain decreases and the defect stiffness increases [130]. This long-

standing hypothesis has been supported by studies directly comparing in vivo osteotomy healing with the healing predicted by strain-directed computational models [131] and by in vitro studies demonstrating that matrix stiffness directs MSC differentiation lineage [132]. Mechanical stimulation mediated by fluid flow [102] and by tension and compression applied to the culture surface [133] also promote enhanced osteogenic differentiation of MSCs in vitro. Mechanical stimulation broadly encompasses multiple parameters, including strain magnitude, mode of loading (e.g. compression vs. tension), frequency, and timing, all of which are known to influence bone's response to loading.

2.6.1.1 Compressive Strain Magnitude

Native bone tissue is responsive to strain magnitude, and bone mass increases in a dose dependent manner. There is a lower threshold required to achieve a response [134] and an upper threshold above which bone formation is halted and damage may be sustained [135]. Mechanical cues can serve as either an anabolic or catabolic stimuli to regenerating bone tissue [136]. Moderate strain micromovements have consistently been shown to improve fracture healing [127, 137, 138]. However, when these micromovements are too large, fracture healing can be delayed [139] or altogether halted [140], and mechanical instability is noted as a principal cause of fracture non-union [141]. Reliance on various different in vivo models to vary the mechanical environment (e.g. size of osteotomy gap [140], rigidity of fixator [136, 139], and application of force through external fixator [137]) has made it difficult to reconcile all the existing literature to arrive at a defined threshold for anabolic vs. catabolic, and therefore therapeutically desirable, strain magnitude. In a

pseudarthrosis model, loading was applied to a hinged fixator to apply spatial gradients of strain magnitudes across the defect tissue. These force gradients were quantified and spatially correlated with resulting tissue type by histology. Below 10% strain, the highest probability tissue type was bone, with the peak probability of bone formation occurring around 2-5% strain. Above 10%, the highest probability tissue type was non-healed fibrous tissue [142]. In an osteotomy model, Claes et al. identified 5% strain as a threshold for intramembranous ossification and 15% strain for endochondral ossification [143].

2.6.1.2 Mode of Loading Compression, Tension, and Shear

Fracture healing is sensitive to the mode of loading, e.g. compression, tension, bending, or shear. Compression has been the most commonly studied and is widely accepted to improve healing up to a critical strain threshold [144]. Bone tissue is also sensitive to tensile loads [135], and tension affects fracture healing similarly to compression; moderate applied tension is stimulatory, while large magnitude tension leads to reduced healing and even resorption [131]. Tension is a component of the common clinical practice of distraction osteogenesis [145]. The effects of interfragmentary shear and bending are less well understood. Bending incorporates elements of both compression and tension, and in one study of bending, the fracture callus mineralized and bridged only on the compressive side and not on the tensile side of bending [146]. In a recent review article, Betts and Muller highlighted eight studies of interfragmentary shear. Of these, six reported negative effects of applied shear and two reported positive effects [144]. Difference in animal model, strain magnitude, and strain frequency along with the ability

to isolate shear from any other mode of loading may explain the contradictory results. Interestingly, in the pseudarthrosis study discussed in 2.6.1.1 that correlated local strain with tissue type, 10% strain was consistently the threshold transition point from a greater probability of forming bone to a greater probability of a fibrous response across compression, tension, and shear [142].

2.6.1.3 Time: Frequency, Duration, and Initiation

Native bone exhibits sensitivity to dynamically applied loads but not static loads [147], which is analogous to sensitivity to walking but not to standing. Gait frequency for humans is approximately 1 Hertz (Hz) [148] and up to 4 Hz for rodents, making these commonly studied frequencies [149]. Bone formation exhibit a dose response to load frequency, with bone mass increasing as frequency increased from 1-10 Hz [150]. Interestingly, very low magnitude strains typically below the threshold of effect can be potentiated by applying them at high frequencies (30 Hz), both increasing native bone mass [151] and accelerating fracture repair [152]. The ability of dynamic loading to increase bone formation is potent and can be detected after only a single loading period [153]. However, the mechanosensitivity of bone becomes saturated [149], and the anabolic effects plateau after relatively few continuous cycles [154]. Partitioning the loading into multiple, shorter cycles [155] or inserting rest periods as short as 14 seconds can restore mechanosensitivity [156].

Finally, the initiation time of loading has also been implicated as an important factor in achieving an anabolic rather than catabolic effect of mechanical stimulation.

Gardner et al. compared the effects of loading on the day of osteotomy vs. loading four days following the osteotomy surgery. Early loading led to reduced failure strength relative to the non-loaded control, whereas delayed loading increased failure strength relative to the control [157]. Subsequent work by Boerckel et al. observed a similar time-dependent effect in a critical size bone defect. Bone volume and mechanical strength were decreased due to early loading but increased by delayed loading. Additionally, this study measured vascular volume and found that the vascular response mirrors that of bone [136], suggesting that the early vascular response to the mechanical environment may drive subsequent bone formation.

2.6.2 Effect of Mechanical Stimulation on Vasculature [1]

Vascular growth and remodeling are highly sensitive to mechanical cues; however, much of the existing research in this field has focused on luminal mechanics related to fluid flow (i.e. fluid shear and cyclic stretch) rather than abluminal stimulation of the entire vessel network [158, 159]. Additionally, much of the existing literature has used two-dimensional cell monolayers that likely do not fully recapitulate the cell-cell interaction effects present in vivo.

[1] Portions of this section have been adapted from Section 2.1 of Krishnan, L., LaBelle, S.A., **Ruehle, M.A.**, Hoying, J.B., Weiss, J.A., and Guldberg, R.E. Mechanical Regulation of Microvascular Growth and Remodeling, in Vascularization for Tissue Engineering and Regenerative Medicine, Holnthoner, W., Banfi, A., Kirkpatrick, J., Redl, H., Editors. 2019, Springer International Publishing: Cham. 2019. Reproduced with permission: license number 4584870078122.

2.6.2.1 Fluid Shear

Initial *in vitro* models utilizing aortic endothelial cell monolayers exposed to constant laminar flow demonstrated that fluid shear leads to changes in cellular morphology, alignment, and migration. Under uniform laminar flow, cells transition from a polygonal to elliptical shape, with the primary axis aligning with the direction of flow [160-162]. Laminar flow also affects endothelial cell pinocytosis and fluid endocytosis, indicating that metabolism within and bulk transport across the vascular endothelium are also sensitive to shear [160]. These cellular responses all occur in a time and shear magnitude-dependent manner, with intracellular pinocytosis changes occurring before morphological or alignment changes [163].

Biochemical changes also occur in response to laminar flow, including altered production of vasomediators such as prostacyclin, endothelin-1 (ET-1), and nitric oxide (NO). Vasodilator (prostacyclin and NO) production levels are increased by pulsatile flow as compared to uniform flow, under which a steady-state is quickly achieved [164, 165]. Vasoconstrictor (ET-1) production is decreased under shear stress conditions [164]. Intracellular calcium ion concentrations also vary between pulsatile and uniform flow. Uniform flow increases Ca^{2+} concentration relative to static controls, and pulsatile flow further increases Ca^{2+} concentration. Purely oscillatory flow ("on-off" rather than periodic magnitude changes) does not change Ca^{2+} concentration. By affecting intracellular Ca^{2+} concentration, flow profiles mediate Ca^{2+} dependent signaling cascades to effect downstream cellular responses such as the vasomediator production previously discussed [166, 167]. These functional changes provided support for early in vivo observations implicating fluid flow properties in pathologies such as atherosclerosis.

2.6.2.2 Tensile Stretch

Stretch elicits many of the same cellular responses as shear stress. Cyclic mechanical stretch, as cells experience *in vivo*, also increases cellular proliferation and changes protein production profiles [168, 169]. Like shear stress, stretch increases mediators of signaling cascades, such as intracellular Ca^{2+} concentration and cyclic adenosine monophosphate (cAMP) [170, 171]. Production of vasomediators including NO synthase (NOS), ET-1, and prostacyclin is also increased by stretch [172-174]. The morphological effects of shear and mechanical stretch stimuli, such as cellular elongation and alignment, can be additive [161, 175].

The cyclic loading of endothelial and perivascular cells has been approximated in vitro by growing cells on deformable substrates. Cyclic stretch can induce strain-dependent increases in secretion of proteolytic enzymes and accelerate the generation of cord-like networks on planar EC monolayers [176]. When ECs and SMCs were co-cultured on an elastomeric substrate, cyclic tensile stretch increased EC sprouting and migration and SMC recruitment. Stretching increased EC secretion of angiopoietin-2, which increased EC sprouting through autocrine signaling, and secretion of platelet derived growth factor (PDGF), which increased SMC recruitment through paracrine signaling [177]. These results suggest that mechanical cues could be driving many of the biochemical cues well-known to influence vascularization.

2.6.2.3 Extracellular Matrix Deformation

Vascular cells are also influenced by the mechanics of their ECM substrate, and matrix stiffness is well recognized as a critical element in vessel growth and function [178]. Softer substrates generally produce a more rounded morphology, elicit greater migration, and allow higher levels of protrusion and retraction activities [179, 180]. In contrast, higher moduli substrates are deformed less by ECs, which also proliferate more on stiffer substrates, show more prominent stress fiber formation, and upregulate RhoA activation [181, 182]. Cells have been shown to preferentially migrate towards stiffer substrates as well as change direction of migration in response to mechanical stimuli, termed durotaxis [183]. Bovine aortic endothelial cells cultured on substrates with different stiffness showed organization into cord like structures on more compliant substrates, but not stiffer substrates, when substrates were coated with the same amount of collagen [184]. ECs cultured on fibronectin coated surfaces form multicellular cord like structures at an optimal fibronectin surface coating density but not on highly adhesive (high fibronectin density) surfaces. Further, culturing endothelial cells within a three-dimensional gel of ECM components greatly facilitates angiogenesis, promoting tube formation within days rather than the weeks required on protein-coated rigid dishes [185]. These observations suggest that both ECM stiffness and cell binding motif density are important factors in capillary network or sprout formation.

MVF cultured in three-dimensional collagen matrices also exhibit sensitivity to extracellular matrix stiffness and density. As collagen density increases, vascular network length, branching, and interconnectivity all decrease. Computational simulations suggest that the rate of growth and branching is slowed by increased matrix density [113]. Matrix

density cannot be completely decoupled from matrix stiffness and availability of adhesive ligands, both of which may independently or cooperatively influence the morphological effects. Additionally, MVF themselves also affect ECM stiffness. Through protease activity, MVF remodel collagen matrices, decreasing stiffness as sprouting initiates. Following the primary invasion of the matrix, however, MVF then increase the matrix stiffness above initial levels through ECM deposition and contraction of the collagen substrate [112]. Interactions between vasculature and ECM are bidirectional, and this interplay supports the study of angiogenesis in three-dimensional culture systems rather than in monolayer alone.

Abluminal forces that deform the extracellular matrix surrounding a vascular network are particularly relevant to load-bearing tissues such as bone. In vitro studies have shown that tensile forces affect the alignment and sprouting of microvascular networks, with MVF aligning parallel to the direction of applied tension [111, 112]. Neither static nor dynamic active stretching produced more alignment of vessels than the passive stretch created by holding the gel within the loading fixture. All three conditions (static 6% stretch, dynamic 6% stretch, and passive boundary condition stretch) produced a higher number of vessels than unconstrained controls, and static stretch produced the greatest degree of branching [111, 112]. Although early studies with EC monolayers cultured on deformable substrates induced cell orientation perpendicular to the direction of stretch [186], orientation of vessels parallel to the direction of applied tension has been replicated in other three-dimensional culture systems. In a 3D co-culture of ECs and fibroblasts, vessel alignment was mediated by actin stress fibers and associated with differential protein secretion [187].

While bone tissue does experience some tensile forces, compressive forces dominate, and there is little existing literature on the effect of abluminal compressive forces on vascular network growth or remodeling. Previous in vivo research has demonstrated that functional loading has a potent time-dependent influence on vascular growth during segmental bone defect healing. Loading of the bone defect through ambulatory activity was allowed either early, immediately following the defect creation surgery, or delayed four weeks post-surgery. Early loading impaired vessel growth, whereas delayed loading enhanced vascular growth. Furthermore, ultimate differences in bone healing followed the earlier changes in vascular networks; bone healing was impaired due to early loading and enhanced due to delayed loading [136]. These promising results may have implications for both vascularization strategies for tissue engineering and physical rehabilitation following bone injury; however, the in vivo environment is inherently complex, and well-controlled in vitro studies are needed to better understand the mechanical cues associated with vascular growth and inhibition.

CHAPTER 3. CHARACTERIZATION OF VASCULAR CELL-LADEN COLLAGEN SPONGES AS BONE TISSUE ENGINEERING CONSTRUCTS

3.1 Introduction

Bone tissue has an innate capacity for repair, and the majority of fractures heal with only immobilization as the primary treatment. However, approximately 5-10% of fractures do not heal with standard treatment and are termed non-unions [8]. Non-unions represent a clinical challenge for orthopaedic surgeons, as these injuries by definition require multiple different interventions to be implemented in an attempt to achieve bone union. Non-union increases the overall healing time, increasing the duration of time a patient may be disabled, and each procedure involves risks and pain for the patient [188]. The current clinical standard of care for long bone defects is autografting; however, tissue availability and donor site morbidity are serious disadvantages of the autograft procedure [48]. One clinically available alternative to autografting is the use of bone morphogenetic protein-2 (BMP-2) delivered on collagen sponge. Originally approved for use in spinal fusion [69], BMP-2 on collagen sponge has now been used in tibial fractures for over 15 years [70]. BMP-2 is a growth factor capable of inducing bone formation, while collagen sponge provides a matrix both to retain BMP-2 and to support progenitor cell ingrowth [71].

A functional vascular network is required to support the survival of cells that migrate into the bone defect space and is a key, enabling step of the wound healing cascade [10, 11, 88]. Angiogenesis and osteogenesis are known to be intimately linked [11, 17, 20,

189], and when vascularization is impaired, bone healing is also substantially impaired [16]. The importance of vascularization is also appreciated clinically; vascular damage is a key indicator of open fracture severity [38]. As such, bone tissue engineering strategies that aim to enhance vascularization, such as co-delivery of BMP-2 and vascular endothelial growth factor (VEGF), have been previously implemented; however, these approaches have achieved variable results [92, 94, 95]. While some growth factor co-delivery strategies report an improvement in healing [91-93], others report no lasting effect [94-96, 99]. Cell-based approaches to vascularization have been shown to improve bone healing. However, these studies have tended to focus on the delivery of a single vascular cell type (e.g. endothelial progenitor cells) rather than all those of mature vasculature [101, 104], which often produces a leaky, immature vascular phenotype [105].

Microvascular fragments (MVF) are multicellular segments of intact vasculature that can sprout and form in vitro vascular networks [107, 113]. They are isolated from mature vasculature and are composed of a variety of cell populations including endothelial cells, smooth muscle cells, and pericytes [107]. MVF have been implanted *in vivo*, where they have been shown to inosculate with the host vasculature [114, 115] and increase vascularity of tissue defects [116]. MVF are most commonly obtained from adipose tissue [109], which holds potential for autologous transplantation.

Stromal vascular fraction (SVF) is a single cell level digestion consisting of a heterogeneous mixture of endothelial, mesenchymal, smooth muscle, and hematopoietic cells and is also most commonly obtained from adipose tissue [120]. SVF forms interconnected networks in vitro, but because they must first assemble into tubular structures, the timescale is longer for SVF than for MVF. SVF has been isolated clinically

from liposuction aspirates and used as a therapeutic [123], representing a significant translational advantage over MVF.

We aimed to develop a clinically translatable tissue engineering construct to deliver vascular progenitors, either multicellular microvascular fragments (MVF) or component single cells (SVF), along with BMP-2 on collagen sponge. We first characterized the constructs in vitro and observed differential in vitro BMP-2 recovery from constructs containing MVF vs. SVF. We subsequently hypothesized that MVF may have increased BMP-2 recovery from constructs due to production of BMP-2 or due to increased protease activity. Finally, we implanted these constructs into a rat composite bone-muscle defect model that exhibits both attenuated bone healing [42] and decreased vascularity [43, 44]. We hypothesized that 1) a vascular cell-laden construct would improve bone healing relative to an acellular BMP-2 construct and 2) MVF would further improve bone healing relative to SVF due to their preformed tubular structure.

3.2 Methods

3.2.1 MVF and SVF Isolation

MVF were isolated as previously described [107]. Briefly, epididymal fat pads were harvested from Lewis rats, minced, and digested with a collagenase solution for 7-8 minutes at 37 °C while manually shaking. Fragments were obtained through selective filtration, excluding tissue larger 500 μm and single cells smaller than 50 μm. SVF was

obtained through a similar process; digestion time was increased to 30 minutes on an orbital shaker at 225 rpm and 37 °C, and only single cells smaller than 50 μm were retained.

3.2.2 Cellular Characterization

Selected cellular subpopulations of MVF vs. SVF were quantified using flow cytometry. Freshly isolated MVF were subsequently further digested to single-cell level with 30 minutes of collagenase solution digestion on an orbital shaker at 225 rpm and 37 °C. MVF and SVF were fixed in 1% paraformaldehyde (PFA) for 10 minutes at 4 °C. Cells were permeabilized with 0.5% Tween-20 in PBS for 20 minutes. Cells were then stained for mesenchymal stem cell (MSC) surface markers CD29 (BioLegend, San Diego, CA, 102222), CD90 (BioLegend, 202506), and CD 45 (BioLegend, 202207) [190], and mature endothelial cell (EC) surface marker CD 31 (Bio-Rad, Hercules, CA, MCA1334A647) [121], and for intracellular alpha smooth muscle actin (ASMA; Abcam, Cambridge, MA, ab8211) [120]. Cells double positive for CD31 and ASMA were defined as pericytes [191]. Stained cells were refixed as before and analyzed using a BD FacsAria Fusion.

Flow analysis was performed using FlowJo 10 (Becton, Dickinson and Company; Franklin Lakes, NJ). Compensation was applied using single stained controls. Gating was determined using fluorescence minus one (FMO) controls. FMO controls are stained with all fluorophores minus one, and gating was determined such that only contained 1% of FMO cells were positive for the missing fluorophore [192].

3.2.3 Construct Loading & Viability

MVF and SVF were suspended in αMEM (ThermoFisher Scientific; Waltham, MA) and loaded into collagen sponges (5 mm diameter, 1 cm height; Kensey Nash/DSM; Exton, PA) by pipetting 130 µL dropwise. MVF were seeded at a density of 40,000 MVF/mL, and SVF were seeded at a density of 4 x 10^6 cells/mL. Following a 20 minute cell attachment period, 250 µL of media (αMEM supplemented with 10% fetal bovine serum (FBS; Atlanta Biologicals; Atlanta, GA) and 1% penicillin-streptomycin-L-glutamine (ThermoFisher)) was added to each construct [112]. Constructs were cultured for 14 days to assess cell viability, which was determined with live/dead stains (ThermoFisher) performed at time points up to 14 days (n=3/group/time point).

3.2.4 BMP-2 Release Kinetics

To evaluate release kinetics, 500 ng BMP-2 (R&D Systems, Minneapolis, MN) was added to αMEM (acellular), αMEM containing MVF, or αMEM containing SVF and pipetted dropwise onto collagen sponges (n=3/group). BMP-2 recovery from collagen sponges seeded with αMEM containing MVF without exogenous BMP-2 (n=3). Following a 20 minute binding period, 250 µL of media was added to each construct; media was collected and replaced at time points up to 21 days. BMP release was also measured from 3% type I collagen gels. 250 µL gels were formed in 48-well plates and were either acellular or contained 20,000 MVF/mL. Media was collected and replaced up to 14 days. Media BMP-2 content was quantified with enzyme-linked immunosorbent assay (ELISA; R&D Systems).

3.2.5 Gene Expression

To assess gene expression in the collagen sponge, MVF and SVF were seeded with or without 500 ng BMP-2 (n=5/group). RNA was isolated from constructs using Qiagen MinElute kits at hours 0, 3, 6, and 24 of culture. cDNA was created using Qiagen RT^2 First Strand kits. Expression of BMP-2 (ThermoFisher, Rn00567818_m1), cathepsin K (CtsK; Rn00580723_m1), and matrix metalloproteinase 14 (MMP14; Rn00579172_m1) was measured and expressed at each time point relative to hour 0 and to housekeeping genes ß-actin (Rn00667869_m1) and GAPDH (Rn01775763_g1) using the ΔΔCt method.

3.2.6 BMP-2-Primed 2D Culture

MVF were plated directly onto tissue culture polystyrene (TCPS) at a density of 4500 fragments/cm^2 to promote their dissociation to single cells. SVF was also plated directly onto TCPS at a density of 4.5 x 10^5 cells/cm^2. MVF and SVF were cultured in media with or without 500 ng BMP-2 for 24 hours (n=3/group). After 24 hours, all media was removed, cells were washed three times with fresh media, and culture was continued in fresh media that did not contain exogenous BMP-2. At hours 24 and 96 following the BMP-2 priming period, media was removed for ELISA (R&D Systems) and replaced with fresh, non-BMP-2-containing media. Cells were harvested at the same time points, and BMP-2 gene expression was assessed as in 3.2.5.

3.2.7 Pilot in vivo Study

Composite bone-muscle defects were created in 13-week-old female Lewis rats by creating an internally stabilized 8 mm femoral defect with an overlaying 8 mm diameter full-thickness quadriceps defect, as described in [42]. Bone defects received a cylindrical collagen sponge (5 mm diameter by 10 mm height) containing BMP-2 with MVF (80,000 fragments/mL; n=3) or SVF (4 x 10^6 cells/mL; n=3). Collagen sponges without BMP-2 were used as a negative control (n=3), and acellular sponges containing 2.5 μg BMP-2 were used as a positive control (n=3). Constructs were loaded by pipetting 130 μL dropwise as in in vitro studies. All muscle defects were left untreated.

Longitudinal bone volume was assessed using micro computed tomography (μCT) at 4, 8, and 12 weeks post-surgery. The defect region was scanned with a voxel size of 38.9 μm, and bone volume was quantified by Scanco software using a threshold corresponding to 50% of intact cortical bone [42, 193]. Terminal mechanical testing was also performed at the 12 week end point. Femur ends were potted in Wood's metal and tested in torsion at a rate of 3°/s to failure (ELF 3200, TA ElectroForce) [61]. Failure strength was calculated as the maximum torque at failure, and torsional stiffness was calculated as the linear region of torque vs. rotation. All animal experiments were performed in accordance with the Georgia Institute of Technology IACUC.

3.2.8 Statistical Analysis

Data was analyzed using GraphPad Prism 5 with α=0.05. BMP-2 release data from collagen sponge and collagen gel were analyzed using a repeated measures ANOVA (RM ANOVA). Gene expression data from collagen sponge and 2D TCPS were analyzed with a two-way ANOVA. In vivo bone volume, failure strength, and stiffness were analyzed with a one-way ANOVA. ANOVAs were followed with a Bonferroni post hoc test. BMP-2 recovery from MVF+BMP vs. SVF+BMP in the 2D TCPS environment and flow cytometry data were analyzed with a Student's t-test.

3.3 Results

3.3.1 Cellular Characterization

MVF contain more endothelial cells (EC; CD31+αSMA-; p=0.019) than SVF, while SVF contain more stromal cell types: smooth muscle cells (SMC; CD31-αSMA +; p=0.0054), pericytes (CD31+αSMA+; p=0.0012), and mesenchymal stem cells (MSC; CD29+CD90+CD45-; p=0.0007) (Figure 3.1).

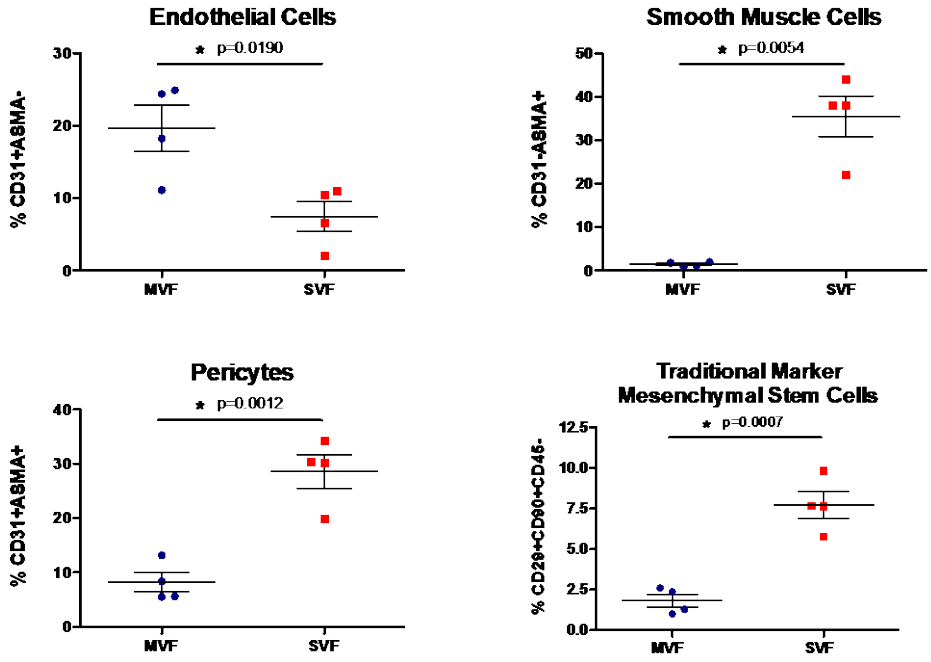

Figure 3.1. Flow cytometry characterization of MVF and SVF cellular subpopulations. MVF have a higher proportion of endothelial cells, while SVF have a higher proportion of stromal cells such as MSC, SMC, and pericytes. Student's t-test, * $p<0.05$.

3.3.2 Construct Viability

Both MVF and SVF remained viable in the collagen sponge constructs co-loaded with BMP-2 for at least 14 days. However, in contrast with the typical sprouting angiogenesis observed when MVF are cultured in collagen gels, MVF appeared to dissociate to a single cell level by day 5 before reforming tubular structures around day 9. Single cell SVF formed tubular structures by day 9 (Figure 3.2).

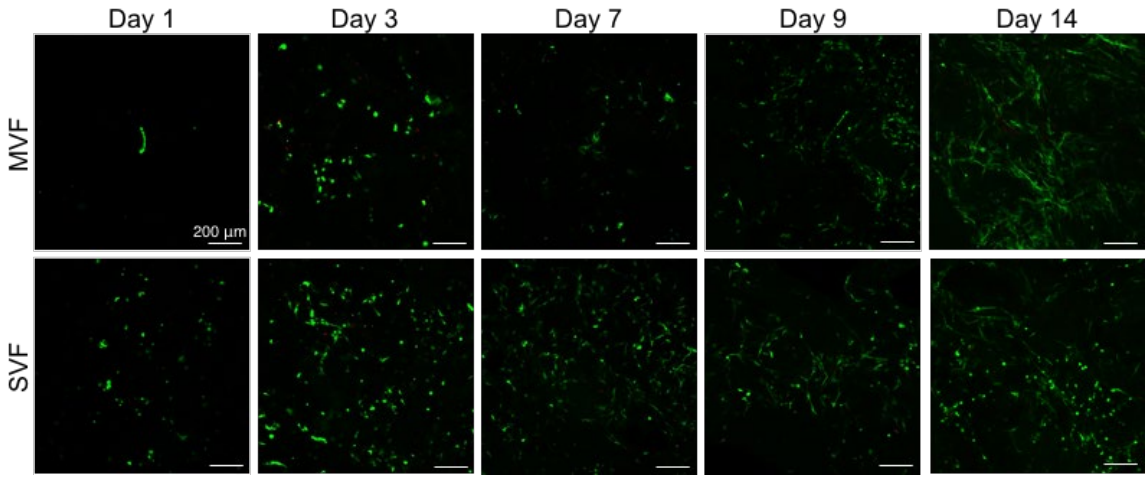

Figure 3.2. Viability of MVF and SVF over time in culture within collagen sponge. Collagen sponge constructs supported viability of MVF and SVF to at least day 14 of culture (live – green; dead – red). However, MVF dissociated from multicellular structures to single cells by day 3.

3.3.3 BMP-2 Release Kinetics

Acellular, SVF-containing, and MVF-containing collagen sponges were loaded with 500 ng BMP-2 and cultured for 21 days. Media was collected at various time points, and the amount of BMP-2 in the media was quantified. By day 21, 25-30% of loaded BMP-2 was recovered from acellular and SVF loaded collagen sponges, which is consistent with previously reported in vitro BMP-2 release from collagen sponge [194]. However, over 75% of loaded BMP-2 was recovered MVF-containing collagen sponges by day 21. Significantly more BMP-2 was recovered from MVF- containing than SVF- containing or acellular sponges from hour 6 through 21 days (n=3; Figure 3.3 A). This result was confirmed in three independent experiments. No detectable BMP-2 was recovered from MVF-containing collagen sponges without exogenous BMP-2, which was significantly different than all other groups at all time points beyond hour 0 ($p<0.001$).

Approximately 40% of loaded BMP-2 was recovered from both MVF-loaded and acellular collagen gels; significant differences did not exist between the two groups at any time point (n=3; Figure 3.3 B).

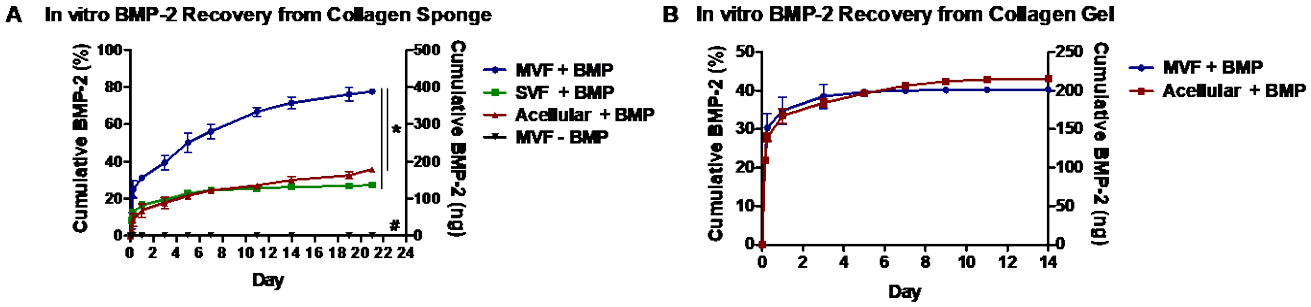

Figure 3.3. In vitro BMP-2 recovery from collagen constructs. Cumulative BMP-2 recovery from A) collagen sponge and B) collagen gel constructs. RM-ANOVA, n=3/group. * indicates MVF-loaded constructs are significantly different than SVF-loaded and acellular constructs from hour 6 through day 21, $p<0.05$. # indicates MVF-loaded constructs without exogenous BMP-2 are significantly different from all other groups at all time points beyond hour 0, $p<0.001$.

3.3.4 Gene Expression

We hypothesized that the increased BMP-2 recovery from MVF-containing sponges could be due to cellular production of BMP-2 or increased protease activity in MVF compared to SVF. Thus, expression of BMP-2, neovessel-specific MMP14 [195], and cathepsin K (CtsK) were measured for MVF cultured with BMP-2 (MVF+BMP), for MVF cultured without BMP-2 (MVF-BMP), for SVF cultured with BMP-2 (SVF+BMP), and for SVF cultured without BMP-2 (SVF-BMP).

BMP-2 expression was significantly higher in MVF than SVF both with (Figure 3.4; $p<0.01$) and without BMP-2 ($p<0.05$) at hour 3. At hour 3, MVF expression of BMP-

2 was approximately 4.5-fold higher than its BMP-2 expression at hour 0 (i.e. immediately following harvest), while hour 3 SVF expression of BMP-2 was only approximately 1.5-fold greater than that at hour 0. At hour 6, BMP-2 expression was significantly higher in MVF-BMP than in SVF-BMP ($p<0.01$). Hour 6 MVF expression of BMP-2 was approximately 1.5-fold higher than at hour 0, while SVF expression of BMP-2 was approximately equivalent to that at hour 0. By hour 24, there were no significant differences in BMP-2 expression between MVF and SVF. There was no significant effect of exogenous BMP-2 on BMP-2 gene expression at any time point, and there were no significant interaction effects.

MVF+BMP expression of MMP14 was significantly higher than SVF+BMP expression at hour 24 ($p<0.05$). CtsK expression was significantly higher in MVF than SVF both with ($p<0.01$) and without BMP-2 ($p<0.05$) at hour 3, and CtsK expression was significantly higher in MVF+BMP than in SVF+BMP ($p<0.05$) at hour 6. MVF expression of MMP14 at hour 24 is the only time point at which expression of either protease by either MVF or SVF was elevated above that at hour 0. There was no significant effect of exogenous BMP-2 in the collagen sponge culture constructs on gene expression of either protease at any time point, and there were no significant interaction effects.

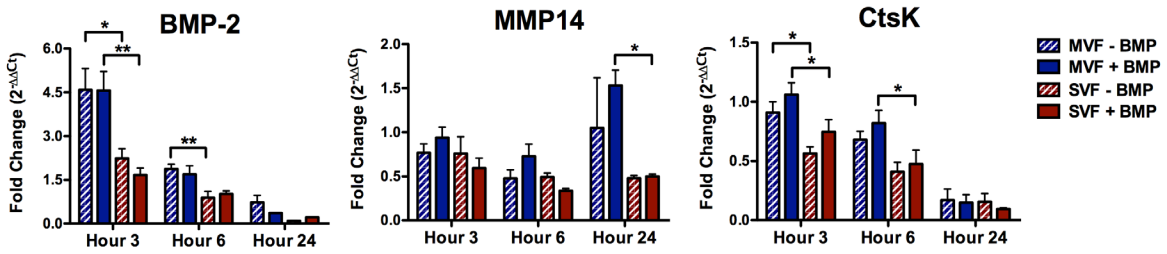

Figure 3.4. Gene expression of MVF and SVF in collagen sponge. MVF expression of BMP-2 and CtsK were significantly greater than that of SVF at hours 3 and 6. MVF expression of MMP14 was significantly greater than that of SVF at hour 24. 2-way ANOVA within time point; n=5/group/time point. * indicate post-hoc differences with $p<0.05$, ** $p<0.01$.

3.3.5 BMP-2-Primed 2D Culture

In a culture setup designed to mimic the MVF dissociation observed in collagen sponges, MVF were plated directly onto TCPS and allowed to dissociate to single cells (Figure 3.5 A). Dissociated MVF that were first primed with BMP-2 for 24 hours then released approximately 25 ng of BMP-2 into fresh culture media (e.g. no additional exogenous BMP-2 added) within the first 24 hours of culture and approximately 6 ng between hours 24 and hour 96 of culture (n=3; Figure 3.5 B). This was significantly more BMP-2 than was recovered from BMP-2 primed SVF plated on TCPS ($p<0.001$), which released approximately 2.5 ng BMP-2 within the first 24 hours and approximately 0.8 ng between hours 24 and 96. Non-primed cells, MVF and SVF, did not release any detectable BMP-2 into fresh media over the culture period.

BMP-2 gene expression was also measured following exogenous BMP-2 priming. At 24 hours following the BMP-2 priming, MVF expression of BMP-2 was significantly

greater than that of SVF (overall effect, $p<0.05$; Figure 3.5 C). However, there was no difference in gene expression due to BMP-2 priming. There were no significant differences in BMP-2 gene expression at hour 96 following the BMP-2 priming period.

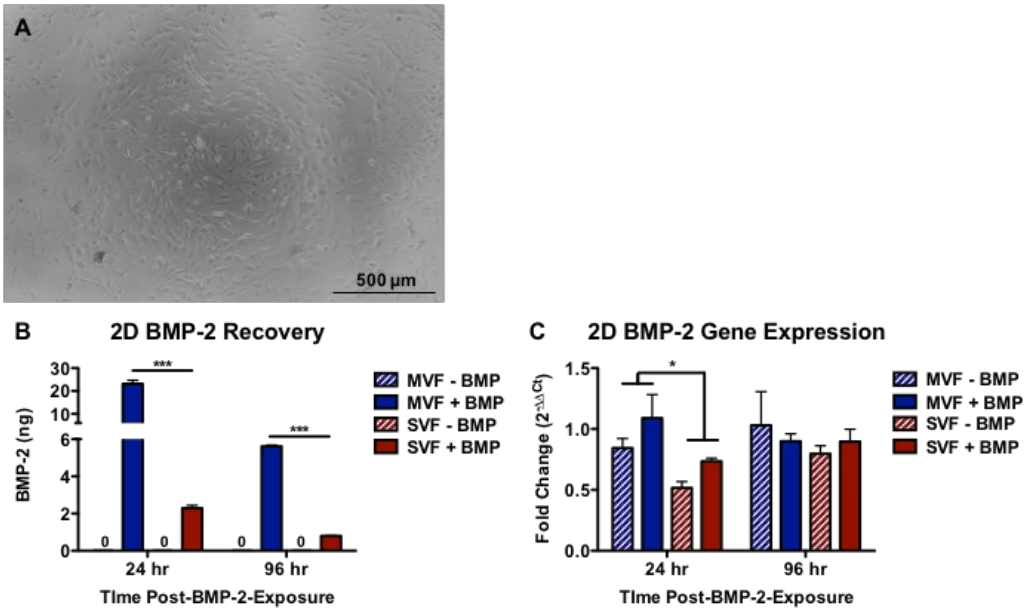

Figure 3.5. BMP-2 recovery and gene expression from 2D TCPS culture system. A) MVF were cultured on TCPS to allow dissociation to single cells. B) Dissociated MVF primed with BMP-2 released significantly more BMP-2 into fresh media than BMP-2-primed SVF (*** post hoc, $p<0.001$), while non-primed cells of either type did not release any detectable BMP-2. C) At 24 hours post BMP-2 priming, MVF had significantly greater BMP-2 expression than SVF (* overall effect, $p<0.05$), but there was no effect of BMP-2 priming on BMP-2 expression of MVF or SVF.

3.3.6 Pilot in vivo Study

At the 12 week end point, bone volume was significantly higher in the BMP-2 and BMP-2+MVF groups than in the sponge only negative control ($p<0.05$; Figure 3.6 A).

BMP-2+SVF was not significantly different than the negative control. There were no statistically significant differences in failure strength or stiffness among treatment groups. However, the average of the BMP-2+MVF group approached those of historical bone-only injuries treated with BMP-2 [42], shown by the dashed blue line in Figure 3.6 B-C, whereas the BMP-2+SVF group more closely matched historical values for composite injuries treated with BMP-2 [42], shown by the dashed green line.

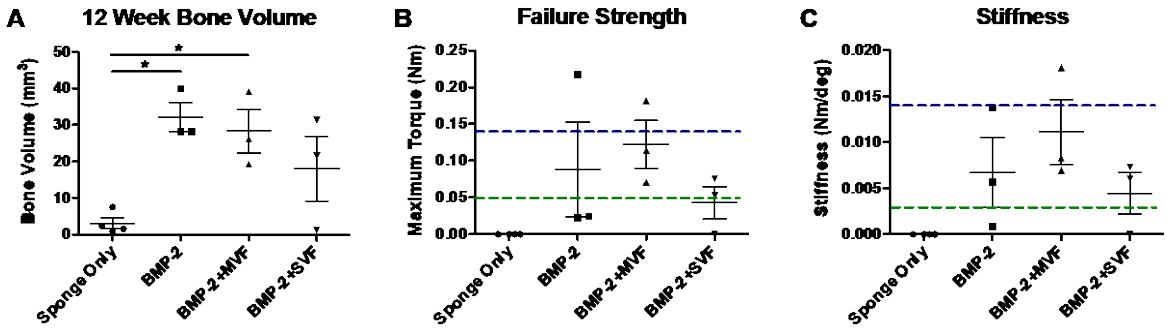

Figure 3.6. Pilot bone regeneration in composite defects treated with collagen sponge. A) Bone Volume (1-way ANOVA, * indicates $p<0.05$), B) Failure strength defined as maximum torque at failure, C) Regenerate bone stiffness defined as the slope of the linear region of torque vs. rotation.

3.4 Discussion

In this chapter, we aimed to develop a clinically translatable tissue engineering construct to deliver multicellular MVF or single cell SVF along with BMP-2 on collagen sponge. We found that MVF and SVF, while obtained from the same tissue source, are composed of different proportions of cellular subpopulations. Both MVF and SVF remained viable within the collagen sponge, but multicellular MVF dissociated to single cells within collagen sponge rather than the sprouting angiogenesis they exhibit in collagen

hydrogels. We observed that significantly more BMP-2 was recovered from constructs containing MVF than those containing SVF and subsequently hypothesized that MVF may have increased BMP-2 recovery from constructs due to production of BMP-2 or due to increased protease activity. In a pilot in vivo experiment, BMP-2+MVF treatment produced significantly greater bone volume than the collagen sponge only negative control, whereas there was no difference between the BMP-2+SVF treatment and the negative control.

Although MVF and SVF were isolated from the same adipose tissue source, the different digestion times, 7 minutes for MVF and 30 minutes for SVF, and filtration sizes, multicellular MVF are between 50-500 μm while SVF are single cells smaller than 50 μm, result in different cellular subpopulations. MVF were composed of a higher proportion of endothelial cells, while more stromal cells such as MSC, SMC, and pericytes comprised SVF. During the digestion process, some perivascular cells may have been detached from their vascular structures. These cells would then have been filtered out of MVF but remain within SVF, increasing their relative abundance in SVF vs. MVF. Additionally, adipose tissue is a widely recognized source of MSCs [67, 196-198], and adipose-derived MSCs have been shown to occupy a perivascular niche [199]. Thus, they too may become detached from their vascular structures and removed during the digestion and filtration process to obtain MVF.

When cultured within collagen sponge, both MVF and SVF remained viable for at least 14 days. However, MVF dissociated into single cells around day 3 of culture prior to reforming tubular networks by day 9-14. This is in contrast with the sprouting angiogenesis of MVF typically observed in collagen gels [107, 113]. The macroporous structure of

collagen sponge may have created asymmetric cell-matrix contacts (e.g. only one side of a vessel fragment may have been in contact with the matrix, while the opposite side was in direct contact with media) that destabilized the tubular structure of MVF. Since the cells that primarily comprise MVF are contact-dependent, cells may have dissociated from the vascular structure, migrated to bind extracellular matrix, and thus maintained viability.

Approximately 25-30% of the loaded BMP-2 was recovered from acellular and SVF-containing collagen sponges, which is consistent with previous results from acellular collagen sponge [194] and from other materials such as alginate hydrogels [200, 201]. In contrast, nearly 75% of the loaded quantity of BMP-2 was recovered from MVF-containing collagen sponges, suggesting that MVF uniquely modulate BMP-2 recovery. However, MVF-containing collagen gels did not show increased BMP-2 recovery compared to acellular collagen gels. MVF dissociated within collagen sponge but retained their tubular structure within collagen gel, suggesting that dissociation is a likely stimulus for the increased BMP-2 recovery phenomenon observed in collagen sponge. We hypothesized that dissociating MVF may exhibit elevated protease activity that frees BMP-2 bound to the collagen sponge and/or directly produce BMP-2. Interestingly, previous work has shown that vascular cells [202] such as endothelial cells, the primary cellular component of MVF, can produce BMP-2 in response to exogenous BMP-2 [98].

Gene expression of MVF and SVF cultured in collagen sponges with or without BMP-2 showed that MVF expressed significantly higher levels of BMP-2 than SVF at hours 3-6. However, there were no differences in BMP-2 expression in MVF cultured with vs. without exogenous BMP-2. Since increased BMP-2 recovery was only observed in collagen sponges containing exogenous BMP-2, the gene expression data suggest that

cellular production of BMP-2 was not likely responsible for the increased BMP-2 recovery. Although there is post-transcriptional modification of BMP-2 [203], the magnitude of difference between gene expression levels and protein levels was much higher than would typically be attributed to post-transcriptional mechanisms. MVF also expressed significantly greater levels of proteases than SVF. MVF expressed higher levels of CtsK, the most prevalent mammalian collagenase [204], at hours 3 and 6, and higher levels of neovessel-specific MMP14 [195] at hour 24. However, again there were no differences due to presence of BMP-2. This combined with the fact that the fold changes in gene expression were all well below common thresholds (e.g. 2-fold) of biological significance suggest that these proteases were also not responsible for the increased BMP-2 recovery.

To replicate the MVF dissociation observed in collagen sponges, we cultured MVF on TCPS, which forced their dissociation into single cells. Both MVF and SVF were cultured on TCPS with or without 500 ng BMP-2 for a 24 hour priming period. Following priming and three washes, significantly more BMP-2 was recovered from media from BMP-2-primed MVF than BMP-2-primed SVF. The approximately 1-2 ng of BMP-2 recovered from BMP-2-primed SVF media may be residual BMP-2 bound to cells or the well plate and not removed by washes. However, an order of magnitude more BMP-2 was recovered from BMP-2-primed MVF. This provides additional support for the observation that dissociation of MVF is a key element of their augmented BMP-2 recovery. As in the collagen sponge, MVF had a higher overall expression of BMP-2 than SVF 24 hours after the BMP-2 priming period, but there was no effect of BMP-2 priming on BMP-2 gene expression. This further supports that MVF are not increasing BMP-2 recovery due to BMP-2 production. The recovery of significantly more BMP-2 from MVF in a 2D culture

setup without a large amount of extracellular matrix like the collagen sponge suggests that increased activity of proteases, even those not included in the gene expression analysis, was not responsible for the increased BMP-2 recovery.

Overall, the dissociation of multicellular MVF in the presence of exogenous BMP-2 led to increased recovery of BMP-2 in the surrounding media, both when cultured within collagen sponge and on TCPS. When exogenous BMP-2 was not present, dissociating MVF did not release any detectable BMP-2 into their media. While early gene expression of BMP-2 was elevated in MVF relative to SVF, there was no difference in BMP-2 gene expression in MVF cultured with vs. without BMP-2, suggesting that MVF dissociating in the presence of BMP-2 do not produce additional BMP-2. While there were statistically significant differences in MVF vs. SVF protease gene expression, there were again no differences due to the presence of BMP-2. This combined with replication of the augmented BMP-2 recovery on TCPS that lacks substantial extracellular matrix material to be degraded suggests that increased protease activity was not responsible for the increased BMP-2 recovery. Despite not elucidating the mechanism for augmented BMP-2 recovery from MVF, the replication of this phenomenon in independent experiments and in different culture environments increases confidence that it is a consistent phenomenon. Multicellular MVF, which have more extensive native extracellular matrix, may bind exogenous BMP-2 and release it upon dissociation. This hypothesis could be tested in future work by using fluorophore-labeled BMP-2 and imaging to determine whether BMP-2 colocalizes with labeled MVF.

Finally, we implanted collagen sponges containing BMP-2 and MVF or SVF to a model of composite bone-muscle injury that exhibits attenuated bone healing [42] and

decreased revascularization following injury [43, 44]. Even in a pilot sized experiment, constructs containing BMP-2 only and BMP-2+MVF achieved significantly higher bone volume than the collagen sponge only negative control; the BMP-2+SVF group was not statistically different than the negative control. Although there were no statistically significant differences in mechanical properties among any treatment groups, the average torque to failure and stiffness were greatest in the BMP-2+MVF group. Additionally, the mechanical properties of the BMP-2+MVF group approached those of historical values for bone-only injuries [42]. This promising result suggests that co-delivery of MVF and BMP-2 may be able to overcome the bone healing deficit observed in composite bone-muscle injuries, perhaps through a combination of increasing vascularization and by increasing the availability of BMP-2.

3.5 Conclusions

Dissociation of multicellular MVF in the presence of exogenous BMP-2 consistently led to increased recovery of BMP-2 in the surrounding media. Although our hypotheses that this could be due to MVF production of BMP-2 or increased protease activity in MVF were not supported, increased recovery of BMP-2 was consistently observed across different culture environments. MVF may bind exogenous BMP-2 and release it upon dissociation. In a pilot sized in vivo experiment, BMP-2 and BMP-2+MVF produced significantly greater bone volume than the collagen sponge only negative control, while BMP-2+SVF was not statistically different than the negative control. Although not statistically significant, the mechanical properties of the BMP-2+MVF approached

historical data for those of bone-only injuries. Thus, the co-delivery of BMP-2 and MVF on collagen sponge in vivo is a promising approach that may improve bone healing, possibly overcoming the attenuation in bone healing observed in composite defects, by both enhancing vascularization and by increasing BMP-2 availability.

CHAPTER 4. EFFECTS OF BMP-2 DOSE AND DELIVERY OF MICROVASCULAR FRAGMENTS ON HEALING OF BONE DEFECTS WITH CONCOMITANT VOLUMETRIC MUSCLE LOSS [2]

4.1 Introduction

Composite tissue injuries present a compelling clinical challenge to both military and civilian trauma populations. Of the six million fractures that occur in the U. S. each year, approximately 10% are open fractures, which are characterized by concomitant soft tissue damage. These injuries experience a complication rate about twice that of closed fractures, with complications including infection, malunion, and non-union [35]. As a result, open fractures are often subject to multiple treatment strategies, repeated surgeries, and high direct and indirect costs [188]. Despite these multiple interventions, nearly two-thirds of patients remain significantly disabled long term (at seven years post-injury, and likely beyond) [51].

One treatment strategy often employed in challenging bone healing scenarios is the delivery of bone morphogenetic protein-2 (BMP-2) on a collagen sponge. While most commonly used in cases of spinal fusion [69], BMP-2 has demonstrated clinical success in long bone fracture cases for over 15 years [70]. However, BMP-2 has also been linked to

[2] Adapted from M.A. Ruehle, et al. Effects of BMP-2 dose and delivery of microvascular fragments on healing of bone defects with concomitant volumetric muscle loss, Journal of orthopaedic research, 2019. 37(3): p. 553-561. Reproduced with permission: license number 4541971103840.

side effects such heterotopic bone formation and inflammation [73], both of which can be exacerbated by orthopaedic trauma [205]. Segmental bone defect healing is known to exhibit a dose response to BMP-2 [193]; however, a minimally bridging dose for a segmental bone defect was unable to consistently bridge same-sized bone defects in a composite bone and muscle defect model [42]. Thus, the effect of BMP-2 dose is of particular interest in traumatic composite defects.

The Gustilo classification system scores open fractures from class I-IIIC in terms of increasing severity. Assignment to broad classes I-III is determined by increasing size of soft tissue loss, but the hallmark of the most severe category IIIC is vascular damage – regardless of the degree of soft tissue damage [38]. The revascularization process is a rate-limiting step of the wound healing [10] and plays a crucial role in the clinical success of treatments for open fractures. Further, it is well established that angiogenesis and osteogenesis are linked [16] and that impaired revascularization impairs fracture healing in pre-clinical animal models [15]. Numerous therapeutic strategies targeting revascularization of bone have been employed, largely pre-clinically, including growth factor and cell delivery [92, 100, 103].

One promising approach is the use of microvascular fragments (MVF), multicellular segments of mature vasculature that form angiogenic networks in vitro [107]. Due to their pre-patterned tubular structure and retention of vascular support cells, MVF are attractive candidates for tissue engineering applications [206]. MVF have been shown to inosculate with host vasculature [195, 207], increase tissue vascular volume [116, 195] and improve tissue grafting in pre-clinical models [118, 119]. MVF are most commonly obtained from adipose tissue and therefore have potential clinical utility in an autologous application.

We have previously developed a pre-clinical small animal model of composite bone-muscle injury consisting of a critical size femoral defect with an overlying volumetric muscle loss [42]. Our model recapitulates the clinical observation of impaired bone healing when concomitant soft tissue injury is present, and this has also been seen in similar pre-clinical models of composite tissue injury [40-42, 208]. In this study, we tested the hypotheses that BMP-2-mediated functional regeneration of composite extremity injuries is dose dependent and can be further enhanced via co-delivery of adipose-derived microvascular fragments (MVF), which have been previously shown to increase tissue vascular volume.

4.2 Methods

4.2.1 MVF Isolation and Construct Preparation

MVF were isolated as previously described [107]. Briefly, epididymal fat pads were harvested from two retired breeder Lewis rats to yield approximately 10-12 mL fat tissue. Fat was minced, and digested with a collagenase solution for 7 minutes at 37 °C. MVF were obtained through selective filtration to retain tissue between 50-500 μm. To prepare surgical constructs, MVF were suspended at a density of 80,000 MVF/mL in αMEM (ThermoFisher Scientific; Waltham, MA) along with BMP-2 (Pfizer, Inc.; New York, NY) and pipetted dropwise onto collagen sponges (5 mm diameter, 1 cm height; Kensey Nash/DSM; Exton, PA).

Viability of constructs cultured in αMEM with 10% fetal bovine serum (FBS; Atlanta Biologics; Atlanta, GA) and 1% penicillin-streptomycin-L-glutamine (ThermoFisher) was evaluated using a live/dead assay kit according to manufacturer's instructions (ThermoFisher). Cylindrical constructs were cut in half lengthwise to expose the center of the sponge immediately prior to imaging. Three constructs were imaged per time point at days 1, 3, 7, 9, and 14 of culture. Viability was quantified using the ImageJ 3D objects counter to compare the number of objects in the red channel of the image vs. the green channel.

4.2.2 Surgical Procedure

Unilateral composite defects were made in 13-week-old female Lewis rats (Charles River Laboratories; Wilmington, MA) by creating an internally stabilized 8 mm defect in the mid-diaphysis of the femur with an overlying 8 mm diameter full-thickness quadriceps defect as previously described [42]. Collagen sponges (5 mm diameter, 1 cm height) loaded with BMP-2 ± MVF were press fit into the defect. Sponges contained 2.5 μg BMP-2 without MVF (n=8 animals), 2.5 μg BMP-2 with MVF (n=8), 10 μg BMP-2 without MVF (n=9), or 10 μg BMP-2 with MVF (n=10). Animal number was determined from previous studies of segmental bone defect healing, and animals were randomly assigned to treatment groups. Animals were double-housed, maintained on a 12-hour light/dark cycle, and allowed ad libitum access to food and water. At 12 weeks post-surgery, animals were euthanized by CO_2 inhalation. All animal experiments were performed in accordance with

the Georgia Institute of Technology Institutional Animal Care and Use Committee (IACUC).

4.2.3 Bone Regeneration Analyses

Bone healing was qualitatively assessed by radiography at 2, 4, 8, and 12 weeks post-surgery and quantitatively assessed by micro-computed tomography (μCT) at 4, 8, and 12 weeks post-surgery. The defect region was scanned with a voxel size of 38.9 μm. The middle 6.5 mm of the defect was analyzed, and bone volume was quantified by Scanco software using a threshold corresponding to 50% of intact cortical bone [42, 193]. Polar moment of inertia was calculated for each μCT slice as a measure of the distribution of bone relative to the central axis using a Scanco evaluation script [209]. An average of all slices' polar moment of inertia was calculated to determine a global value for each sample [194].

Mechanical testing and histology were performed at the 12 week endpoint after euthanasia. Thighs were harvested, soft tissue was cleared, and fixation plates were removed. Femur ends were potted in Wood's metal (Alfa Aesar) and tested in torsion at a rate of 3°/s to failure (ELF 3200, TA ElectroForce) [61]. Maximum torque (torque at failure) and torsional stiffness (linear region of torque vs. rotation) were calculated for all samples.

Following mechanical testing, one sample from each group was fixed in 10% neutral buffered formalin (NBF) for 24 hours and decalcified in a formic citrate solution

(Newcomer Supply, Inc; Middleton, WI). Bone and muscle tissues were embedded in paraffin and sectioned at a thickness of 5 μm. Bone tissue was stained with hematoxylin and eosin (H&E); muscle tissue was stained with H&E and with Masson's Trichrome to observe fibrosis (Histotox Labs; Boulder, CO). Bone sections were also stained with rhodamine-labeled Griffonia simplicifolia lectin I (GS-1 lectin; Vector Laboratories; Burlingame, CA) at a concentration of 10 μg/mL and counterstained with DAPI (ThermoFisher) diluted 1:1000 in phosphate buffered saline to identify blood vessels.

4.2.4 Serum Cytokine Quantification

At the week 12 endpoint, blood was collected via the rat tail vein from a subset of animals from each treatment group (n=5/group). Serum was collected from whole blood for multiplexed analyte analysis for 27 inflammatory cytokines and chemokines. Samples were prepared using a multiplexed rat cytokine/chemokine magnetic bead panel (MILLIPLEX RECYTMAG-65K), according to manufacturer's instructions. Data was collected using a MAGPIX multiplexing system (Luminex Corporation; Austin, TX).

4.2.5 Statistical Analysis

Data were analyzed using GraphPad Prism 7 and are represented as mean ± standard error of the mean (SEM). Bone volume, maximum torque, torsional stiffness, and cytokine levels were analyzed by two-way analysis of variance (ANOVA) and Bonferroni post-hoc tests with an alpha level of 0.05.

4.3 Results

4.3.1 Construct Viability

MVF cultured in BMP-2 loaded collagen sponges maintained viability in vitro throughout the three-dimensional construct (Figure 4.1). However, multicellular MVF appeared to dissociate to single cells by day 3 of culture and reform networks by day 9-14. Approximately 65% of the cells were viable at day 3; over 90% of cells were viable at days 7-14.

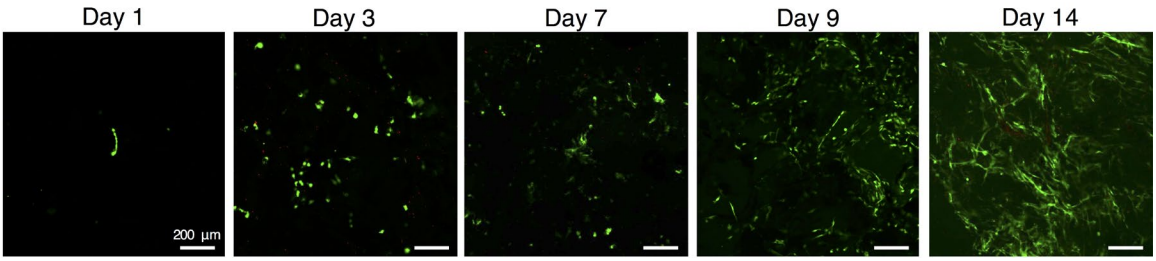

Figure 4.1. MVF Viability in Collagen Sponge. Representative images of MVF cultured in collagen sponge with BMP-2 at days 1, 3, 7, 9, 14. Images were acquired from the center (longitudinal cross section) of the 5 mm diameter sponge. Green, calcein – live, red, ethidium homodimer – dead. MVF dissociated to single cells by day 3 and reformed networks around day 9-14.

4.3.2 Bone Regeneration

4.3.2.1 Radiography and μCT

Radiographs demonstrated that a majority of defects bridged in all four treatment groups (Figure 4.2). By 12 weeks, all defects treated with 10 μg BMP-2, with and without

MVF, had bridged (nine of nine and ten of ten, respectively). Seven of eight defects treated with 2.5 µg BMP-2 without MVF bridged, and five of eight defects treated with 2.5 µg BMP-2 with MVF bridged. Bone volume in the defect region was measured by µCT and was significantly higher in the 10 µg dose groups than in the 2.5 µg dose groups (Figure 4.3 A; overall effect, p=0.0312). There was no effect of the MVF treatment on bone volume and no significant interaction. The polar moment of inertia was also calculated as a measure of the distribution of bone relative to the central axis. pMOI was significantly lower in the 2.5 µg dose groups (Figure 3B; overall effect, p=0.0047). This corresponds to the more compact morphology observed in the radiographs (Figure 4.2) and µCT reconstructions of the 2.5 µg dose groups (Figure 4.3 C). Bone density was approximately 870 mm hydroxyapatite/cm^3 for all four groups.

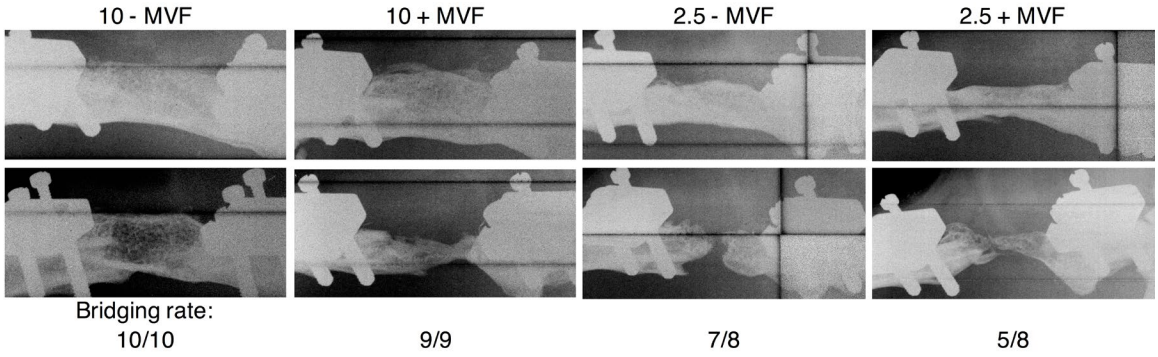

Figure 4.2. Representative relatively well healed and poorly healed 12-week radiographs of defects treated with BMP ± MVF in collagen sponge. Well healing samples are shown on top, and poorly healed samples are shown on bottom. Bridging rate by group is shown below.

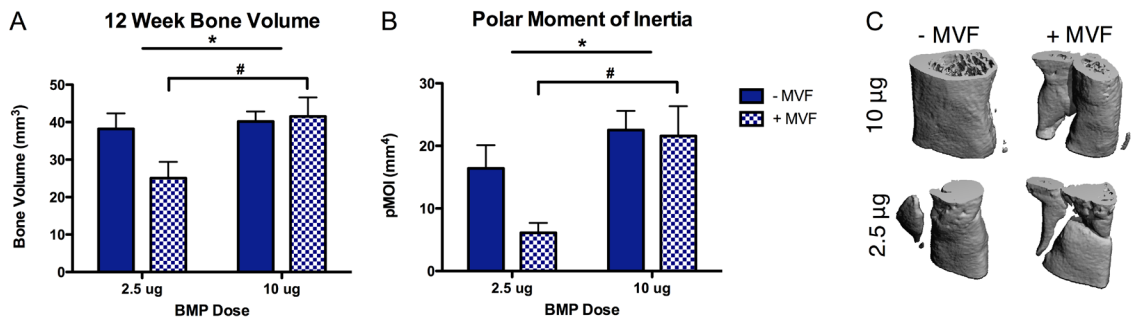

Figure 4.3. 12-week bone volume data for defects treated with BMP ± MVF in collagen sponge. A) Bone volume and B) polar moment of inertia of defects as measured by µCT. C) Representative µCT reconstructions of defects from each treatment group that exhibited similar bone volume (~35-40 mm^3) but different morphologies. * overall effect of BMP dose, $p<0.05$; # post-hoc $p<0.03$; 2-way ANOVA; n=8-10/group.

4.3.2.2 Mechanics

The torque to failure was significantly higher for the 10 µg dose BMP-2 groups than the 2.5 µg dose groups (Figure 4.4; post hoc, $p<0.001$). There was no effect of MVF and no significant interaction. Despite the increased strength of the 10 µg BMP-2 treatment, the 10 µg dose without MVF group still only achieved 60.5% of intact strength. Stiffness was also significantly higher in the 10 µg dose groups than in the 2.5 µg dose groups (overall effect, $p=0.0005$), and stiffness was significantly decreased in groups with MVF compared to without MVF (overall effect, $p=0.0098$).

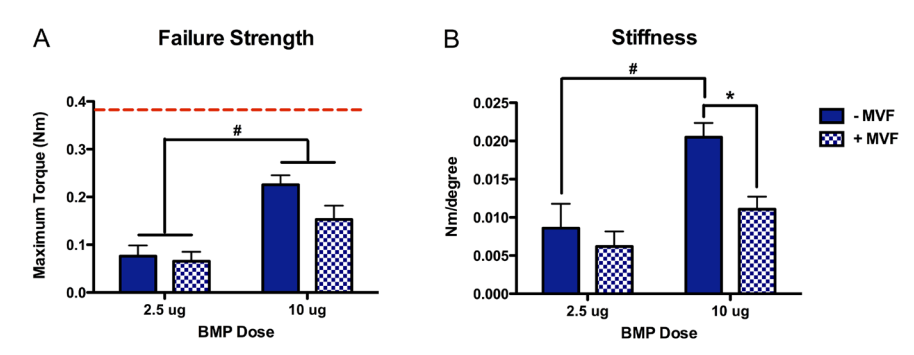

Figure 4.4. Mechanical properties of defects treated with BMP ± MVF in collagen sponge. Failure strength and B) stiffness of bone regenerated at 12 weeks. Dashed red line indicates failure strength of intact contralateral femur. # post-hoc differences due to BMP dose, $p<0.001$; * post-hoc differences due to MVF, $p<0.01$; 2-way ANOVA; n=8-10/group.

4.3.2.3 Histology

Qualitative histological assessment of bone defects supported the quantitative µCT data. The 10 µg dose without MVF group showed the greatest amount of bone organized in apparent lamellae, and both groups that received MVF showed larger areas of non-mineralized, marrow-like tissue (Figure 4.5). There were no qualitative differences in relative number of lectin-stained blood vessel structures among treatment groups at the 12 week time point (Figure 4.6). As expected, the untreated muscle defects did not heal over the course of this study. At the 12 week end point, muscle exhibited a large degree of fibrosis and fatty infiltration (Figure 4.7). No qualitative differences in muscle healing were apparent between the well healing 10 µg BMP-2 without MVF and poorly healing 2.5 µg BMP-2 with MVF groups.

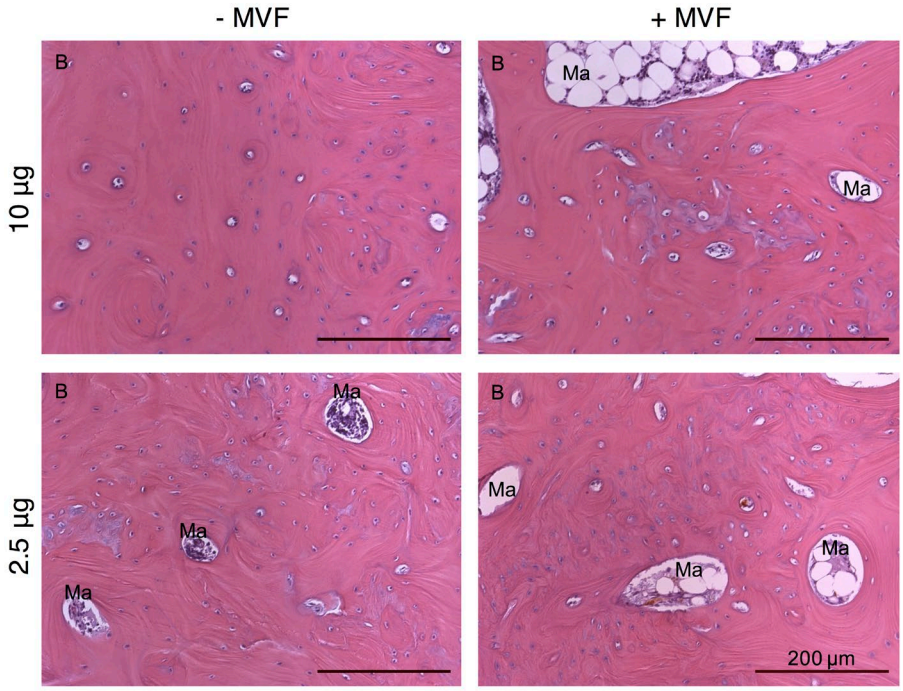

Figure 4.5. Hematoxylin and eosin staining of bone tissue regenerated by 12 weeks in defects treated with BMP ± MVF in collagen sponge. The 10 µg without MVF group appears the most organized into apparent lamellae, while the other groups are less organized and contain larger areas of non-mineralized, marrow-like tissue (Ma) within the mineralized bone (B).

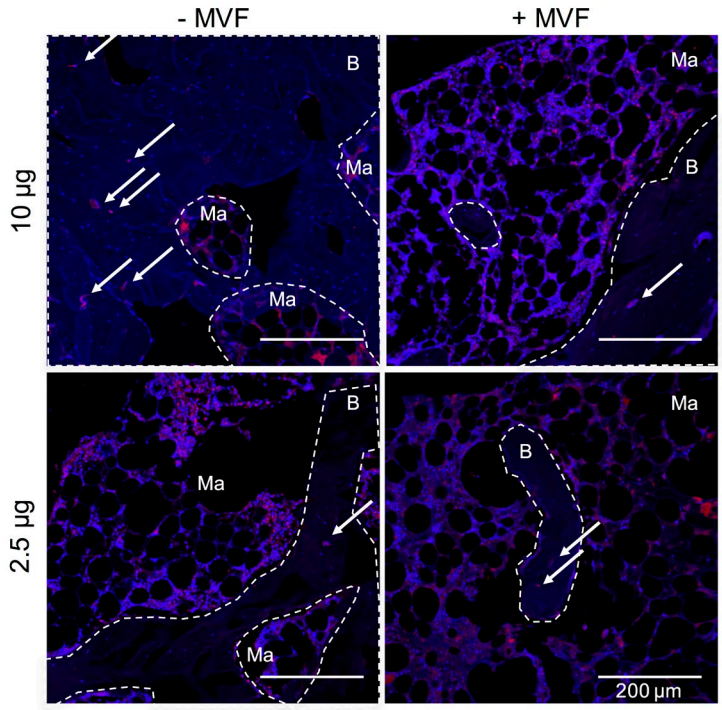

Figure 4.6. GS-1 lectin staining for blood vessels within regenerate bone at 12 weeks from defects treated with BMP ± MVF in collagen sponge. Dashed line demarcates mineralized bone (B) vs. marrow-like tissue (Ma). White arrows indicate blood vessels within mineralized tissue. Red, GS-1 lectin – vessel glycocalyx; blue, DAPI – nuclei.

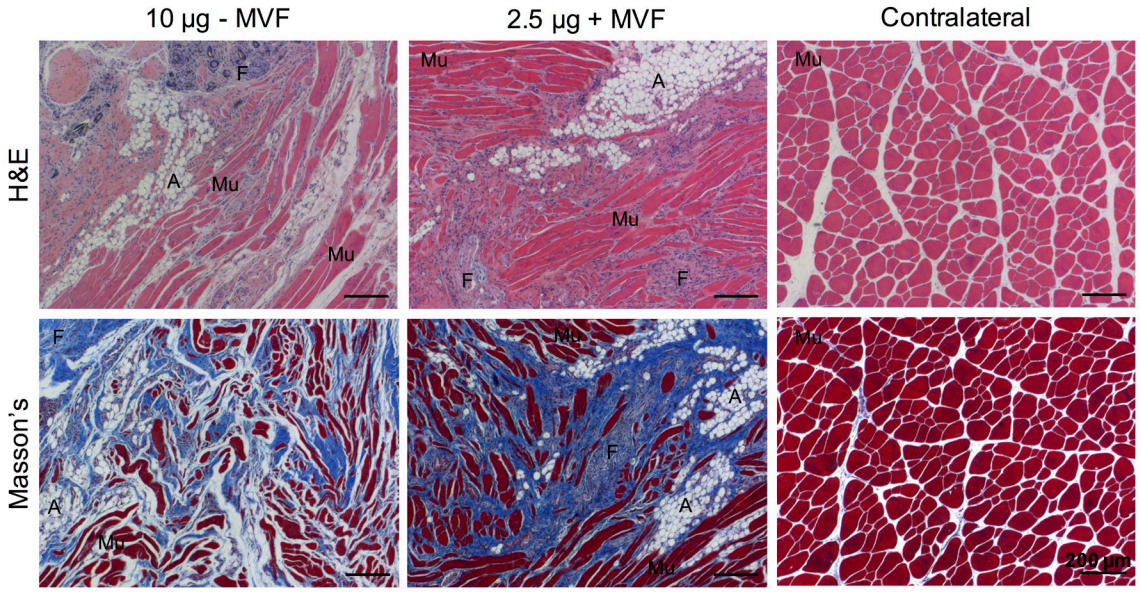

Figure 4.7. H&E and Masson's trichrome staining of muscle tissue from treatment groups with well healed bone and poorly healed bone alongside uninjured

contralateral muscle tissue. Well healed samples are from the 10 µg - MVF group, and poorly healed samples are from the 2.5 µg + MVF group. Masson's: red – muscle fibers, blue – fibrotic tissue. Muscle fibers (Mu), fibrotic tissue (F), and adipose infiltration (A) are denoted.

4.3.3 Serum Cytokine Quantification

Blood was collected at the 12 week end point to quantify systemic levels of circulating inflammatory cytokines (n=5/group). Levels of multiple interleukins (IL) were significantly decreased in blood samples taken from animals treated with the increased 10 µg BMP-2 dose groups, both with and without MVF (Figure 4.8). Both pro-inflammatory interleukins, such as IL-1a and IL-1b, and anti-inflammatory interleukins, such as IL-5, IL-10, and IL-13, [210] were decreased in the 10 µg BMP-2 dose groups. Pro-inflammatory eotaxin was also lower (p=0.0507) in the 10 µg BMP dose groups.

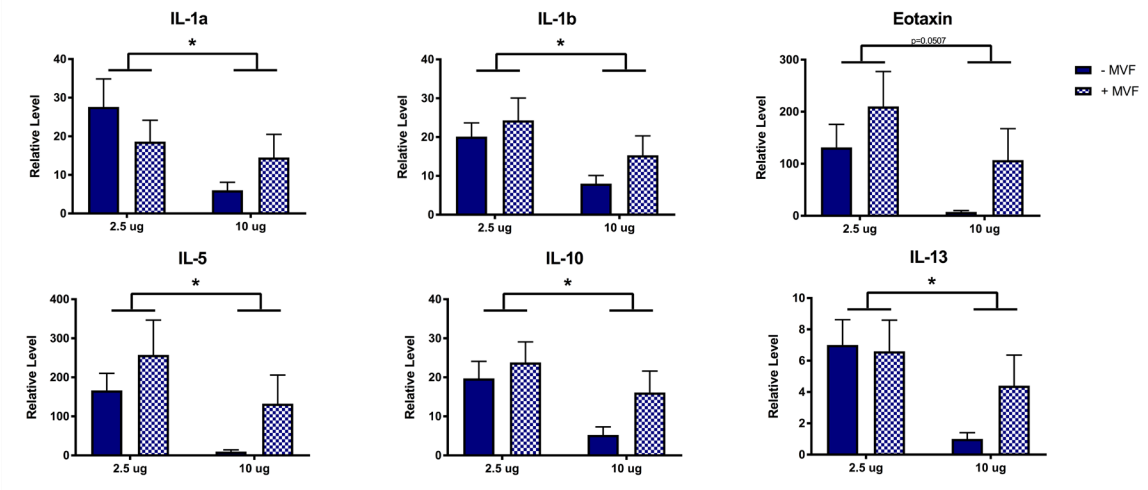

Figure 4.8. Relative serum levels of pro- and anti-inflammatory cytokines by treatment group as measured by multiplexed analyte analysis. Pro-inflammatory cytokines on top and anti-inflammatory cytokines on bottom. * post-hoc differences due to BMP dose, $p<0.05$; 2-way ANOVA; n=5/group.

4.4 Discussion

Composite tissue extremity injuries represent a significant challenge to orthopaedic surgeons and a momentous hardship for patients. Vascularization is an enabling step of wound healing, and we hypothesized that BMP-2-mediated functional regeneration of composite extremity injuries would be dose dependent and could be further enhanced via co-delivery of adipose-derived microvascular fragments (MVF), which have been previously shown to increase tissue vascular volume.

BMP-2 is clinically approved for a number of bone healing indications and has shown success in treating long bone fractures and non-unions [70, 211]. There is a BMP-2 dose response in humans and in pre-clinical animal models, but precise dosing required for specific human applications is not well defined [193, 211]. High BMP-2 dosage has been linked a number of side effects including heterotopic ossification (HO) and increased inflammation [73], and HO is also often increased in cases of trauma [212-214]. While a 2.5 μg dose of BMP-2 is a bridging dose in a segmental defect model [193], it produces inconsistent bridging in this challenging composite defect model [42]. In this segmental defect model, HO has been observed at 30 μg doses of BMP-2 [194, 200]. We showed in the present study that a 10 μg dose is sufficient to improve composite defect healing relative to the 2.5 μg dose and does not lead to mineralization outside the collagen sponge delivery vehicle. A moderately increased dose (e.g. 10 μg relative to 2.5 μg or 30 μg) may be required in composite injuries to compensate for the loss of endogenous stem and progenitor cells and growth factor availability as a result of the concomitant muscle loss. When scaled by body surface area (assuming a 60 kg human relative to a 0.25 kg rat), a 2.5 μg rat dose would be equivalent to 0.114 mg in humans, and a 10 μg dose would be

equivalent to 0.454 mg [215]. This is lower than the current FDA approved dose of BMP-2 for tibial fractures of 12 mg [70]. However, there is known species variation for BMP-2 dose specifically, with sheep requiring higher doses than rodents and non-human primates requiring higher doses still [216]. Together, these studies demonstrate the need for precise identification of the appropriate clinical dosing window of BMP-2. While muscle loss constitutes an increased level of trauma, this model does not incorporate head trauma or muscle crush, which are known contributors to human post traumatic HO [213, 214]. Traumatically injured muscle can give rise to osteogenic progenitor cells [214], but it is unknown whether a similar effect would be present in this model which cleanly removes a volumetric section of muscle with a biopsy punch. While large volume muscle loss has been shown to have a more profound impact on bone healing than muscle crush injuries [217], the VML model utilized here may not fully recapitulate the HO risk associated with trauma of clinical open fractures that often also have significant muscle damage. Future work may be warranted to investigate more aggressive debridement of damaged muscle adjacent to bone injuries as prophylaxis for HO, though this could potentially lead to reduced functional outcomes.

Local healing at the site of a regenerative intervention, as well as HO, are both thought to be influenced by the systemic immune response. Interestingly, the 10 μg BMP dose resulted in lower levels of both pro- and anti-inflammatory systemic cytokines relative to the 2.5 μg dose at the 12-week time point. The 2.5 μg dose group's failure to completely heal may have prolonged the inflammatory stage of the wound healing process, which previous studies have shown to be increased in composite tissue injuries [40]. That persistent local inflammation may then have resulted in altered systemic immune cytokine

profiles. Rather than a high BMP dose inducing inflammation, the successful bridging and restoration of function may have resolved the local inflammation and led to lower cytokine levels by the 12 week time point. Future studies investigating inflammatory profiles at earlier time points would be required to more definitively address the composite injury's inflammatory response to various BMP doses.

MVF were used as a proposed therapeutic approach to enhance revascularization and subsequently bone regeneration; however, the MVF treatment did not improve bone volume or failure strength and in fact decreased the stiffness of the regenerated bone. Although MVF treatment had no significant effect on bone volume, the mineralization pattern of the regenerated bone appeared more fragmented in MVF-treated defects as observed with μCT. The fragmented mineralization of MVF-treated groups may have contributed to the differences in mechanical properties. MVF have been shown to improve tissue vascularization and integration; however, this has been primarily demonstrated in subcutaneous implantation [195], skin flaps [218], and dermal substitutes [118, 119], all of which are considerably thinner and thus closer to native vascular sources than the critical size bone defect used here. MVF have also been shown to increase tissue perfusion in VML models when delivered in collagen gel [116, 117], which allows for sprouting angiogenesis [107, 110, 116, 219]. In this study, while in vitro viability of MVF was maintained in collagen sponge, the multicellular MVF first dissociated to single cells and then reformed networks. This is not consistent with the sprouting angiogenesis typically observed within a collagen gel and may have contributed to the lack of effect of MVF on bone healing. While collagen sponge is a clinically available BMP-2 delivery vehicle, it may not be an optimal delivery vehicle for MVF, which are exquisitely sensitive to extracellular matrix

properties [110, 112]. Further, MVF exert traction forces on their matrices and can contract collagen hydrogels [107, 113, 219]; cell-mediated contraction of collagen sponge may have contributed to the more fragmented mineralization observed in the MVF-treated defects (Fig 3C).

Beyond the vascular components of adipose-derived MVF, these structures also contain mesenchymal stem cells (MSCs) [119, 220]. Exogenously delivered adipose-derived MSCs have previously been shown to negatively affect mineralization when co-delivered with BMP-2 [67]. While BMP-2 upregulates osteogenic signaling of bone marrow-derived MSCs, adipose-derived MSCs may differentially interact with BMP-2 to dampen or alter its signaling to endogenous host cells. However, adipose-derived MVF contain only about 2%-7% MSCs [108, 119], so their relative contribution may be proportionally small. Retention of other adipose-derived cells may have contributed to the larger marrow spaces histologically observed in MVF-treated defects (Figure 4.5), and adipose-derived MVF may not be suitable for bone defect applications.

Delivery of MVF also did not result in qualitative differences in lectin-stained blood vessel structures at 12 weeks. Cell implantation strategies broadly are challenged by issues of viability and retention [68, 106, 221]. Although vascularization is hypothesized to improve viability by enabling nutrient and oxygen transport, the implanted MVF may have failed to survive long enough to inosculate with the host vasculature – particularly due to their dissociation within the collagen sponge. Future studies to assess MVF retention, viability, and vascularization at earlier time points are required.

4.5 Conclusions

This is the first investigation of BMP-2 dose in a composite defect model. While the delivery of MVF did not improve bone healing in the composite defect model, an increased dose of 10 μg BMP-2 significantly improved bone healing and regenerate bone mechanics relative to a 2.5 μg dose. While 2.5 μg BMP-2 restored bone failure strength to only 20% of intact strength, a 10 μg BMP dose restored failure strength to 60% of intact. This improvement may represent significant functional improvements but also underscores the challenging nature of healing composite tissue injuries. Collagen sponge is a clinically approved, and therefore translationally relevant, BMP-2 delivery vehicle but may not be an appropriate MVF delivery vehicle. A modest increase in BMP-2 dosage may be a clinically relevant treatment strategy for critical size bone defects with concomitant muscle damage while a biomaterial delivery system for co-delivery of MVF is developed. Approaches that enhance early vascularization may be required to restore regenerated bone to greater than 60% of intact strength in cases of composite bone and muscle traumatic injury, and development of a more suitable biomaterial delivery vehicle may enable enhancement of early vascularization by MVF.

CHAPTER 5. DEVELOPMENT OF DECORIN-SUPPLEMENTED COLLAGEN HYDROGELS AS DIMENSIONALLY STABLE SCAFFOLDS [3]

5.1 Introduction

Vascular growth and remodeling are processes that are highly sensitive to mechanical cues; however, much of the existing research in this field has focused on luminal mechanics related to fluid flow (i.e. fluid shear and cyclic stretch) rather than abluminal stimulation of the vessel network itself [222]. Abluminal forces are particularly relevant to load-bearing tissues such as bone, and it is well established that angiogenesis and osteogenesis are intimately linked in both development and healing [11, 88]. Additionally, previous work in vivo showed that functional loading has a potent time-dependent influence on vascular growth during segmental bone defect healing; early loading impaired vessel growth, whereas delayed loading enhanced vascular growth [136]. Well-controlled in vitro studies are needed to better understand the mechanical cues associated with vascular growth and inhibition.

Microvascular fragments (MVF) are multicellular segments of vasculature that can sprout and form networks in vitro [107]. In combination with an appropriate 3D substrate, MVFs allow for interactions between multiple cell types and between cells and their

[3] Adapted from Ruehle, M.A., et al., Decorin-containing collagen hydrogels as dimensionally stable scaffolds to study the effects of compressive mechanical loading on angiogenesis. MRS Communications, 2017. 7(3): p. 466-471. Reproduced with permission: license number 4510920697725.

matrix, thereby better representing the complex in vivo processes of angiogenesis than models utilizing single cells or 2D substrates. Previous work utilizing MVF constructs has shown that they are sensitive to chemical cues, extracellular matrix (ECM) mechanical properties, and tensile forces [111-113]; however, they have yet to be studied under compressive forces. MVF are typically cultured in three dimensions within type I collagen gels, which contract significantly over time in culture [107, 113]. Gel contraction prevents longitudinal analysis of cultures, which is a serious limitation for studies aiming to investigate time-dependent effects. Thus, to study the role of a compressive mechanical environment on MVF growth over time in vitro, there is a need for a material substrate that both supports MVF growth and has greater dimensional stability than a low percentage collagen gel.

Although increasing the percentage of collagen within the gel increases structural stability, MVF growth is hindered at high collagen densities [113]. Crosslinking methods exist to chemically link the collagen fibrils rather than relying on physical interactions; however, unreacted crosslinking reagents can be cytotoxic and are therefore not amenable to cell encapsulation prior to crosslinking [223]. While synthetic materials offer advantages of tunability and batch-to-batch consistency, both scaffold development and MVF culture would require optimization, whereas MVF growth in collagen is quite well characterized. Thus, this research focused on techniques to modify the mechanical properties of collagen hydrogel constructs.

Decorin (DCN) is a small leucine-rich proteoglycan (SLRP) expressed in connective tissue that modulates collagen fibrillogenesis and alters the mechanical properties of collagen hydrogels [224-228]. A previous in vitro study demonstrated that

addition of DCN during collagen fibrillogenesis led to a denser fibril network with a higher tensile modulus [228]. Our objective here was to investigate the ability of DCN-supplemented collagen hydrogels to 1) support microvascular growth, 2) maintain dimensional stability throughout at least 14 days in culture, and 3) withstand physiologic compressive loads.

5.2 Materials and Methods

5.2.1 Decorin Purification

Methods for decorin purification were based on published protocols [228, 229]. Bovine knee ligament samples were frozen in liquid nitrogen and pulverized. The powder was suspended in an extraction solution [229] at 4 °C overnight before centrifugation at 20,000 g for 2 hours. The resulting supernatant was then sequentially filtered through a 1.1 μm glass fiber filter and a 0.45 μm regenerated cellulose filter. The filtrate was subjected to anion exchange chromatography over a POROS PI column at 4 °C. GAG-containing fractions were identified by dimethylmethylene blue (DMB) assay, pooled, concentrated via ultrafiltration, and purified by gel chromatography with a sepharose CL-4B column. GAG-containing fractions were pooled as above, and DCN-containing fractions were identified by SDS-PAGE [225] before ultrafiltration and buffer exchange. Hydrophobic chromatography was performed on the DCN fractions using an octyl-sepharose column at 25 °C. DCN-containing fractions were monitored and concentrated as above before buffer exchange into phosphate buffered saline (PBS) using PD-10 desalting columns. The

solution was sterilized by filtration. DCN purity was confirmed with SDS-Page [225], and concentration was determined by DMB assay.

5.2.2 Gel Formation and Characterization

Collagen gels were created from rat-tail type I collagen (Corning Life Sciences, Corning, NY). Collagen solutions, 3 mg/mL or 6 mg/mL with or without 50 µg/mL DCN, were buffered with 1X Dulbecco's modified eagle medium (DMEM) and mixed on ice. Gels were formed at 37 °C unless otherwise stated.

For turbidity measurements, which assess collagen fibrillogenesis kinetics, 100 µL of ice cold collagen solution was pipetted into a 96-well plate (n=5-6/group). Absorbance readings at 405 nm were made every minute for 60 minutes at room temperature [228]. Acellular gels were imaged using second harmonic generation (SHG) for qualitative comparison of collagen fibrils using a Zeiss LSM 710 confocal microscope (800 nm excitation).

To evaluate gel mechanical properties, acellular gels were tested in unconfined compression using a Bose ELF 3100 system with a 25 g load cell (Bose, Framingham, MA; Transducer Techniques, Temecula, CA). Gels were formed in a custom mold (8 mm diameter x 5.7 mm height) and incubated in PBS at 37 °C overnight prior to testing; gels were submerged in PBS in an acrylic chamber during testing at room temperature. Gels were preconditioned with 10 cycles of a triangle waveform varying from 0 to 10% strain at 0.05 Hz; testing was then performed using a monotonic ramp to 30% strain at 0.02 mm/s.

Gels were held at 30% strain for 150 s to allow stress relaxation. Peak stress was determined by averaging the stress during the last one second of the strain ramp. The equilibrium modulus was calculated after stress relaxation by averaging the last ten seconds of the 150 s hold time at 30% strain. The linear modulus was defined as the slope of a linear regression fit to the linear region (10%-30%) of the applied strain ramp; all linear fits had a correlation coefficient ≥ 0.9.

5.2.3 Microvascular Fragment Culture and Analysis

MVF were isolated as previously described [110]. Briefly, adipose tissue was harvested from epididymal fat pads of Lewis rats, minced, and partially digested with a collagenase solution. Selective filtration was then used to remove tissue larger than 500 μm and single cells smaller than 20 μm. MVF were suspended at 20,000 fragments/mL of gel and cultured in rhVEGF-supplemented serum-free media [112].

Quantification of vessel growth was done on day 9 of culture. MVF-containing gels were fixed with 4% paraformaldehyde, and rhodamine labeled Griffonia simplicifolia (GS-1) lectin (Vector Laboratories, Burlingame, CA) was used to stain vessel structures for quantification. GS1-lectin-stained MVF networks were imaged using a Zeiss LSM 700 confocal microscope. Five randomly selected fields were imaged at 10x to a depth of 402 μm for each gel, and 7-8 gels were imaged per group. Maximum intensity z-projections were created for each stack, thresholded, and skeletonized in ImageJ to determine branch number and total length. Gel contraction was determined by quantification of gel area

(ImageJ) from photographs (Gel Doc XR, Bio-Rad, Hercules, CA) of well plates over time in culture.

5.2.4 Statistics

All experiments were performed with n≥5, and results are presented as mean ± SEM. All analyses were performed as a two-way ANOVA with α level of 0.05 and Bonferonni post hoc tests. GraphPad Prism 5 was used for all statistical analyses.

5.3 Results

5.3.1 Collagen Fibillogenesis

The addition of DCN to both 3% and 6% collagen solutions led to a lower ultimate turbidity ($p<0.001$ for 3%, $p<0.01$ for 6%). DCN did not affect the lag time, the initial phase of fibrillogenesis during which nucleation sites form and turbidity is low, in 3% collagen. However, in 6% collagen, DCN shortened the lag time ($p<0.05$), allowing for an earlier onset of fibrillogenesis. The rate of fibrillogenesis as evidenced by the slope of the turbidity curve growth phase was not significantly affected by DCN in either group (Figure 5.1). There were overall effects of collagen percentage on both ultimate turbidity ($p<0.0001$) and rate of fibrillogenesis ($p<0.0001$), with higher collagen density increasing both parameters.

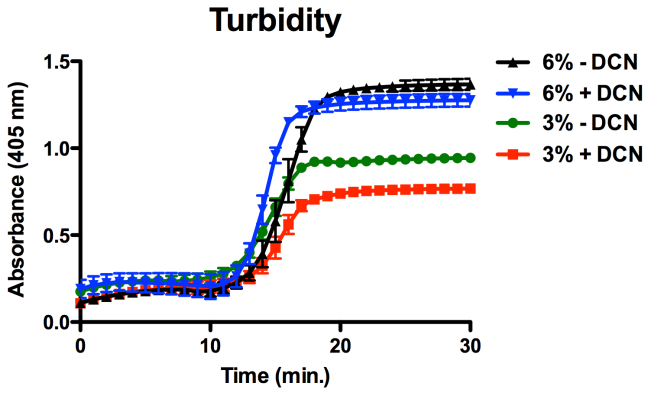

Figure 5.1. Collagen Density and DCN affect Collagen Fibrillogenesis. Turbidity curves for 3% and 6% collagen ± 50 µg/mL DCN (n = 5–6/group).

Qualitatively, in both 3% and 6% gels, the addition of DCN during polymerization of the collagen gels appeared to cause a more spatially uniform but diffuse organization of collagen fibrils with fewer short, wide bundles. Both 6% gels appeared denser than either 3% gel (Figure 5.2).

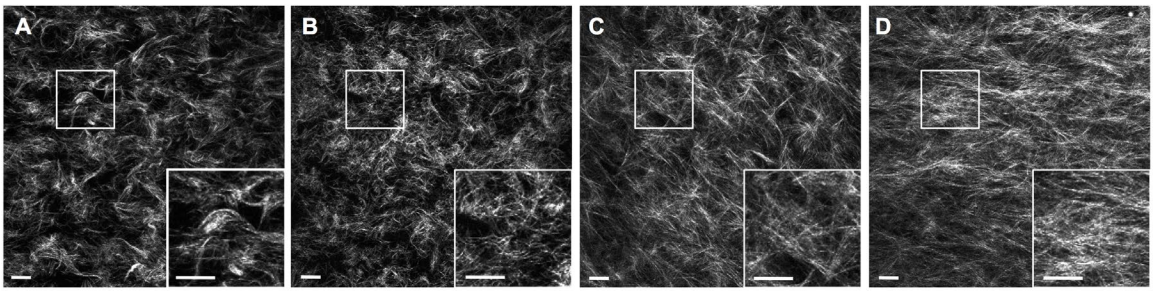

Figure 5.2. Collagen Fibril Structure ± DCN. Representative single-plane 60× SHG images of (a) 3% collagen without DCN, (b) 3% + DCN, (c) 6% − DCN, and (d) 6% + DCN with zoomed insets. Scale bars represent 30 µm.

5.3.2 Compressive Properties of Collagen Hydrogels

Both collagen density ($p<0.0001$) and DCN ($p<0.0001$) increased the peak stress experienced at 30% strain. There was also a significant, ordinal interaction effect ($p=0.0004$); the effect of DCN was greater in 6% than in 3% collagen (Fig. 3A). The equilibrium modulus was significantly higher in 6% vs. 3% collagen ($p<0.001$) but was not affected by DCN ($p=0.125$) (Fig. 3B). The linear modulus was also increased by increasing collagen density ($p<0.0001$), and DCN increased the linear modulus of 6% gels ($p<0.01$). The linear modulus of 3% gels was not affected by DCN, and there was no significant interaction (Figure 5.3).

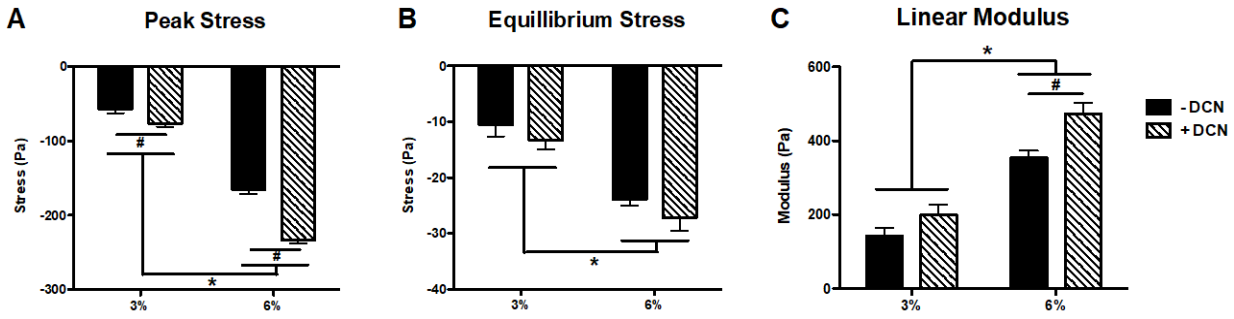

Figure 5.3. Compressive Properties of Collagen Gels ± DCN. Gel compression testing results showing (a) peak stress experienced at 30% load, (b) equilibrium stress level under maintained 30% strain, and (c) linear modulus (n = 5/group). *Indicates significant differences between 3% and 6% gels (2-way ANOVA, $P < 0.0001$). # Indicates significant differences between ±DCN ($P < 0.01$ for 6%; $P < 0.05$ for 3%).

5.3.3 Microvascular Growth

MVF cultured in 3% collagen gel resulted in significantly greater total network length ($p<0.0001$) and number of branches ($p<0.0001$) than those cultured in 6% gel. There was no significant effect of DCN on MVF growth, and there was no significant interaction.

Qualitative observations of the cultures showed that the 3% gels had more multidirectional branch-points (arrows, Figure 5.4 A-D) while 6% gels promoted bidirectional growth from the two fragment ends.

5.3.4 Gel Contraction

At day 16 of MVF culture, 3% collagen gels with no decorin had contracted to an average of 48% of their original (day 1) area, while 3% collagen gels with decorin and both 6% gels retained about 95% of their initial area. Both increased collagen density ($p<0.0001$) and DCN ($p<0.0001$) significantly attenuated gel contraction. A significant interaction effect was also revealed ($p<0.0001$), and post hoc tests showed that contraction of only 3% collagen gel was significantly reduced by the presence of DCN ($p<0.001$; Figure 5.5).

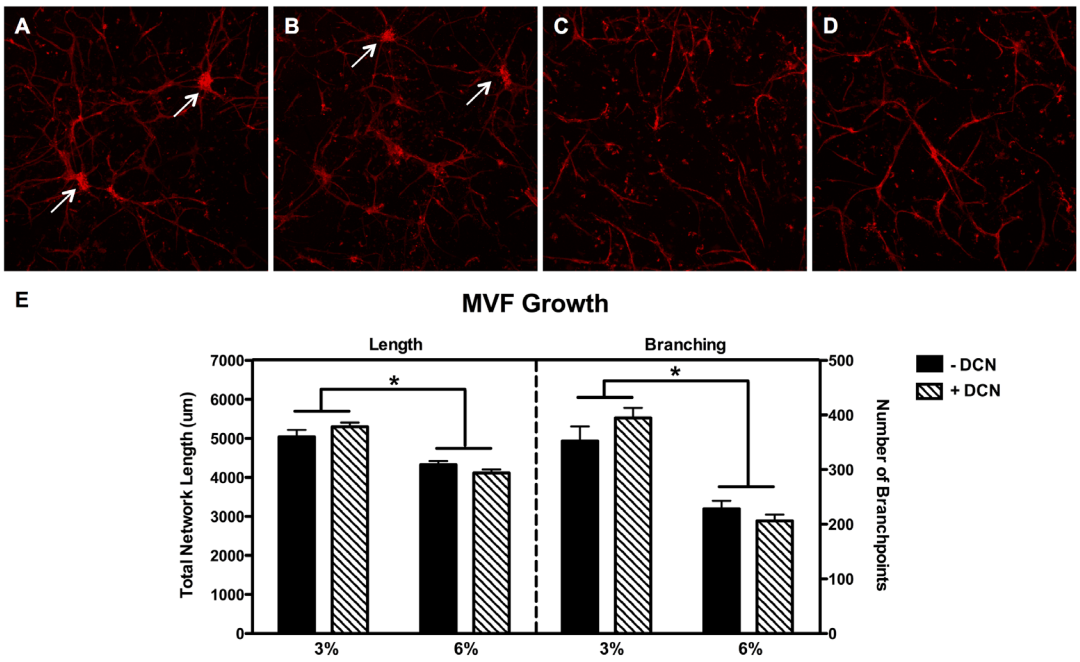

Figure 5.4. MVF Growth ± DCN. Representative 10x maximum intensity z-projections of MVF growth at day 9 in (a) 3% collagen without DCN, (b) 3% + DCN, (c) 6% − DCN, and (d) 6% + DCN and quantification (n = 5 frames/7–8 gels/group) of (e) total network length number of branch-points. * Indicates significant differences between 3% and 6% gels (2-way ANOVA, P < 0.0001). Arrows indicate multi-directional branch-point structures.

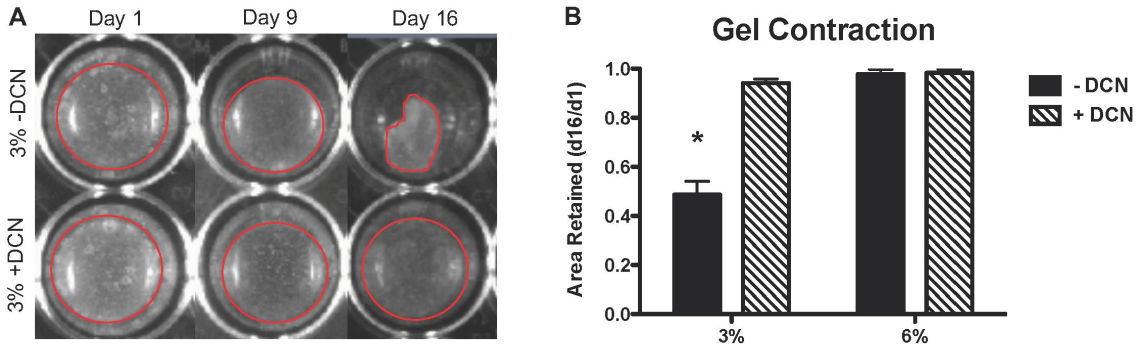

Figure 5.5. Gel Contraction ± DCN. Red outlines show border of gels within 48-well plate. B) Average fractional area retained by MVF-seeded gels over 16 days in culture (n = 6/group). * Indicates significant difference from all other groups (2-way ANOVA, P < 0.001).

5.4 Discussion

The vasculature is an integral component of musculoskeletal regeneration, both providing nutrient transport and participating in VEGF-BMP-2 signaling interplay [97, 98]. Changes in the mechanical environment of bone injury repair tissue have been associated with vascular changes in vivo [136]. However, it has been challenging to directly examine the relationship between the compressive loads of a large bone defect and vascular regulation. Accordingly, the goal of this work was to investigate the ability of DCN-supplemented collagen scaffold to maintain dimensional stability while supporting microvascular growth in vitro. The addition of DCN markedly increased the stability of 3% collagen gel through day 16 in culture. Further, although DCN increased the compressive properties of both 3% and 6% collagen gels, DCN-supplemented constructs supported robust MVF growth.

The addition of DCN significantly reduced contraction of 3% collagen. Although 6% collagen was not impacted by the addition of DCN, the 6% gels do not undergo appreciable contraction during culture, and thus it is logical that their mechanical properties were less affected by DCN. The reduction in contraction of the 3% gel by DCN was dramatic despite a relatively modest increase in compressive properties, potentially suggesting a biological effect of DCN rather than a purely mechanical phenomenon. Endothelial cells cultured on a DCN substrate have shown reduced focal adhesion formation [230], and DCN has shown reduced collagen contraction by fibroblasts through transforming growth factor ß (TGF-ß) inhibition [231, 232]. In contrast, DCN has also been shown to increase cell-mediated collagen contraction [233]; however, that study utilized highly contractile smooth muscle cells, and they may respond differently to DCN than

other vascular cell populations. Despite potential biological effects of DCN, MVF growth was not significantly different as a result of DCN supplementation.

Collagen is known to have a higher tensile than compressive modulus [227, 234]. Since DCN affects collagen properties via affecting fibrillogenesis, the tensile properties of resultant fibers may better show the effect of DCN. Thus, while a primary objective of this work was to establish whether collagen with DCN could withstand compression, the tensile properties of the gels may have been affected to a greater degree than the compressive properties. Additionally, forces exerted by cells during sprouting angiogenesis that ultimately cause the gels to contract are primarily tensile rather than compressive, perhaps suggesting that gel contraction was mitigated by an increased tensile modulus [185].

While increased substrate stiffness tends to decrease microvascular growth [113], using DCN to increase the modulus of the vascularized collagen gels did not have this effect. DCN is known to play a complex role in angiogenesis, with studies suggesting both pro- and anti-angiogenic effects depending on the context [230, 235-237]. Many of these studies focus on the expression of DCN by endothelial cells rather than on its function as an ECM component [237]; however, when endothelial cells were cultured on a two-dimensional DCN substrate, tube-like structure formation was inhibited, suggesting an anti-angiogenic role [230]. While tube-like structure formation is a critical step in *de novo* angiogenesis, DCN may not affect the subsequent steps such as sprouting and elongation that are more relevant to the microvascular fragment model presented in this study. Also, the use of pure DCN in isolation from other ECM moieties may have magnified effects of DCN. DCN is also known to interact with growth factors such as TGF-ß and has been

shown to upregulate vascular endothelial growth factor (VEGF) [238, 239]. In the system presented here, DCN may bind, sequester, and better present growth factors [240], thereby potentially promoting angiogenesis and effectively balancing the inhibitory effect of increased substrate stiffness.

Finally, the 50 μg/mL DCN dose used in this study was chosen based on previous research utilizing DCN in 2% collagen; while higher concentrations of DCN further affected fibrillogenesis, the tensile modulus plateaued at 50 μg/mL [228]. In this study, we used 3% collagen to compare microvascular growth to results from previous studies using this in vitro model for angiogenesis [107, 110-112], and it is possible that a higher dose of DCN would produce a greater effect in higher percentage collagen. As the concentration of collagen monomer is increased, collagen-collagen interactions may dominate over any effects between collagen and DCN and effectively dampen the response to DCN. Both 3% and 6% collagen showed a reduction of final turbidity in the presence of DCN, consistent with previous results in 2% collagen. However, the rate of fibrillogenesis, evidenced by the slope of the growth phase, was not affected by DCN in either 3% of 6% collagen, and the lag time was not affected in 3% collagen and was in fact reduced in 6% collagen (Fig. 1), contrasting previous results [228]. Taken together, these data suggest that the 50 μg/mL dose of DCN does have differing effects on different densities of collagen. Despite the variances in turbidity curves, SHG images of the gels qualitatively showed collagen organization differences, which were also noted in 2% collagen [228], and the compressive modulus was increased for both densities.

5.5 Conclusions

By quantifying collagen hydrogel construct mechanical properties and vascular growth as a function of collagen density and presence of DCN, this study has demonstrated a method to improve dimensional stability of collagen gels without compromising vascular growth. While it is unclear whether the reduction of gel contraction is primarily due to biological or mechanical effects of DCN, both compressive modulus and fibril structures were altered. Taken together, these data suggest that decorin-supplemented collagen constructs are an attractive candidate for in vitro model studies on the effects of compressive mechanical loading on three-dimensional microvascular growth.

CHAPTER 6. DECORIN-SUPPLEMENTED COLLAGEN HYDROGELS FOR THE CO-DELIVERY OF BONE MORPHOGENETIC PROTEIN-2 AND MICROVASCULAR FRAGMENTS TO A COMPOSITE BONE-MUSCLE INJURY MODEL [4]

6.1 Introduction

Traumatic musculoskeletal injuries resulting in open fractures, which are characterized by concomitant soft tissue injury, represent a major clinical challenge. Cases of open fracture have a two-fold increased rate of complications including infection, delayed union, malunion, and non-union compared to closed fractures [35]. These complications often lead to repeated surgical interventions that are still not able to avert long-term disability 7 years following injury [51]. One of the key clinical indicators of composite injury severity is vascular integrity; composite injuries that include vascular damage are considered the most severe [38]. We have previously established a pre-clinical rat model of composite bone-muscle extremity injury that recapitulates the attenuation of bone healing seen clinically [42], and similar pre-clinical models have also observed

[4] Adapted from Ruehle, M.A., et al., Decorin-Supplemented Collagen Hydrogels for the Co-Delivery of Bone Morphogenetic Protein-2 and Microvascular Fragments to a Composite Bone-Muscle Injury Model with Impaired Vascularization. Acta Biomaterialia, 2019. Doi: 10.1016/j.actbio.2019.01.045.

impaired bone healing with concomitant muscle injury [40, 41]. Previous studies in our composity injury model also demonstrated a dysregulated vascularization response following injury [43].

Early revascularization is a critical step of the wound healing cascade, providing a transport mechanism for oxygen, pro-regenerative growth factors, and stem and progenitor cells [10]. When vascularization is impaired in fracture models, bone healing is also severely impaired [15, 16]. Osteoprogenitor cells migrate into the bone defect region along with nascent vasculature, and osteoprogenitor cells and endothelial cells participate in bidirectional chemical signaling to stimulate growth [17]. As such, vascularization has been a promising target in bone regeneration, and many previous strategies have been employed including the co-delivery of osteogenic and angiogenic growth factors (e.g. bone morphogenetic protein-2 (BMP-2) vascular endothelial growth factor (VEGF)) as well as mesenchymal stem cell (MSC) and endothelial cell delivery [241]. However, while some growth factor co-delivery strategies report an improvement in healing [91-93], others report only a temporary transient effect or no effect at all [94-96, 99]. Although endothelial cell-based strategies have been shown to increase bone regeneration [101, 104], the resultant vasculature is often immature and leaky [105]. Another promising option is the use of microvascular fragments (MVF), which are multicellular segments of mature vasculature [107]. MVF are able to serve as a template for vascular growth and thus accelerate the establishment of vascular networks. Additionally, MVF retain vascular support cells and may therefore accelerate vessel maturation and patency. MVF form networks in vitro and have been previously shown to anastomose with host vasculature [195, 207] and increase tissue vascular volume [116] following implantation. Previous

vascularization therapies without an osteoinductive factor have not improved bone healing [96, 100]. Therefore, we investigated the co-delivery of MVF with BMP-2, a potent osteoinductive growth factor.

Design criteria for a co-delivery biomaterial are the support of MVF growth and sustained BMP-2 release. MVF have typically been cultured in type I collagen gels, which support in vitro sprouting and network formation [107, 116]. However, collagen-based materials tend to have a burst release of BMP-2 [242], which necessitates supraphysiological dosing and can cause exuberant bone formation outside the defect site [194]. Biomaterials with a more sustained BMP-2 release profile, such as alginate, have shown improved healing compared to collagen sponge [74]. MVF are sensitive to their extracellular matrix [110, 112], and we have previously developed a decorin-supplemented collagen culture substrate that supports robust angiogenesis of MVF [219]. Decorin (DCN) is a small leucine-rich proteoglycan naturally found in connective tissue [243]. DCN alters collagen fibrillogenesis, which in turn affects the mechanical properties of collagen hydrogels [219, 228] and limits the cell-mediated contraction of collagen [219].This increased dimensional stability allows vessel networks to grow and exert traction forces without collapsing the collagen matrix. DCN has also been shown to sequester transforming growth factor ß (TGF-ß) family growth factors [239, 240], such as BMP-2, which may allow for a more sustained release as compared to collagen alone.

Here, we evaluated decorin-supplemented collagen hydrogels (collagen+DCN) as a biomaterial vehicle for the co-delivery of BMP-2 and MVF. We hypothesized that collagen+DCN would increase BMP-2 retention over collagen alone due to DCN's ability

to sequester TGF-ß growth factors. We further hypothesized that MVF would increase both early vascularization and subsequent BMP-2-mediated bone regeneration.

6.2 Methods

All animal experiments were performed in accordance with protocols approved by the Georgia Institute of Technology Institutional Animal Care and Use Committee (IACUC).

6.2.1 In vitro Construct Preparation & Characterization

MVF growth and the acellular BMP-2 release kinetics of collagen+DCN hydrogels were assessed and compared to collagen alone and to alginate. Collagen gels were made at 3% w/v and buffered with Dulbecco's modified eagle medium (DMEM; ThermoFisher Scientific; Waltham, MA). Collagen+DCN gels consisted of 3% collagen supplemented with 50 µg/mL DCN as previously described [219]. To prepare alginate hydrogels, RGD-functionalized alginate (FMC BioPolymer; Ewing, NJ) dissolved in αMEM was crosslinked with calcium sulfate for a final concentration of 2% [75].

MVF were isolated as previously described [107]. Briefly, epididymal fat pads were harvested from Lewis rats, minced, and digested with a collagenase solution for 7 minutes at 37 °C. MVF were obtained through selective filtration to retain tissue between 20-200 µm. Tissue was first passed through a 200 µm filter to remove partially undigested adipose tissue; the flow-through was then passed through a 20 µm filter to remove single cells. MVF were suspended at a density of 80,000 fragments/mL in solution prior to gelation.

To assess BMP-2 release kinetics, acellular gels were loaded with 500 ng BMP-2 (n=4/group) by incorporation within solution prior to gelation. Gels were incubated at 37 °C in αMEM (ThermoFisher) supplemented with 10% fetal bovine serum (Atlanta Biologics; Atlanta, GA). Media was collected and replaced at time points up to day 20. BMP-2 present in the collected media was quantified by ELISA according to manufacturer's instructions (R&D Systems, Minneapolis, MN). BMP-2 release was then compared for acellular vs. MVF-containing collagen+DCN hydrogels as above up to day 7 (n=5/group).

MVF growth in collagen+DCN gels ± BMP-2 was assessed at day 7 (n=5/group). MVF-containing constructs were cultured in αMEM (ThermoFisher) supplemented with 10% fetal bovine serum (Atlanta Biologics) and 1% penicillin-streptomycin-glutamine (ThermoFisher). In the BMP-2 containing group, 500 ng BMP-2 was incorporated into the collagen+DCN solution prior to gelation. Gels were fixed with 4% paraformaldehyde and stained with rhodamine-labeled Griffonia simplicifolia (GS-1) lectin (Vector Laboratories, Burlingame, CA). Five randomly selected fields were imaged per gel to a depth of 402 μm using a Zeiss LSM 700 confocal microscope. Maximum intensity z-projections were created for each stack, thresholded, and skeletonized using the AngioAnalyzer ImageJ plugin to determine branch number and total length [116, 219].

6.2.2 Surgical Procedures

Composite defects were made in 13-week-old female Lewis rats for syngeneic implantation of MVF harvested from Lewis rats. Lewis rats that ubiquitously express GFP

(LEW-Tf(CAG-EGFP)YsRrrc) were obtained from the Rat Resource and Research Center (RRRC, Columbia, MO) to enable the detection of implanted MVF. Bone defects received either collagen+DCN loaded with 2.5 μg BMP-2 and MVF (BMP-2+MVF), collagen+DCN loaded with BMP-2 (BMP-2), or an empty collagen+DCN gel (gel only). Gels were formed in custom polycarbonate molds to achieve a diameter of 5 mm and a length of 1 cm and placed inside perforated PCL mesh tubes for implantation. 36 animals were used to evaluate the effect of MVF on BMP-2-mediated revascularization and subsequent bone healing. A subset of animals (n=6/BMP-containing group) were euthanized at 7 days post-surgery to assess vascularization using μCT angiography. The remaining animals (n=9/BMP-containing group, n=6/gel only group) were euthanized at 12 weeks post-surgery to assess bone regeneration.

6.2.3 μCT Angiography

Animals were sequentially perfused with 0.9% saline to clear blood vessels, 0.4% papaverine hydrochloride to dilate vessels, 10% neutral buffered formalin to fix, saline to rinse, and a lead chromate radiopaque contrast agent (Microfil MV-22 diluted 2:1; Flow Tech, Inc., Carver, MA). Samples were stored overnight at 4 °C to allow complete polymerization of the contrast agent prior to dissection and μCT analysis. Hind limbs from the hip to the knee were excised. No bone had yet formed in the defect area by day 7, so limbs were analyzed immediately.

Two volumes of interest (VOIs) were used to analyze either the bone defect region only or the entire thigh, including both the bone defect and surrounding muscle. All scans

were performed at a 21 μm voxel size. The thigh VOI encompassed the entire diameter of the thigh for the length of the defect, and the bone defect VOI consisted of a cylindrical volume 6 mm in diameter to encompass the outer diameter of the treatment-containing PCL mesh tube. A global threshold was applied for segmentation of vasculature, and a Gaussian low-pass filter was used to suppress noise ($\sigma = 0.8$, support = 1). Total vascular volume and voxel diameter histograms were computed using native Scanco software. The number of voxel counts per diameter bin was used as a measure of vessel number [116].

6.2.4 Bone Regeneration Analysis

Bone tissue regeneration was assessed by radiography at 2, 4, 8, and 12 weeks post-surgery and by μCT at 4, 8, and 12 weeks post-surgery. For quantitative μCT analysis, the defect region was scanned with a voxel size of 38 μm. The middle 6.5 mm of the defect was analyzed, and bone volume was quantified by Scanco software using a threshold corresponding to 50% of intact cortical bone [193]. Functional regeneration was assessed by mechanical testing at 12 weeks endpoint. Thighs were harvested, soft tissue was cleared, and fixation plates were removed. Femur ends were potted in Wood's metal (Alfa Aesar) and tested in torsion at a rate of 3°/s to failure or to 30° of rotation (ELF 3200, TA ElectroForce) [61]. The failure strength (torque at failure) and stiffness (linear region of torque vs. rotation plot) were calculated for all samples.

6.2.5 Histology and Immunohistochemistry

Bone tissue was decalcified, sectioned at a 5 μm thickness, and stained with hematoxylin and eosin (H&E; Histotox Labs; Boulder, CO). Immunohistochemistry was also performed on bone tissue sections to evaluate the presence of implanted GFP-expressing MVF. Deparaffinized sections were blocked, incubated with anti-GFP antibody (ab290, Abcam; Cambridge, UK) at a dilution of 1:100, washed, incubated with secondary antibody (A-11036, ThermoFisher) at a dilution of 1:50, washed, and counterstained with DAPI (ThermoFisher) at a dilution of 1:1000.

6.2.6 Statistical Analysis

Data were analyzed using GraphPad Prism 5, and all statistical tests were conducted with $\alpha=0.05$. BMP-2 release data were analyzed with a repeated measures one-way ANOVA with Bonferroni's multiple comparisons test. MVF network length and branching with and without BMP-2 were compared with a Student's t-test with Welch's correction for unequal variances. Total vascular volume data were analyzed with a one-way ANOVA (thigh) with Bonferroni's multiple comparisons test or with a Student's t-test (bone defect area). Vessel thickness histograms were compared using a two-way ANOVA [116] with Bonferroni's multiple comparisons test. Longitudinal bone healing and mechanical testing had significantly different variances among treatment groups (Bartlett's test, $p<0.05$) and were therefore analyzed with Kruskal-Wallis tests and Dunn's multiple comparisons test. Data are plotted as mean with standard error of the mean (SEM) or as a box plot with whiskers indicating the minimum and the maximum.

6.3 Results

6.3.1 In vitro Biomaterial Characterization

Acellular hydrogels were then tested for BMP-2 release. Collagen+DCN released significantly less BMP-2 over days 1-5 than either collagen alone or alginate. By day 10, collagen+DCN released less BMP-2 than collagen alone but was not statistically different than alginate. At days 15-20, the quantity of BMP-2 released by all three materials was significantly different (Figure 6.1 A; RM-ANOVA, $p<0.05$). At day 20, collagen had released about 35% of the loaded BMP-2, collagen+DCN had released about 28%, and alginate had released about 25%.

Release of BMP-2 from acellular vs. MVF-containing collagen+DCN gels was compared up to day 7. Beginning at day 3, the MVF-containing gels released significantly more BMP-2 than acellular gels (Figure 6.1 B; RM-ANOVA, $p<0.05$). This difference persisted through day 7 ($p<0.01$). At day 7, MVF-containing gels had released 12.9% of the loaded BMP-2, and acellular gels had released 11.6%. BMP-2 significantly increased total MVF network length and branching (Figure 6.1 C) and qualitatively appeared to accelerate MVF network formation (Figure 6.1 D-E).

6.3.2 Effect of MVF on Early Revascularization Following Composite Injury

Composite defects were treated with either collagen+DCN gels loaded with BMP-2 and MVF, collagen+DCN gels loaded with BMP-2 alone, or empty collagen+DCN gels only. Based on the reduced number of small diameter vessels within both the thigh and

bone defect region at day 7 of the early revascularization study, 6 animals per BMP-containing treatment group were euthanized 7 days post-surgery for µCT angiography.

Both treatment groups had significantly greater thigh vascular volume than the contralateral leg (Figure 6.2 A-B; $p<0.0001$). However, the total vascular volume was not significantly different between BMP and BMP+MVF in the thigh region or the bone defect region. Analysis of vessel size distributions revealed that compared to BMP alone, BMP+MVF treated defects had significantly fewer vessels in the bone defect regions (Figure 6.2 C; 2-way ANOVA, overall effect $p<0.01$, n.s. interaction effect). The thigh region possessed fewer small diameter vessels, ranging 0-200 µm and 600-1000 µm in the BMP+MVF animals compared to the BMP animals (overall effect $p<0.0001$, interaction effect $p<0.01$).

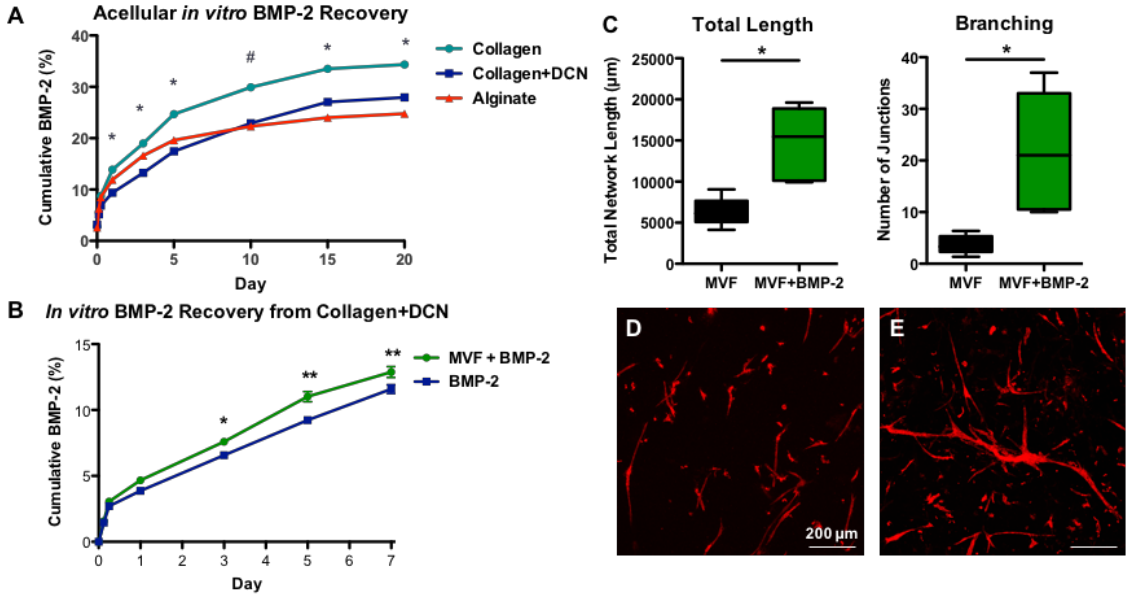

Figure 6.1. In vitro characterization of BMP-2 release and effect on MVF growth. A) Cumulative in vitro BMP-2 released by acellular gels into surrounding media. RM-ANOVA, * $p<0.05$ between all three materials, # $p<0.05$ between collagen and collagen+DCN and collagen and alginate; n=4/group. B) Cumulative in vitro BMP-2

released by acellular vs. MVF-containing collagen+DCN gels into surrounding media. RM-ANOVA, * $p<0.05$, ** $p<0.01$; n=5/group. C) Quantification of total MVF network length and branching without BMP-2 (D) and with 500 ng BMP-2 incorporated into the collagen+DCN gel (E) at day 7 of culture. Student's t-test, * $p<0.05$; n=5/group.

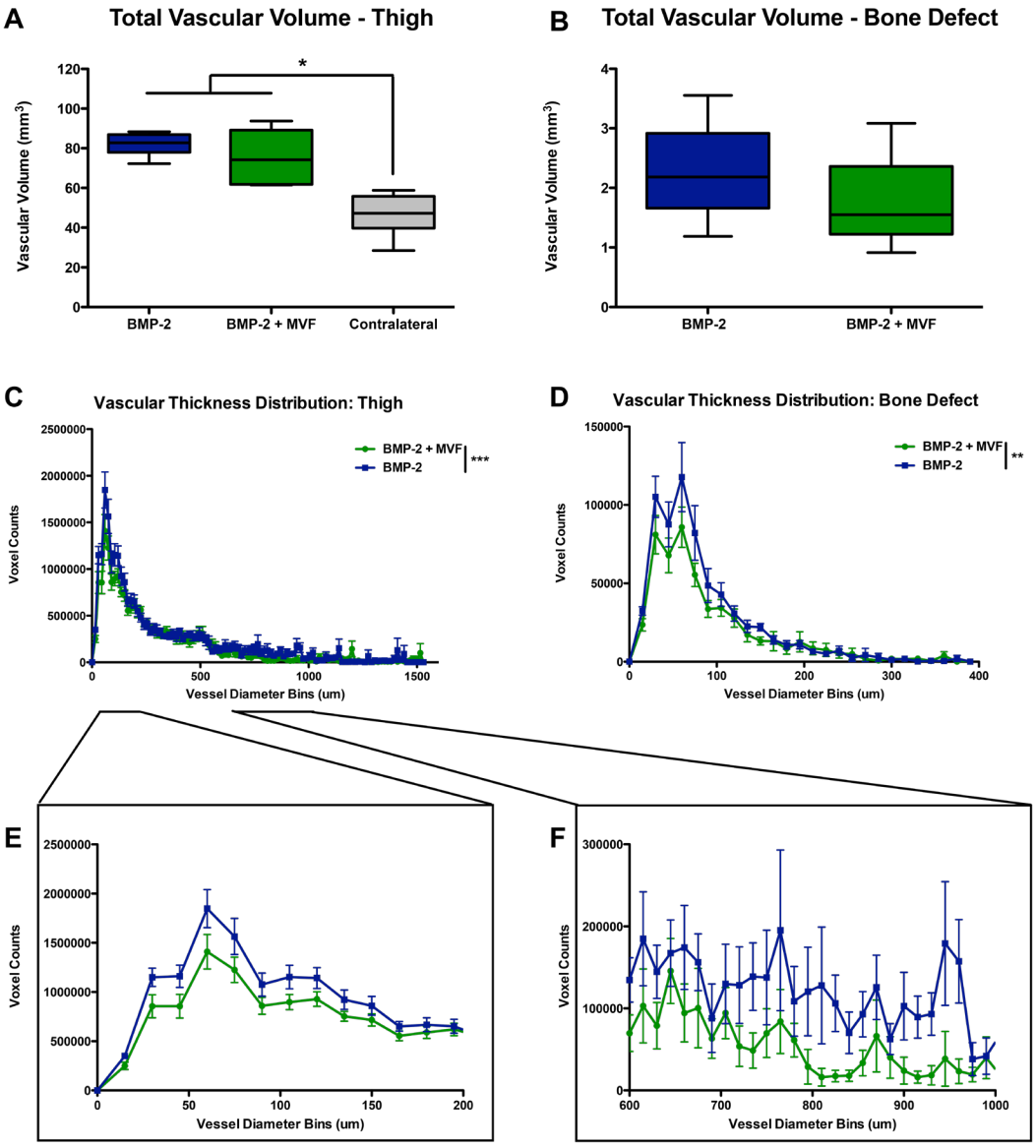

Figure 6.2 Effect of MVF delivered in collagen+DCN on early revascularization following composite injury. Quantitative μCT angiography results for total volume of A) the thigh region and B) the bone defect region. 2-way ANOVA, * $p<0.0001$ between BMP groups and contralateral control; n=6/group. Vascular thickness distributions for C) the thigh region and D) the bone defect region. Insets show E) small 0-200 μm diameter and

F) intermediate 600-1000 μm diameter voxel within the thigh. Voxel counts indicate the number of voxels with a given diameter and are utilized as a measure of vessel number.2-way ANOVA, ** $p<0.01$ between BMP+MVF and BMP (overall effect), *** $p<0.001$.

6.3.3 Effect of MVF on Bone Regeneration in Composite Injury

At 12 weeks, radiography demonstrated inconsistent bridging in both BMP-containing groups (with and without MVF; Figure 6.3). Semi-quantitative bridging scores 0-4 were assigned to each animal: 0, no mineralization; 1, sparse, isolated areas of mineral; 2, substantial but discontinuous mineralization; 3, near but incomplete bridging; 4, complete bridging [244]. Both BMP-containing groups had approximately one third of defects completely bridge (score 4), one third produce substantial mineralization without bridging (score 2-3), and one third with little to no mineral (score 0-1). The gel only control group did not induce substantial bone formation in any animal (all scored 0-1).

Bone volume as measured by μCT was significantly higher in both BMP-containing groups than the gel only control at 12 weeks (Kruskal-Wallis test, $p=0.011$; Figure 6.4 A); there was no effect of MVF on bone volume. There was no difference among treatment groups in failure strength or stiffness, and all groups were significantly below that of the intact contralateral control (Kruskal-Wallis test, $p<0.001$; Figure 6.4 B-C).

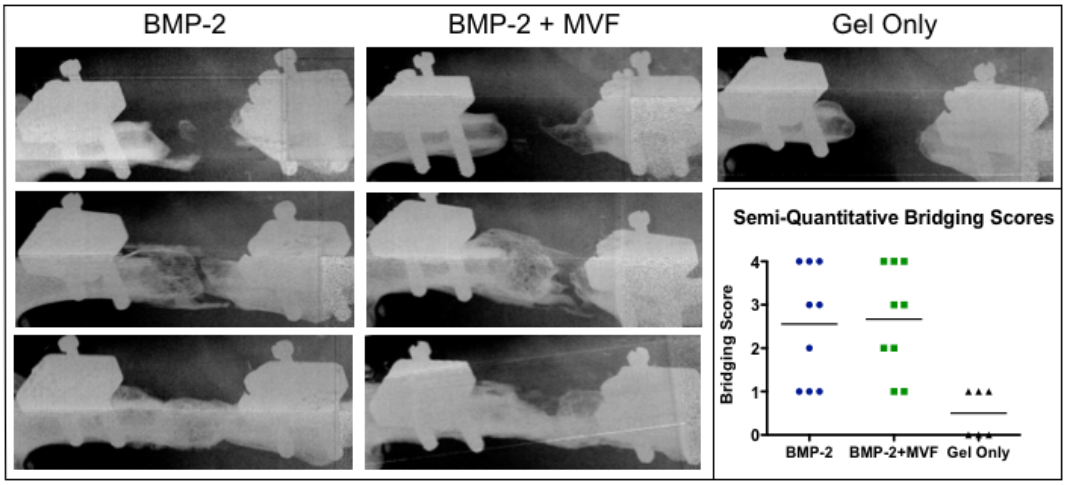

Figure 6.3 Representative radiographs of bone defects treated using collagen+DCN delivery vehicle. Representative 12 week radiographs of non-mineralized (top; bridging score 0-1), mineralized but not bridged (middle; bridging score 2-3), and completely bridged (bottom; bridging score 4) samples from each treatment group. The Gel Only group produced only non-mineralized samples. Inset chart shows the semi-quantitative bridging score distribution and mean for each group.

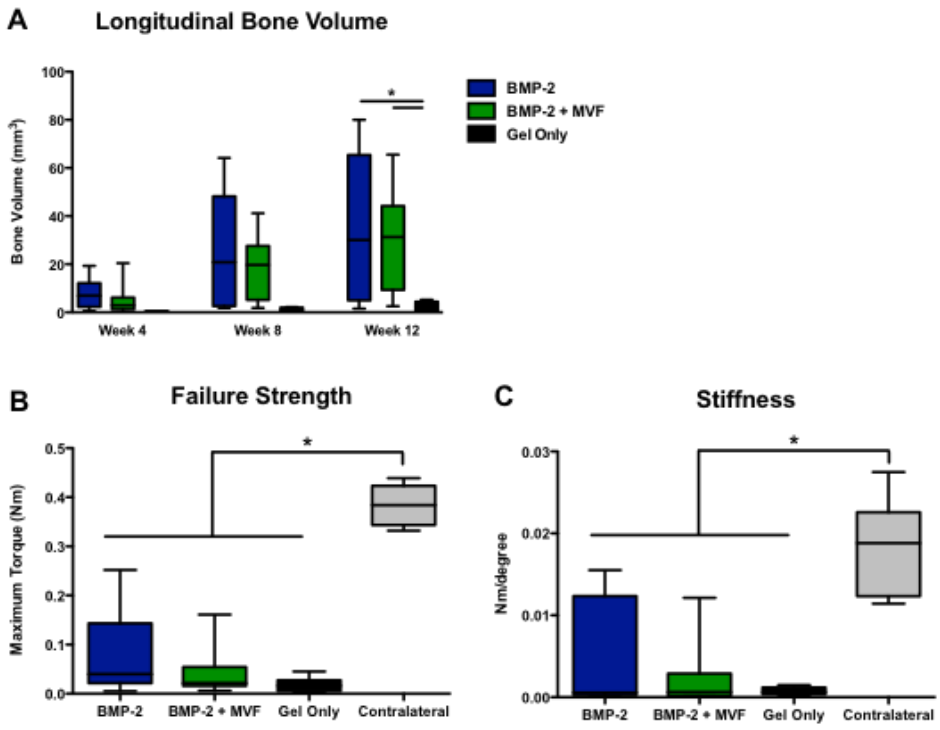

Figure 6.4. Properties of bone regenerated using collagen+DCN delivery vehicle. A) Longitudinal bone volume as measured with µCT. Kruskal-Wallis test, * p=0.011 between

both BMP groups and the Gel Only material control group. B) Failure strength and C) Stiffness of regenerated bone tissue at the 12 week endpoint. Kruskal-Wallis test, * $p<0.001$ between all treatment groups and the contralateral control.

6.3.4 Histology and Immunohistochemistry

H&E staining demonstrated that even in samples with moderate bone volume, the defect area often failed to bridge with one or both intact bone ends (Figure 6.5 A); this is in agreement with the radiography shown in Figure 6.3. Due to the high variability of bone volume, H&E was performed on three samples representing low, moderate, and high bone volume for each treatment group (the collagen+DCN gel only group only produced low bone volume, so only one sample was stained; Figure 6.5 B). The low bone volume samples displayed primarily fibrous tissue. The low bone volume samples from the BMP-containing groups appeared more loosely structured than the gel only group, which was very densely cellular. The moderate bone volume samples appeared to have islands of mineralized tissue within larger areas of marrow-like tissue. The high bone volume samples had fewer and smaller areas of marrow-like tissue. Although there were larger areas of mineralized tissue, they appear more disorganized than intact mature bone tissue.

Immunohistochemistry was performed to determine whether the implanted GFP-expressing MVF remained within the defect at either 1 week or 12 weeks post-surgery. At 1 week, GFP+ cells were identifiable in the defect region (Figure 6.6); however, rather than being evenly distributed throughout the defect, these GFP+ cells appeared to be clustered together. Additionally, they appeared as distinct, single cells rather than multicellular

vessel structures and are not associated with vascular structures. At week 12, no cells stained positive for GFP.

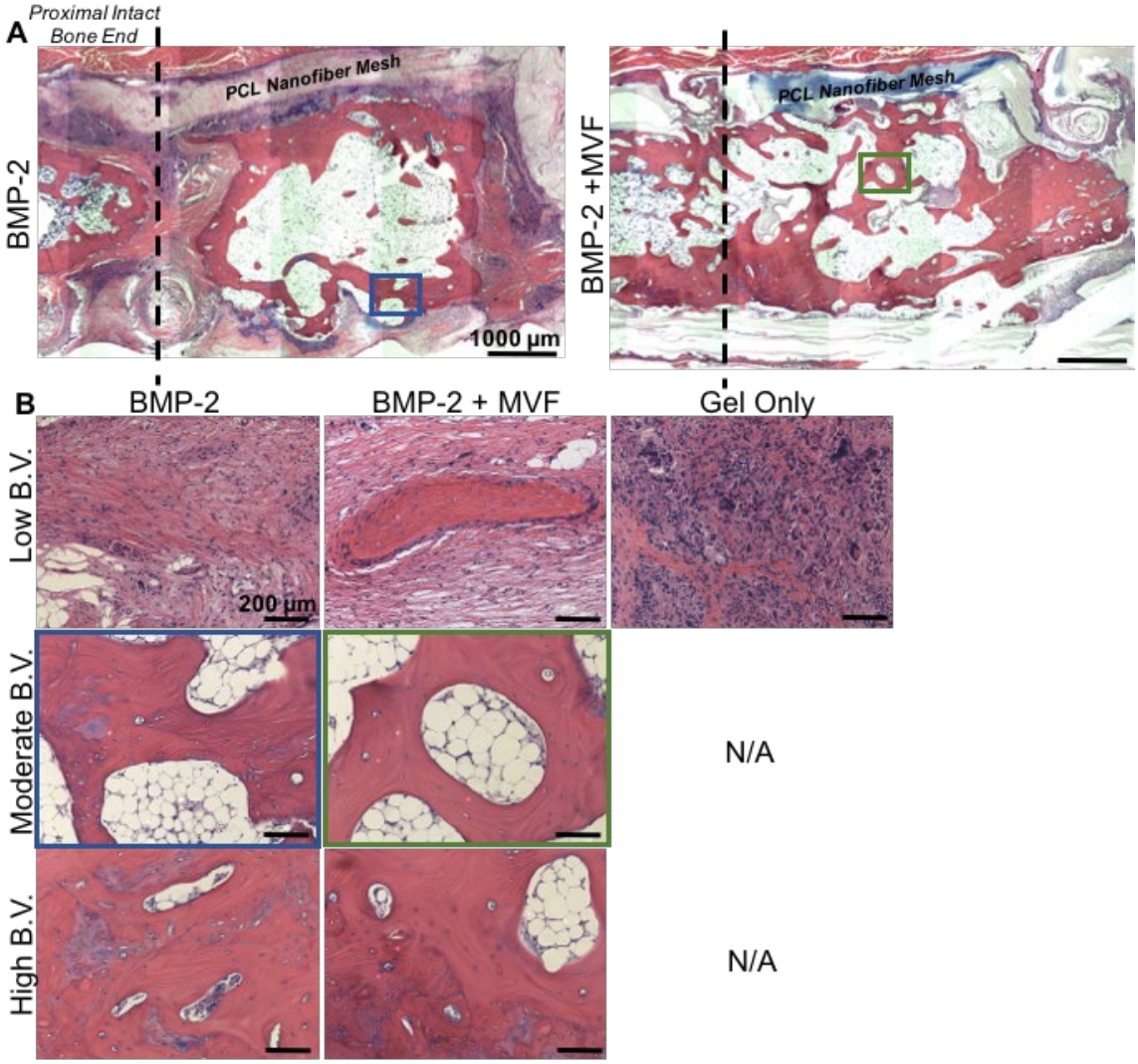

Figure 6.5. Hematoxylin & Eosin staining of bone regenerated using collagen+DCN delivery vehicle. A) Representative H&E mosaic images of samples from the BMP-2 (top) and BMP-2+MVF (bottom) treatment groups. The PCL nanofiber mesh denotes the boundaries of the defect area, and the proximal intact bone end is marked with dotted line. Scale bar = 1000 µm. B) Representative low (top), moderate (middle), and high (bottom) bone volume samples from each treatment group at the 12 week endpoint. The Gel Only group produced only low bone volume samples. Location of moderate bone volume samples within mosaics are outlined in blue and green for the BMP-2 and BMP-2 + MVF groups, respectively. Scale bar = 200 µm.

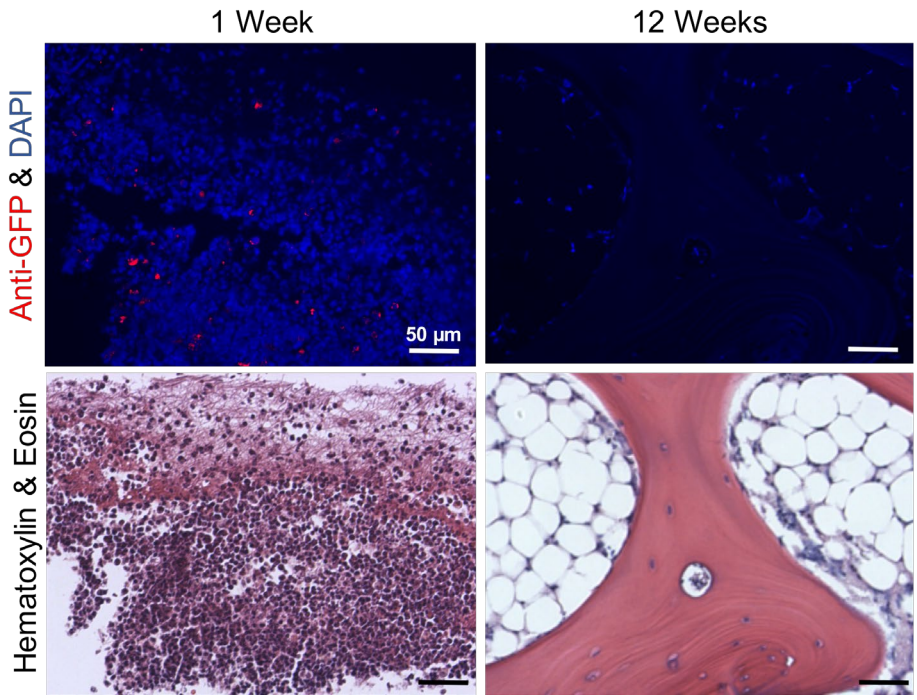

Figure 6.6. Immunohistochemistry to determine presence of implanted GFP+ MVF. Anti-GFP immunohistochemistry (top) to determine retention of implanted GFP+ MVF at 1 week and 12 weeks post-surgery. Red – anti-GFP antibody, blue – DAPI. Serial sections stained with H&E (bottom). Scale bar = 50 µm.

6.4 Discussion

A key indicator of traumatic composite injury severity is vascular integrity [38]. Clinically, bone injuries with concomitant muscle damage are more prone to complications and long-term disability, and those with vascular damage are the most susceptible [35, 51]. We have previously developed a rat model of composite injury that recapitulates the bone healing deficit seen clinically [42] and a vascular deficit [43].

In an effort to rescue this vascular deficit, collagen+DCN hydrogels were developed as a biomaterial delivery vehicle for both BMP-2 and MVF. This material has previous been shown to support vascular growth in vitro with minimal cell-mediated contraction of

the gel [219]. Similar vascularized constructs have been implanted and progressed to connect with the host vasculature [195], increase tissue vascular volume [116], and respond to local microenvironmental characteristics [207]. However, in this application, MVF were not able to overcome the vascular deficit and in fact were associated with decreased number of vessels relative to BMP alone at day 7. The timing of VEGF expression has been implicated as an important regulator of bone healing [94, 99], and delivering MVF immediately following injury may have disrupted the endogenous timeline of wound healing angiogenesis. Endogenous VEGF expression typically peaks around day 5-10 post-injury [99], while delivering MVF immediately following defect creation may have introduced larger amounts of VEGF much earlier. Early presence of VEGF may have then disrupted growth factor gradients and prevented the full endogenous angiogenic response. However, a majority of BMP-2 and VEGF co-delivery studies that ultimately did not show improved bone healing did observe increased vascularity [94-96, 99, 100]. A previous study examining the effect of hindlimb ischemia on segmental defect healing observed a beneficial effect of transient ischemia on revascularization and subsequent bone healing [245]; the complexity of the relationship between vascularization and bone regeneration is not yet fully understood. Although GFP+ cells were observed within the defect area at day 7, they appeared as single cells rather than the GFP+ multicellular vessel fragments that were implanted. While some loss of support cells is a normal element of sprouting angiogenesis, the GFP+ cells do not appear to be associated with vessel-like structures, suggesting instead that a majority of the cells comprising the MVF dissociated to a single cell level. As the implanted vessel fragments dissociated, vessel destabilization cues may possibly have been transmitted to the surrounding tissue, resulting in a decreased number

of vessels within the thigh compared to BMP alone. Previous studies delivering MVF that showed increased tissue vascular volume had pre-cultured the MVF in vitro prior to implantation, which allowed for provisional network formation [116]. While the freshly isolated MVF tested in this study potentially have greater translational applicability, the pre-culture of constructs accelerates inosculation [115] and may be critical to functional revascularization by implanted cells.

MVF also did not have a statistically significant effect on bone volume or mechanical properties. However, the mean and median bone volume, failure strength, and torsional stiffness were all lower in the BMP-2 + MVF group than in the BMP-2 alone group. This may primarily be due to their negative effect on the already dampened revascularization response in the composite defect model. GFP+ MVF-derived cells were not observed in the defect tissue at the 12 week end point, indicating that they did not integrate into the regenerated tissue. Cell-based therapies broadly are challenged by issues of retention and survival [106, 246]; although the implanted cells in this study were able to persist to day 7, without inosculating with the host vasculature, they may have failed to survive within the harsh, hypoxic injury environment. Additionally, exogenous cells may metabolize or degrade BMP-2, thereby reducing its effective dose and availability to osteoprogenitors [68]. However, the in vitro BMP-2 release experiment showed that MVF-containing collagen+DCN gels released modestly but significantly more detectable BMP-2 than acellular gels. This may be due to proteolytic activity of MVF as they sprout and invade the matrix. BMP-2 also significantly increased MVF network length and branching at day 7, which is in agreement with previous reports of BMP-2 increasing angiogenesis [247, 248]. Previous literature showed decreased mineralization when adipose-derived MSCs

were co-delivered with BMP-2, whereas bone marrow-derived MSCs increased BMP-2-mediated mineralization [67]. While adipose-derived MVF do contain MSCs, they represent only about 5% of the cellular constituents [119, 220]. Cell source more broadly may be an important consideration when using MVF therapeutically. Further, even in samples with moderate bone volume, the defect area often failed to bridge with one or both intact bone ends across both BMP-containing treatment groups. While we have established an association between altered revascularization and impaired bone healing, other factors may also contribute to reduced healing. There is evidence for crosstalk between growth factors secreted by muscle tissue and the periosteum [42], perhaps contributing for the relatively low bridging rates observed in this study. The loss of adjacent muscle tissue sustains the pro-inflammatory stage of wound healing [40], and immunomodulatory agents have been shown to improve bone healing in traumatic injuries with volumetric muscle loss [208]. Composite tissue injuries are complex and may require adjunct therapies to address multiple facets of the healing process.

The collagen+DCN delivery vehicle met the in vitro design criteria as a matrix supporting both MVF growth and sustained BMP-2 delivery. MVF grow robustly in collagen+DCN [219], and DCN increased the retention of BMP-2 in vitro compared to collagen alone. At an intermediate timepoint (day 10 of 20), the BMP-2 release of collagen+DCN was not statistically different than alginate. DCN preferentially binds TGF-ß family growth factors such as BMP-2 [239]. As such, DCN may have transiently bound BMP-2, increasing retention, and released it, allowing BMP-2-induced mineralization [240]. Interestingly, DCN has been shown to play a role in angiogenesis, with studies showing both positive and negative effects [230, 236, 237, 249, 250]. DCN deficient mice

exhibit deficiencies in angiogenesis [235], and sprouting endothelial cells express DCN [251]. As an extracellular matrix component, DCN has been shown to inhibit endothelial cell tube formation [230]. However, collagen+DCN is an effective in vitro culture substrate for MVF and facilitates network branching and extension [219]. Collagen+DCN supports angiogenesis in vivo as well. Vessels were able to migrate into the bone defect area, and the 7 day perfusion results appeared qualitatively similar to those observed at day 7 in the alginate system.

As a delivery vehicle for BMP-2, collagen+DCN gels are capable of bridging the challenging composite defect model, albeit inconsistently; mineralization occurred in approximately two-thirds of BMP-treated defects. A previous study of bone healing in the composite defect model observed very comparable bone volume and mechanical properties in composite defects using a well-established alginate delivery vehicle for a functionally equivalent dose of BMP-2 (2 vs. 2.5 μg) [42]. In the present study, the average 12 week bone volume of the BMP only group was 33.38 mm^3, and the average failure strength was 0.0779 Nm; Willett et al. observed a 12 week bone volume of 28.99 mm^3 and a failure strength of 0.0558 Nm in composite defects treated with BMP-2 delivered in alginate. Thus, the inconsistent bone healing observed here may speak more to the extraordinarily challenging nature of composite tissue injuries rather than the efficacy of collagen+DCN as a BMP-2 delivery vehicle. Although not able to promote consistent bridging in challenging composite tissue injuries, collagen+DCN performed as well as RGD-alginate as a vehicle for sustained delivery of BMP-2.

6.5 Conclusions

Composite injuries to bone and adjacent soft tissue are more prone to clinical complications and poor healing outcomes. Previous studies in an established rat bone-muscle injury model demonstrated a modest but significant impairment in early revascularization, which may contribute to impaired bone healing. In an attempt to overcome this vascular deficit, we developed and characterized collagen+DCN hydrogels as a co-delivery vehicle for a vascular therapeutic, MVF, and the osteoinductive growth factor, BMP-2. However, despite in vitro data suggesting synergistic effects between BMP-2 and MVF, we unexpectedly found that MVF did not increase vascular volume and in fact decreased the number of vessels both within the bone defect area and the surrounding tissues of the thigh. GFP+ cells from the implanted GFP+ MVF were present within the bone defect at 1 week post-surgery but appeared as single cells rather than as vessel structures, and no GFP+ cells were observed at 12 weeks post-surgery. Although MVF did not improve bone healing, the collagen+DCN biomaterial delivery of BMP-2 was able to achieve bridging in the challenging composite defect model, reaching endpoint bone volume and mechanical properties comparable to a well-established RGD-alginate delivery system. Decorin-supplemented collagen hydrogel is therefore a promising biomaterial delivery vehicle for treating composite extremity injuries, and future studies will explore pre-culturing MVF in vitro to allow stable network formation prior to implantation.

CHAPTER 7. MECHANICAL LOADING TEMPORALLY REGULATES MICROVASCULAR ANGIOGENESIS

7.1 Introduction

Vasculature is an abundant and vital component of nearly all tissues, and revascularization is a critical step of the wound healing cascade [10]. Angiogenesis, the primary mode of new vessel formation in wound healing, begins as new vessels sprout from adjacent intact blood vessels. New vessels invade the wounded area and begin to form microvascular networks within just a few days. Concurrent with the early steps of angiogenesis, a collagenous provisional matrix is formed, which appears characteristically granular due to its high density of newly formed capillaries. Granulation tissue is then remodeled into mature tissue through a complex series of chemical and physical cues [252] such as the coordinated expression of growth factors and cytokines [253] and dynamically changing ECM properties [130]. During this healing process, granulation tissue also experiences tissue-specific applied forces that are known to influence healing. For example, bone experiences functional compressive loading [209], ligaments and tendons undergo tension [254], venous ulcers are often treated with compression bandages [255], and even cutaneous wound experience tension during closure [256]. While the vasculature has long been recognized as mechanosensitive [222], remarkably little is known about the effects of abluminal forces experienced by healing tissues on angiogenesis.

Previous in vivo work from our lab has shown that abluminal forces, such as bulk compression of the extracellular matrix, can have potent effects on vascular growth – both

inhibitory and stimulatory. When functional loading was applied immediately following injury, angiogenesis and subsequent tissue healing were inhibited. However, when loading was delayed until initial matrix deposition had already occurred, blood vessel growth and subsequent tissue healing were enhanced [136], implicating abluminal loading in differential temporal regulation of angiogenesis.

Sprouting angiogenesis is a dynamic process involving multiple phases of concerted cellular activities. For organized, directed sprouting to occur rather than indiscriminate growth, a subset of endothelial cells within the vessel are selected as sprout tip cells, while adjacent endothelial cells are maintained as stalk cells through lateral inhibition. Tip cells extend filopodia into the surrounding matrix and lead the matrix invasion and migration of the nascent sprout [30]. Stalk cells follow the migrational pattern established by tip cells [257] and proliferate to drive the sustained elongation of nascent vessels [30]. Many of the processes involved in angiogenesis are responsive to mechanical stimuli. Tip cell selection depends on the balances of Notch1 and its ligands Jag1 and Dll4 [30], which have recently been identified as mechanosensitive [258, 259]. Invasion of the ECM by tip cells involves a balance of proteolysis and matrix deposition [30, 32, 33]; expression and secretion of proteases that are involved in angiogenesis such as Mmp2, Mmp9, and Mmp14 are also mechanosensitive [260, 261]. Collective cell migration of both leading tip cells and following stalk cells requires the binding and release of ECM by adhesion molecules such as integrins [31], which are important mediators of mechanotransduction between the ECM and cells [262]. Intracellular mechanotransduction, often activated by integrins, is required to elicit a cellular response. Recently, yes-associated protein (YAP) and its paralog transcriptional coactivator with

PDZ-binding motif (TAZ) have been identified in flow-mediated vascular mechanotransduction [263]. YAP and TAZ are also regulate a number of processes crucial to angiogenesis, including VEGF signaling [264], cell migration [265], proliferation, and cell-cell junction formation [266]. While many stages of angiogenesis have exhibited mechanosensitivity in isolation, little is known about how functional mechanical loading regulates the concerted processes of angiogenesis.

The bone environment is one of the few in which the effects of abluminal forces on vascularization have been investigated [136, 267]. Early functional loading disrupted vascularization, whereas delayed loading enhanced vascular networks [136]; however, the specific parameters of loading involved in regulating angiogenesis are poorly defined. Functional loading typically occurs with a frequency around 1 Hz [148], and strain magnitude is an important regulator of bone formation. Peak bone formation occurs at low strains, whereas a fibrous response occurs at high strains; 10% strain is thought to be a transition point between an anabolic and catabolic response [142]. Furthermore, functional loading includes modes of loading other than pure compression. For example, large bone defects include a shear interface between intact cortical bone and the soft defect space or implanted graft material [268], and shear has been shown to reduce revascularization of bone [267].

The in vivo injury environment is highly complex, which hinders mechanistic understanding of the role played by each loading parameter. To exert more precise control and begin to better understand these effects, we employed an in vitro model system of angiogenesis. Microvascular fragments (MVF) are segments of mature vasculature and thus composed of multiple cell types, including endothelial cells, smooth muscle cells,

mesenchymal stem cells, and fibroblasts [108, 269]. MVF are typically cultured in collagen-based hydrogels [107], which has similarities to the collagenous granulation tissue characteristic of early stage wound healing. MVF represent a 3D culture system that recapitulates the major stages of in vivo angiogenesis including sprout tip cell selection, matrix invasion, neovessel elongation, and branching. These processes require complex cell-cell and cell-matrix interactions, which are vastly simplified in traditional 2D monolayer cultures. Additionally, MVF are known to respond to mechanical cues. Increased collagen matrix density decreased the rate of MVF growth and branching [113], and one of the relatively few studies examining the effect of abluminal forces observed MVF alignment parallel to the direction of applied tension [111].

In this chapter, we studied the effects of three strain magnitudes, 5%, 10%, and 30%, and two modes of loading, compression and compression with a shear interface zone, on MVF network growth when applied early and when delayed. Based on existing bone literature, we hypothesized that vascularization would be enhanced by delayed, moderate compression and inhibited by early, high magnitude compression and in regions of shear stress. We subsequently investigated the changes in viability, proliferation, perivascular coverage, and gene expression profiles associated with early vs. delayed loading. Based on our previous in vivo results, we hypothesized that early loading would decrease cell viability, pericyte-vessel attachment, and expression of genes associated with early stage angiogenesis, such as sprout tip cell selection, thereby leading to impaired vascular networks. Conversely, we hypothesized that delayed loading would increase cellular proliferation and increase expression of genes associated with later stages of angiogenesis, such as matrix invasion, collective cell migration, and cell recruitment, thereby leading to

more extensive and mature vascular networks. Finally, we investigated the role of YAP mechanotransduction in the differential angiogenic responses to early and delayed loading.

7.2 Methods

7.2.1 MVF Isolation and Culture

MVF were isolated as previously described [107]. Briefly, epididymal fat pads of retired breeder Lewis rats were harvested, minced, and digested in a collagenase solution. MVF were obtained through selective filtration to retain multicellular structures between 20-200 μm. MVF were suspended at a density of 20,000 fragments/mL in 3% collagen gels supplemented with 50 μg/mL decorin (DCN) to improve construct dimensional stability [219]. Gels were formed by 15-20 minutes of incubation at 37 °C in custom polycarbonate molds to create gels with a diameter of 5 mm and a height 4 mm. MVF-containing gels were cultured in serum-free media supplemented with 10 ng/mL recombinant human vascular endothelial growth factor (rhVEGF; R&D Systems, Minneapolis, MN) [112]. Media was changed on days 3, 5, and 7 of culture, and gels were fixed with 4% paraformaldehyde on day 10.

7.2.2 Dynamic Loading

MVF-containing gels were loaded using an Electroforce 5500 with a multi-specimen compression chamber containing a 24-well plate loading assembly (TA

Instruments; New Castle, DE). Loading was applied in a triangle wave with amplitudes corresponding to 5%, 10%, or 30% strain (0.2 mm, 0.4 mm, and 1.2 mm, respectively) at a frequency of 1 Hz. Gels were loaded in compression using polyetheretherketone (PEEK) platens with a diameter greater than that of the gel (1 cm) or in compression with a shear interface zone (compression+shear) using PEEK platens with a 3 mm gel-contacting diameter. Loading was applied continuously, breaking only for media changes, for either the first five days of culture, early loading, or the final five days of culture, delayed loading. To ensure gels remained centered within the well, gels sat within the inner diameter of 1 mm thick 3D printed poly(lactic-co-glycolic acid) rings during loading.

To study the effects of loading type and time of initiation, dynamic loading at 5%, 10%, and 30% strain experiments included the following groups (n=6/group): early compression, early compression+shear, delayed compression, delayed compression+shear, and a non-loaded control.

7.2.3 Staining, Imaging, and Image-Based Analyses

To assess network morphology at day 10, fixed gels were stained with rhodamine-labeled Griffonia simplicifolia (GS-1) lectin (Vector Labs, Burlingame, CA) at a concentration of 5 μg/mL in phosphate buffered saline (PBS) overnight at 4 °C (n=6/group). Gels were imaged using a Zeiss 700 confocal microscope with a 5X objective. The entire diameter of each gel was imaged to a depth of 200 μm. Confocal z-stacks were median filtered, deconvolved, and thresholded using Amira for Life Sciences (ThermoFisher Scientific, Waltham, MA). Islands smaller than 30 voxels (e.g. single cells,

debris, or noise) were also removed using Amira. Thresholded images were exported for skeletonization and quantification of length and branching using the 4-D open snake method [270] of the Farsight Toolkit [271, 272].

Viability and proliferation of non-loaded vs. loaded MVF were measured at day 3 for early loading and at day 7 for delayed loading. Viability was determined using a live/dead assay kit performed according to manufacturer's instructions (ThermoFisher). Gels were imaged at 10X, and three randomly selected fields were imaged per gel to a depth of 25 μm. Maximum intensity z-projections were created to quantify viability using Fiji's Analyze Particles feature. Percent viability was calculated as the pixel area of live cells (green channel) over the pixel area of all cells (green+red channels). Proliferation was assessed using a Click-iT EdU Alexa Fluor 594 Imaging Kit (ThermoFisher; n=3/group/time point). EdU was added to media at a concentration of 10 μM at days 2 and 6 of culture and incubated for 24 hours before gels were fixed at days 3 and 7. Gels were imaged at 10X to a depth of 25 μm, and four images were taken to capture the diameter of each gel. Proliferation was quantified as the number of EdU+ nuclei over the total number of nuclei.

To assess the degree of perivascular coverage of endothelial cells by smooth muscle cells over time, non-loaded gels were fixed at days 0, 3, 5, 7, and 10 (n=3/time point), early loaded samples were analyzed at days 3, 5, and 10 (n=3/time point), and delayed loaded samples were analyzed at days 7 and 10 (n=3/time point). Following fixation, gels were stained with Alexa Fluor 488-conjugated anti-alpha smooth muscle actin (αSMA) antibody (ab184675, Abcam, Cambridge, UK) at a 1:100 dilution, DyLight 649-conjugated GS-1 isolectin B4 (DL-1208, Vector Labs) at 5 μg/mL, and DAPI (ThermoFisher) at a 1:1000

dilution. Gels were imaged at 40X to a depth of 25 μm, which is the approximate depth of a single vessel. A region of interest (ROI) was drawn around vascular structures, and signal overlap between αSMA and isolectin B4 were quantified for the ROI using Manders coefficients as determined by the Fiji plugin coloc2 [273].

7.2.4 Gene Expression Analyses

To assess gene expression changes due loading, RNA was harvested from non-loaded and loaded constructs 24 hours after load initiation (i.e. after 24 hours of culture total for early loaded samples and their non-loaded controls and after 6 days of culture total for delayed loaded samples and their non-loaded controls). RNA was collected from non-loaded and loaded gels at both early and delayed time points (n=5-6/group/time point). RNA was extracted using Qiagen MinElute kits, and cDNA was made using Qiagen RT^2 First Strand kits (Qiagen, Hilden, Germany). RNA concentration as determined by NanoDrop spectrophotometer (ThermoFisher) was used to ensure cDNA concentrations were equivalent. Taqman probes were used to assess gene expression of 43 genes known to be involved in various stages of angiogenesis (see Table 1) and five housekeeping genes. Gene expression was quantified using a Biomark real-time PCR integrated fluidic circuit array (Fluidigm, South San Francisco, CA). Rat universal cDNA (Gene Scientific, Rockville, MD) and ultrapure water (ThermoFisher) were used as positive and negative controls, respectively. Data were normalized on a per sample basis to the mean of three housekeeping genes that did not have significantly different levels of expression across groups (Gapdh, Ubc, Hrpt1) using the ΔCt method.

Table 1. List of Genes Measured with Taqman Probes Using Fluidigm System.

Stage of Angiogenesis	Gene	Protein Encoded	Taqman Reference Number
Sprout Tip Cell Selection	Notch1	Notch 1	Rn01758633_m1
Sprout Tip Cell Selection	Jag1	Jagged 1	Rn00569647_m1
Sprout Tip Cell Selection	Dll4	Delta-like ligand 4	Rn01512886_m1
Sprout Tip Cell Selection	Tie1	Tie 1	Rn01417182_m1
Sprout Tip Cell Selection	Tek (Tie2)	Tie 2	Rn01433346_m1
Sprout Tip Cell Selection	Cxcr4	C-X-C Motif Chemokine Receptor 4	Rn01483207_m1
Vessel Growth and Maturation	Vegfa	Vascular endothelial growth factor a	Rn01511602_m1
Vessel Growth and Maturation	Vegfc	Vascular endothelial growth factor c	Rn01488076_m1
Vessel Growth and Maturation	Flt1 (Vegfr1)	Vascular endothelial growth factor receptor 1	Rn01409533_m1
Vessel Growth and Maturation	Kdr (Vegfr2)	Vascular endothelial growth factor receptor 2	Rn00564986_m1
Vessel Growth and Maturation	Angpt1	Angiopoietin 1	Rn01504818_m1
Vessel Growth and Maturation	Angpt2	Angiopoietin 2	Rn01756774_m1
Vessel Growth and Maturation	Pdgfb	Platelet derived growth factor subunit b	Rn01502596_m1
Matrix Invasion and Deposition	Mmp2	Matrix metalloproteinase 2	Rn01538170_m1
Matrix Invasion and Deposition	Mmp9	Matrix metalloproteinase 9	Rn00579162_m1
Matrix Invasion and Deposition	Mmp14	Matrix metalloproteinase 14	Rn00579172_m1
Matrix Invasion and Deposition	Timp2	Tissue inhibitor of metalloproteinase 2	Rn00573232_m1
Matrix Invasion and Deposition	Timp3	Tissue inhibitor of metalloproteinase 3	Rn00441826_m1
Matrix Invasion and Deposition	CtsK	Cathepsin K	Rn00580723_m1

Table 1 continued

Cell Adhesion and Migration	Cdh5	Vascular endothelial cadherin	Rn01536708_m1
Cell Adhesion and Migration	Cdh2	Neural cadherin	Rn00580099_m1
Cell Recruitment	Bmp2	Bone morphogenetic protein 2	Rn00567818_m1
Cell Recruitment	Cxcl12 (Sdf1a)	Stromal derived factor 1 alpha	Rn00573260_m1
Cell Recruitment	Fgf	Fibroblast growth factor	Rn00570809_m1
Cell Recruitment	S1pr1	Sphingosine 1-phosphate receptor 1	Rn02758712_s1
Cell Recruitment	Tgfb1	Transforming growth factor b	Rn00572010_m1
Cell Adhesion and Migration	Pecam1	Platelet endothelial cell adhesion molecule 1	Rn01467262_m1
Cell Adhesion and Migration	Itga5	Integrin alpha 5	Rn01761831_m1
Cell Adhesion and Migration	Itgb1	Integrin beta 1	Rn00566727_m1
Cell Adhesion and Migration	Itgav	Integrin alpha v	Rn01485633_m1
Cell Adhesion and Migration	Itgb3	Integrin beta 3	Rn00596601_m1
Cell Adhesion and Migration	Itga2	Integrin alpha 2	Rn01489315_m1
Inflammation and Apoptosis	Il12 *	Interleukin 12	Rn00584538_m1
Inflammation and Apoptosis	Il10 *	Interleukin 10	Rn01483988_g1
Inflammation and Apoptosis	Tnfa	Tumor necrosis factor alpha	Rn01525859_g1
Matrix Invasion and Deposition	Fn	Fibronectin	Rn00569575_m1
Matrix Invasion and Deposition	Coll1a1	Collagen type 1 alpha 1	Rn01463848_m1
Mechanotransduction	Amotl2	Angiomotin-like 2	Rn01446301_m1
Mechanotransduction	Ankrd1 *	Ankyrin repeat domain 1	Rn00566329_m1
Mechanotransduction	Ctgf	Connective tissue growth factor	Rn01537279_g1
Mechanotransduction	Cyr61	Cyr61	Rn00580055_m1
Inflammation and Apoptosis	Bax	Bcl-2-associated X protein	Rn01480161_g1

Table 1 continued

Inflammation and Apoptosis	Bcl2	B-cell lymphoma 2	Rn99999125_m1
Housekeeping	Gapdh	Glyceraldehyde 3-phosphate dehydrogenase	Rn01775763_g1
Housekeeping	Bactin	Beta-actin	Rn00667869_m1
Housekeeping	Hprt1	Hypoxanthine-guanine phosphoribosyltransferase	Rn01527840_m1
Housekeeping	Ubc	Poly-ubiquitin C	Rn01499642_m1
Housekeeping	Ppia	Peptidylprolyl isomerase A	Rn00690933_m1
** Indicates gene expression was below the limit of detection and thus excluded from analyses.*			

7.2.5 Multivariate Analysis of Gene Expression Data

Partial least squares discriminant analysis (PLSDA) was performed in MATLAB (Mathworks, Natick, MA) using Cleiton Nunes's partial least squares algorithm, which is available on the MathWorks File Exchange. To avoid biasing results with the absolute magnitude of different genes' expression levels, data were z-scored prior to being analyzed with PLSDA. Orthogonal rotations were applied to the z-scores to maximally separate groups (non-loaded, compressive loading, and compression+shear loading) based on latent variables 1 and 2 (LV1 and LV2) created by the PLS algorithm. LV loading plots show the mean and standard deviation of each gene's relative contribution to the latent variable; mean and standard deviation were calculated using Monte Carlo sub-sampling that iteratively excluded and replaced samples 1000 times [274].

7.2.6 YAP Inhibition

The YAP inhibitor verteporfin (VP; MilliporeSigma, Burlington, MA) was dissolved in DMSO and added to serum-free MVF media at a concentration 5 μM. Non-VP controls received an equal volume of DMSO. VP and DMSO were added to MVF-containing gels 30 minutes prior to initiation of loading to allow diffusion throughout the gel. After 24 hours of loading, RNA was collected from early and delayed samples as above. The groups for the YAP inhibition study were compression+shear + VP, compression+shear + DMSO carrier only, non-loaded + VP, and non-loaded + DMSO at both early and delayed time points (n=5-6/group). All culture of samples containing light-sensitive VP [275] was conducted in the dark.

7.2.7 Statistical Analysis

For day 10 MVF network morphology data, a two-way ANOVA was used to compare early vs. delayed loading and compression vs. compression+shear loading. A one-way ANOVA was used to compare early loading to the non-loaded control and delayed loading to the non-loaded control. To directly compare the effects of different load magnitudes, loaded groups were normalized to their respective non-loaded controls and analyzed within time point and loading type (e.g. early compression+shear compared at 5%, 10%, and 30% strain) using a one-way ANOVA. Viability, proliferation, and perivascular coverage data were analyzed by two-way ANOVA. Gene array data were studied in aggregate using PLSDA as detailed above, and the expression levels of individual genes were compared within time point using a one-way ANOVA. The effect of verteporfin on gene expression of non-loaded vs. loaded constructs was analyzed with a

two-way ANOVA. Bonferroni's post hoc test followed all ANOVAs. All statistical analyses were performed in GraphPad Prism 5 with α=0.05. Data are presented as mean ± standard error of the mean.

7.3 Results

7.3.1 Non-Loaded MVF Progress Through Distinct Stages of Angiogenesis in vitro

Under static, non-loaded culture conditions, MVF form in vitro networks in a predictable time course. At day 0 (e.g. day of harvest), the freshly isolated fragments have characteristically rounded ends, denoted by white arrows in Figure 7.1. By day 3 in culture, the fragment ends adopt a pointed appearance, indicative of early sprouting and invasion of the extracellular matrix. By day 5, the initial sprouts extend and begin to branch. Existing sprouts continue to elongate between days 5-7, and some secondary branching appears between days 7-10. Because sprout and branch initiation processes occur within the first five days of culture, while days 5-10 consist primarily of elongation, we selected days 0-5 as "early loading" and days 5-10 as "delayed loading" (Figure 7.2 A).

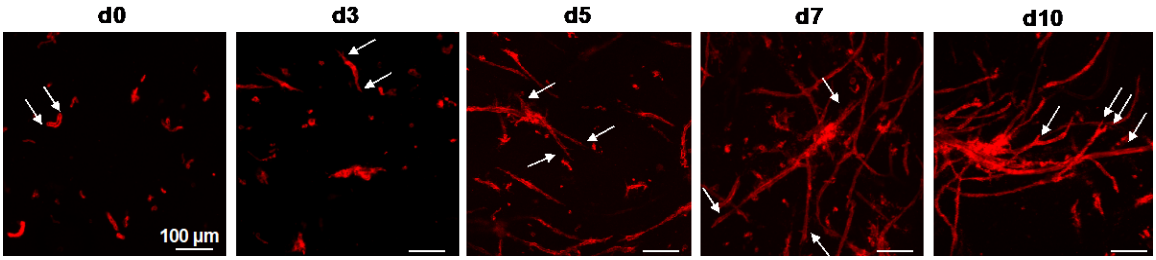

Figure 7.1. Representative images of in vitro MVF network formation over time. White arrows denote ends of freshly isolated fragments (d0) and resulting sprouts (d3, d5,

d7, d10). Maximum intensity z-projections (200 um depth) of samples stained with GS-1 lectin.

7.3.2 MVF Exhibit Sensitivity to Magnitude and Mode of Dynamic Loading

At 5% strain, delayed loading led to significantly greater total network length (two-way ANOVA, Bonferroni post hoc $p<0.05$) and number of branches (post hoc $p<0.05$) than early loading (Figure 7.2 B-C). There was no effect of loading type at 5% strain (e.g. compression vs. compression+shear) and no significant interaction effect. Delayed 5% loading, both compression and compression+shear, increased length (one-way ANOVA, Bonferroni post hoc $p<0.01$ and $p<0.001$, respectively) and branching (post hoc $p<0.05$ and $p<0.01$, respectively) relative to the non-loaded control. Early 5% loading was no different than the non-loaded control.

At 10% strain, delayed loading again significantly increased total network length (two-way ANOVA, overall effect $p<0.05$) and number of branches (overall effect $p<0.05$) relative to early loading (Figure 7.2 D-E). At 10% strain, compression+shear loading also increased length (overall effect $p<0.05$) and branching (overall effect $p<0.05$) relative to compression only. There was no significant interaction effect. Delayed compression+shear loading increased total length (one-way ANOVA, Bonferroni post hoc $p<0.01$) and number of branches (post hoc $p<0.01$) compared to the non-loaded control. Early 10% loading was no different than the non-loaded control.

At 30% strain, delayed compression+shear loading significantly increased total network length (two-way ANOVA, Bonferroni post hoc $p<0.001$) and number of branches (post hoc $p<0.001$) compared to early compression+shear (Figure 7.2 F-G). Delayed

compression+shear also increased length (post hoc $p<0.01$) and branching (post hoc $p<0.01$) relative to delayed compression alone. There was no significant interaction effect. Further, delayed compression+shear significantly increased length (one-way ANOVA, Bonferroni post hoc $p<0.01$) and branching (post hoc $p<0.01$) over the non-loaded control. At 30% strain, early loading, both compression and compression+shear, decreased the total network length relative to the non-loaded control (one-way ANOVA, Bonferroni post hoc $p<0.01$ and $p<0.05$, respectively). Early compression only also decreased branching as compared to the non-loaded control (post hoc $p<0.05$). Qualitatively, the early loaded constructs at day 10 appear to have only early stage sprouts (Figure 7.3) more comparable to the non-loaded sprouting observed at day 3 (Figure 7.1).

When all loaded groups' length and branching were normalized to that of their respective non-loaded experimental controls, early loading exhibited significant strain magnitude-dependence (Figure 7.4). 30% compression decreased network length and branching relative to both 5% (one-way ANOVA, Bonferroni post hoc $p<0.01$) and 10% compression (post hoc $p<0.05$). 30% compression+shear decreased network length and branching relative to 10% compression+shear (post hoc $p<0.05$). There were no statistically significant differences due to strain magnitude among delayed loading conditions.

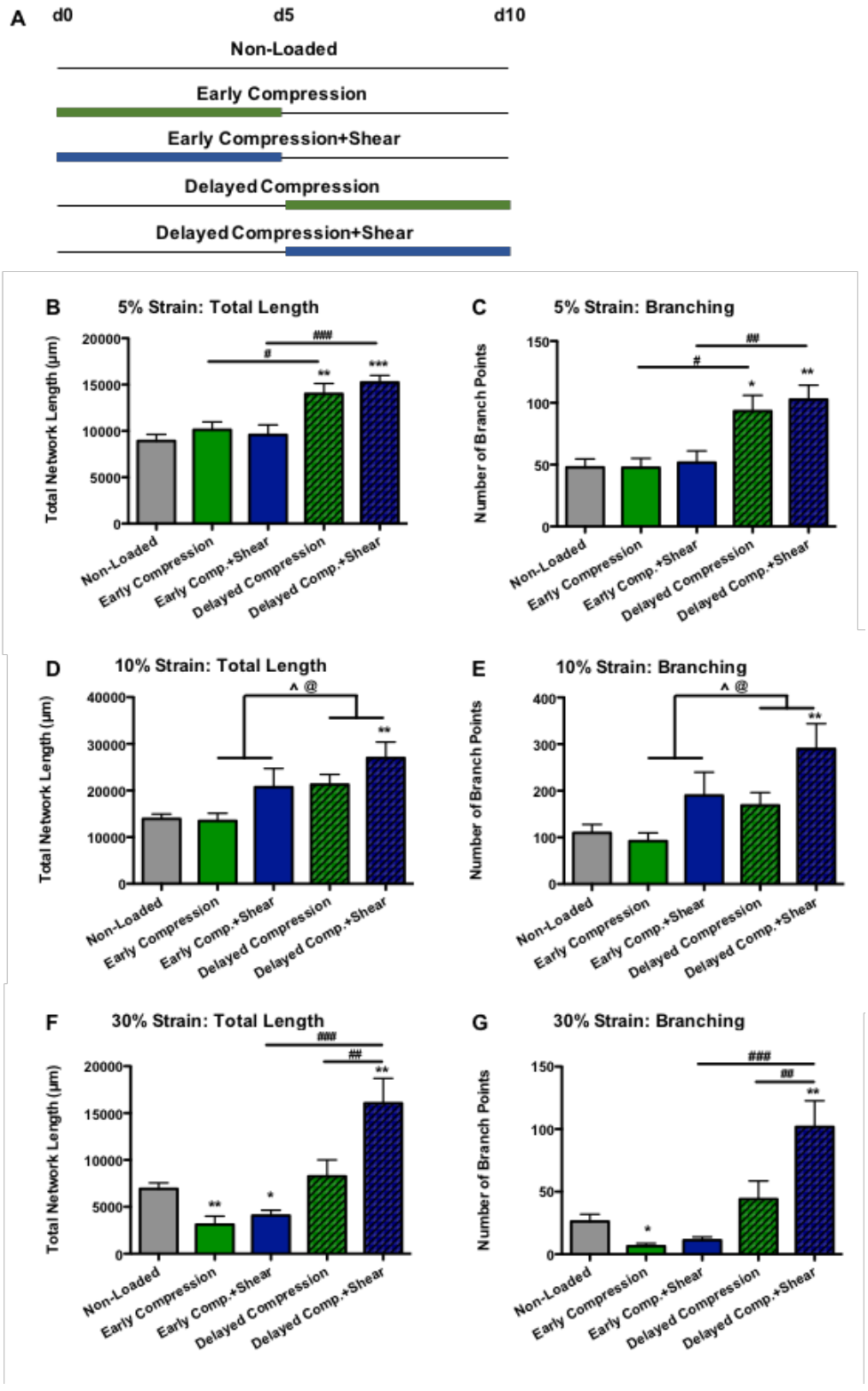

Figure 7.2. Quantification of MVF growth under strain. Experimental design (A) and quantification of MVF network length and branching at 5% (B-C), 10% (D-E), and 30%

(F-G) strain. Quantification based on 3D confocal z-stacks of 200 um depth. * significant difference from NL; 1-way ANOVA, * p<0.05, ** p<0.01, *** p<0.001. # 2-way ANOVA with Bonferroni post hoc test; @ overall effect of loading type; ^ overall effect of time; post hoc # p<0.05, ## p<0.01, ### p<0.001. n=6/group.

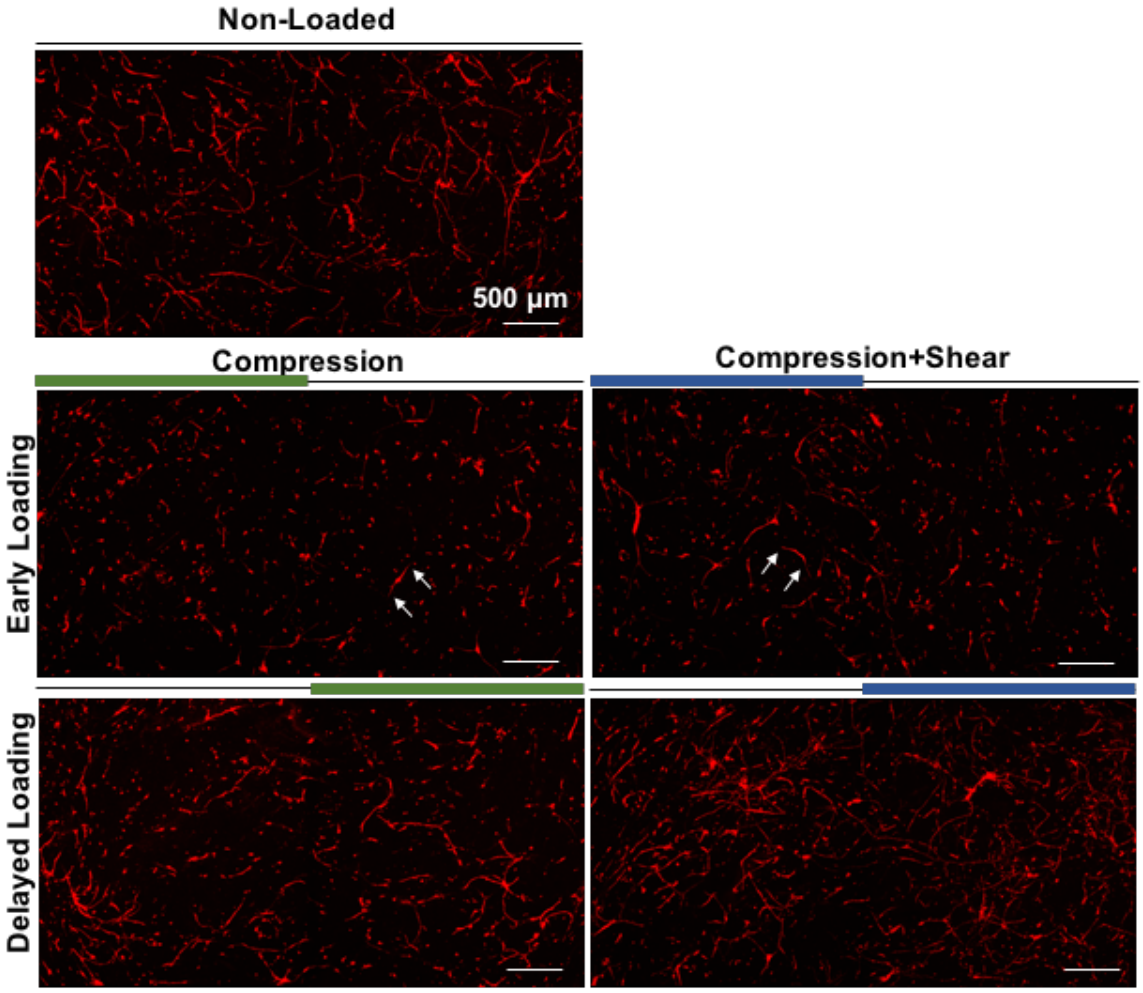

Figure 7.3. Representative images of MVF networks formed under 30% strain. Early compression and early compression+shear groups exhibit only very early stage sprouts, white arrows. Delayed compression+shear appears qualitatively more densely vascularized than the non-loaded or delayed compression groups. Maximum intensity z-projections (200 um depth) of samples stained with GS-1 lectin at day 10 of culture.

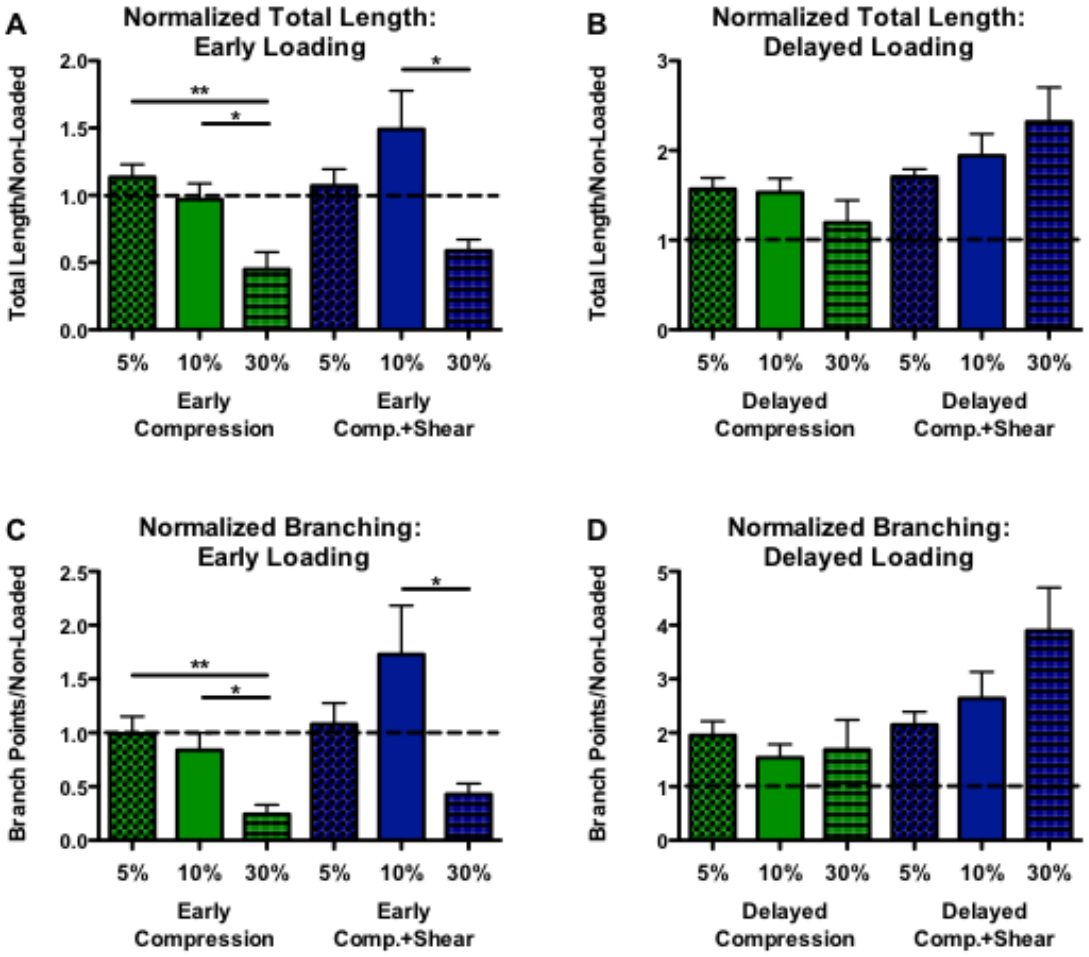

Figure 7.4. Length and branching under 5%, 10%, and 30% strain normalized to non-loaded group. 1-way ANOVA, * $p<0.05$, ** $p<0.01$. n=6/group.

7.3.3 Dynamic Loading Differentially Affects MVF Proliferation but not Viability or Pericyte-Vessel Attachment

Based on our results comparing strain magnitude and type of loading, we selected early and delayed 30% compression+shear loading, the loading parameters that led to the greatest network morphology differences, for subsequent cellular analyses.

To assess the effects of dynamic loading on MVF viability, non-loaded and loaded samples were live/dead stained on days 3 (early loading) and 7 (delayed loading) of culture (Figure 7.5). There was no effect of loading on viability, and viability was greater at day 7 of culture than at day 3 for both non-loaded (two-way ANOVA, Bonferroni post hoc $p<0.01$) and loaded samples (post hoc $p<0.01$). Viability was approximately 75% at day 3 and 90% at day 7.

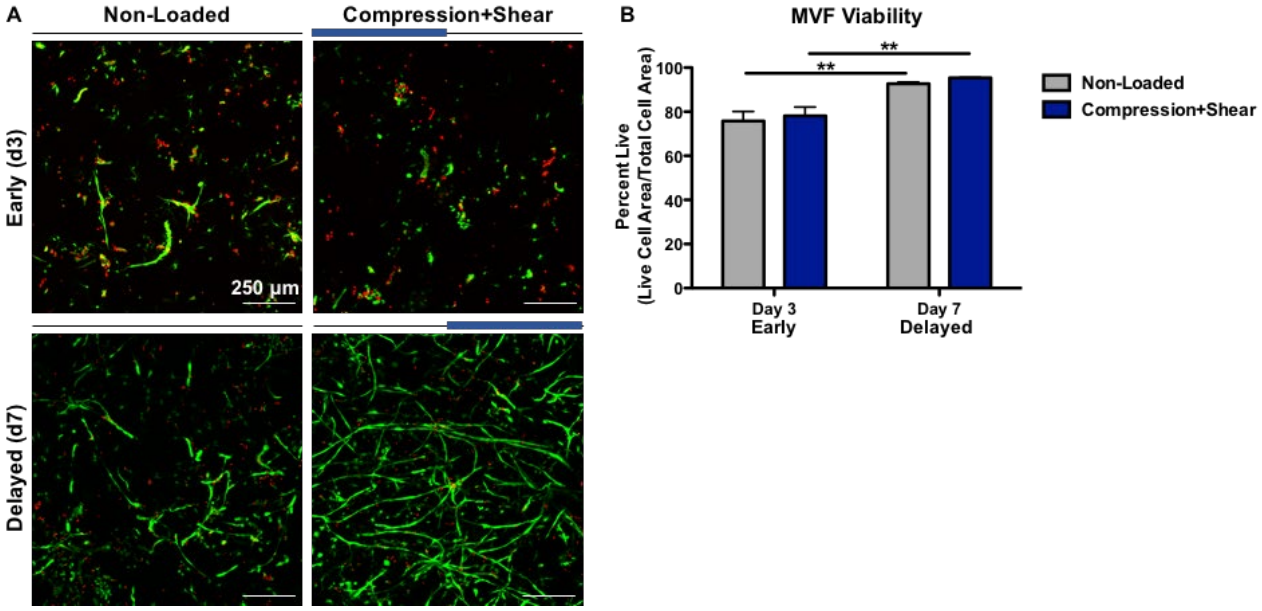

Figure 7.5. MVF viability under early and delayed 30% compression+shear loading. A) Representative maximum intensity z-projections (25 um depth) of calcein (green; live) and ethidium homodimer (red; dead) stained MVF at days 3 (early) and 7 (delayed). B) Image-based quantification of live/dead stain. 2-way ANOVA, ** Bonferroni post hoc $p<0.01$. No effect of loading. No interaction effect. n=3 random images/gel, n=3 gels/group/time point.

Proliferation was measured by EdU incorporation also at days 3 and day 7. There was no effect of early loading on proliferation, and approximately 5-10% of cells were proliferative at day 3 (Figure 7.6). Proliferation was greater at day 7 (two-way ANOVA,

overall effect p<0.001), and delayed loading led to increased proliferation, approximately 25%, compared to non-loaded controls, approximately 15% (two-way ANOVA, Bonferroni post hoc p<0.05). There was a significant disordinal interaction effect (p<0.05), indicating that early loading and delayed loading have opposite effects on cellular proliferation.

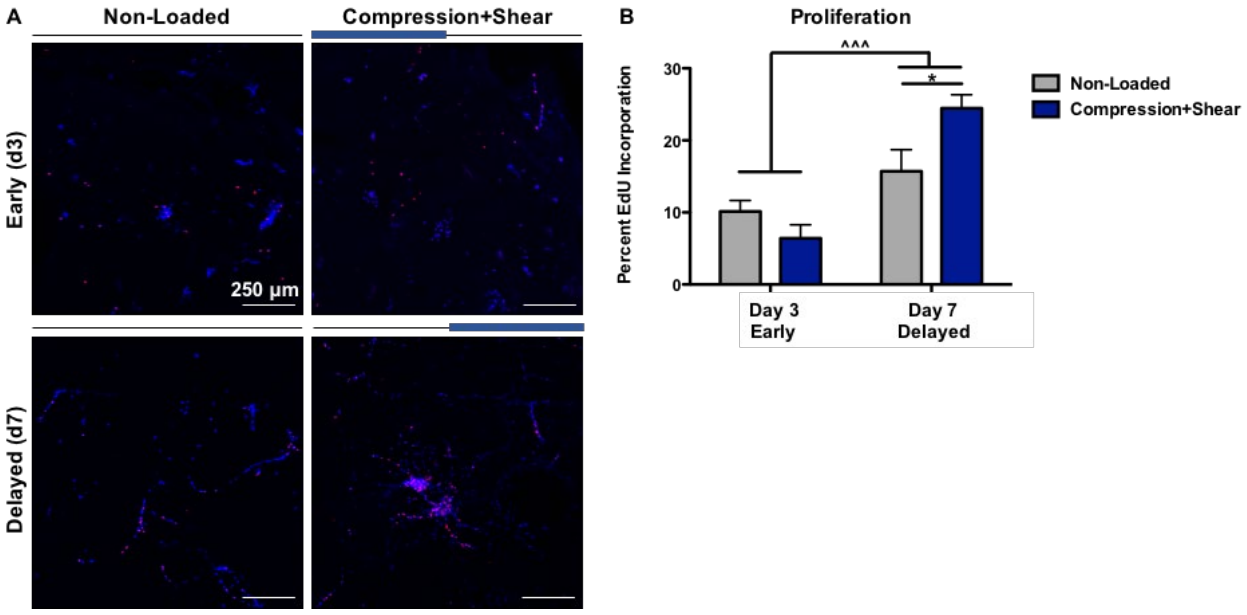

Figure 7.6. MVF proliferation under early and delayed 30% compression+shear loading. A) Representative maximum intensity z-projections (25 um depth) of DAPI (blue; all cells) and EdU (red; proliferating cells) stained MVF at days 3 (early) and 7 (delayed). B) Image-based quantification of proliferation. 2-way ANOVA, ^^^ overall effect of time, p<0.001, post hoc effect of loading ** p<0.01. Significant interaction effect, p<0.05. n=3 gels/group/time point.

The interaction between αSMA+ pericytes and endothelial cells of vessels was assessed at various time points. There were no significant differences in perivascular coverage of endothelial cells due to either early or delayed loading at any time point (Figure 7.7). Perivascular coverage was approximately 75-80% at day 0 through day 10.

Qualitatively, there tended to be relatively less pericyte coverage at the ends of nascent sprouts.

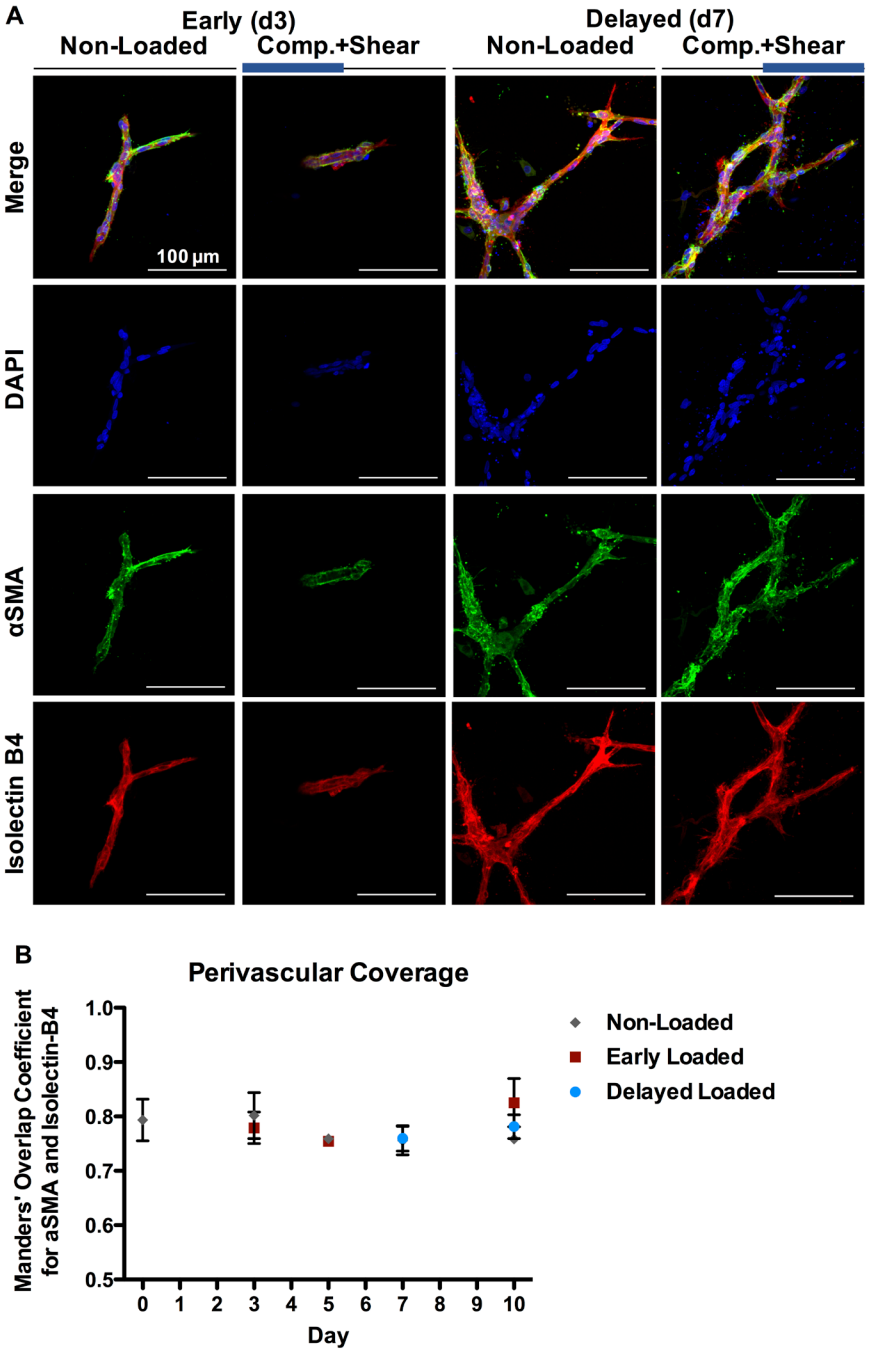

Figure 7.7. Perivascular coverage of MVF under early and delayed 30% compression+shear loading. A) Representative maximum intensity z-projections (25 um

depth) of DAPI (blue; nuclei), αSMA (green; perivascular SMCs), and isolectin B4 (red; ECs) stained MVF at days 3 (early) and 7 (delayed). B) Image-based quantification of perivascular coverage. 2-way ANOVA, no significant differences due to loading or time. n=3 gels/group/time point.

7.3.4 Dynamic Loading Differentially Regulates MVF Gene Expression

Partial least squares discriminant analysis (PLSDA) was performed on gene expression data to create profiles of the RNA-level changes that were associated with the differential effects of early and delayed 30% strain loading (compression and compression+shear). For both the early and delayed time points, PLSDA created a latent variable (LV2) that separated non-loaded from loaded samples (Figure 7.8 A, C). LV2 is composed of a weighted average of genes, and each individual gene's relative contribution can be visualized with a latent variable loading plot. In general, gene expression was downregulated by early loading (negative values in Figure 7.8 B) and instead upregulated by delayed loading (positive values in Figure 7.8 D).

When considered in aggregate, genes known to be involved in sprout tip cell selection (5 of 6) and protease homeostasis (6 of 6) tended to be downregulated by early loading. In contrast, genes known to be mechanosensitive (2 of 3) and involved in matrix deposition (2 of 2) tended to be upregulated by early loading. When considered at the individual gene level, Tie1, Mmp14, Timp3, Cxcr4, Cxcl12, Mmp9, and Itgav were all significantly downregulated by early loading. Cyr61, Ctgf, Vegfa, and Fgf2 were all significantly upregulated by early loading (Figure 7.9). These genes are some of the strongest contributors to the early loading LV2, as they have the largest absolute values in Figure 7.8 B.

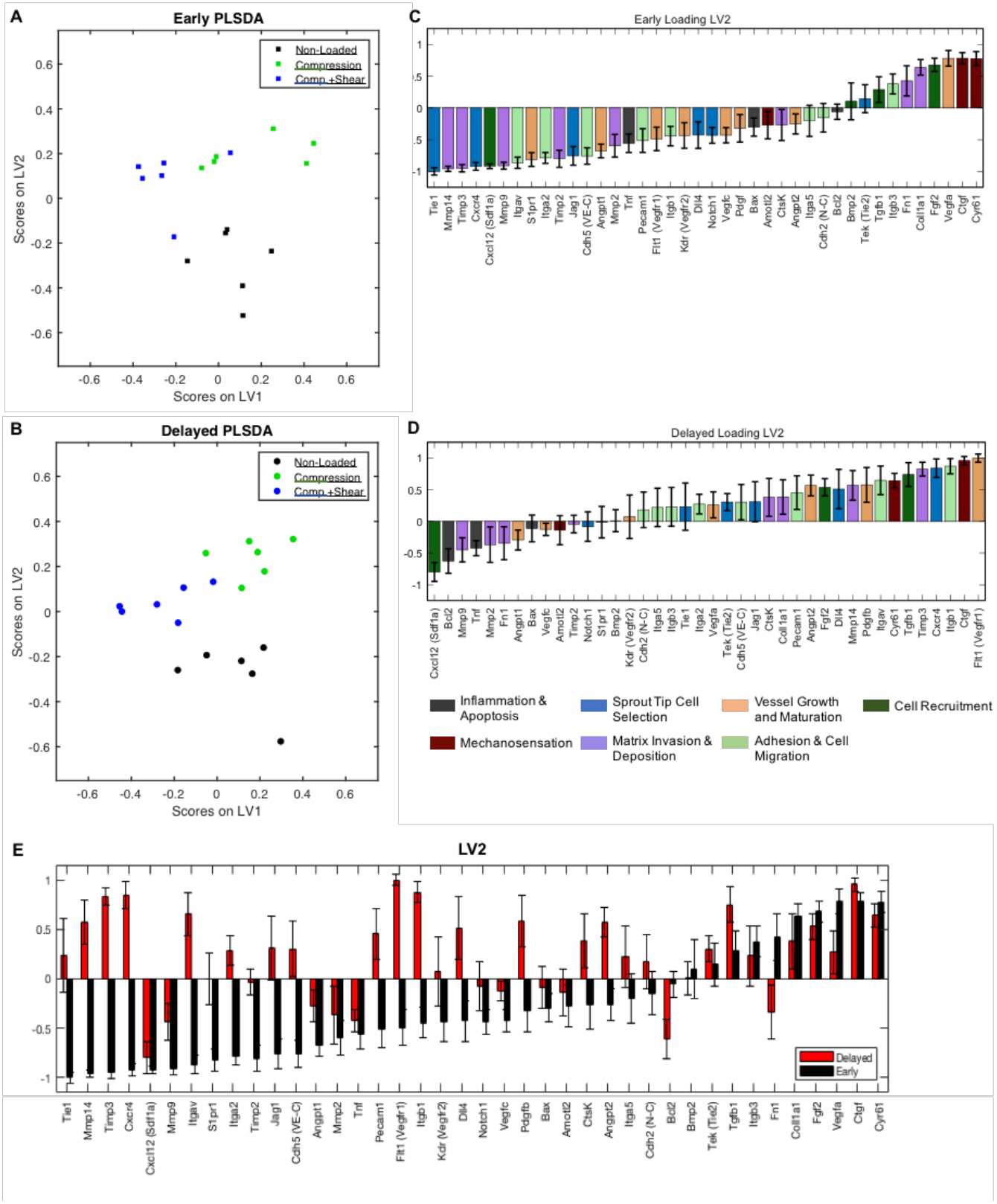

Figure 7.8. PLSDA of MVF gene expression under 30% compression and compression+shear loading. PLSDA plots of latent variable 2 vs. latent variable 1 reveals

separation of loaded and non-loaded samples along LV2 for both early loading conditions (A) and delayed loading conditions (B). Loading plots of early LV2 (C) and delayed LV2 (D) demonstrate the relative contribution of each gene to the separating LV2. Genes are color coded by angiogenesis functions they are known to be involved in. E) When interleaved, the loading plots of early vs. delayed loading reveal differential regulation of a number of genes. n=6 gels/group. Error bars created by 1000 iterations of Monte Carlo sub-sampling.

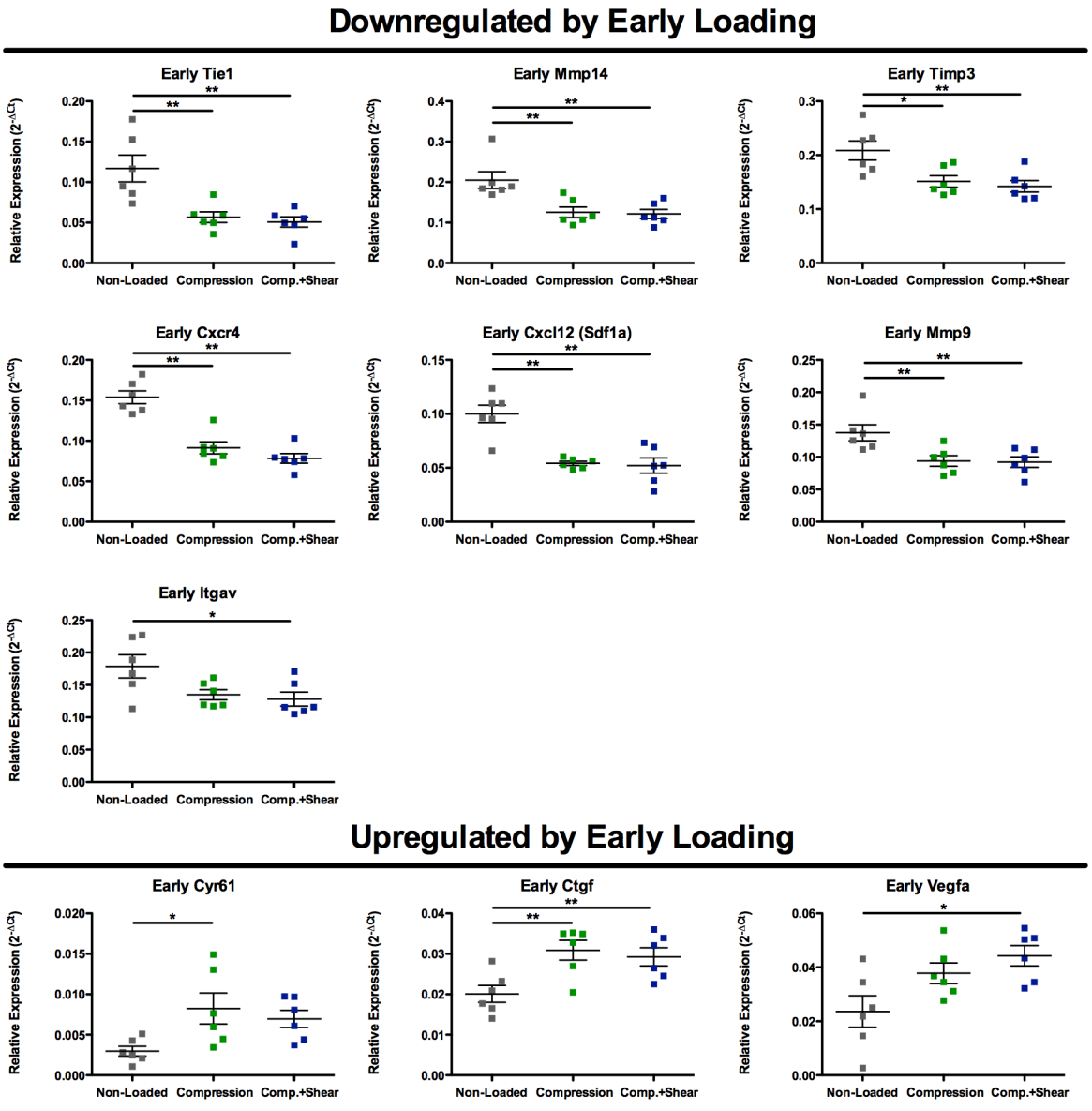

Figure 7.9. Individual genes significantly affected by early loading. 1-way ANOVA, Bonferroni post hoc *p<0.05, **p<0.01. n=6/group.

When considered in aggregate, genes known to be involved in sprout tip cell selection (5 of 6), adhesion and migration (8 of 8), and mechanosensation (2 of 3) tended to be upregulated by delayed loading. Genes known to be involved in inflammation and apoptosis (3 of 3) tended to be downregulated due to delayed loading. At the individual gene level, the strongest contributors to the delayed loading LV2 are Flt1, Ctgf, Itgb1, Cxcr4, Timp3, and Tgfb1, which are all significantly upregulated by delayed loading, and Cxcl12, which is significantly downregulated by delayed loading (Figure 7.10).

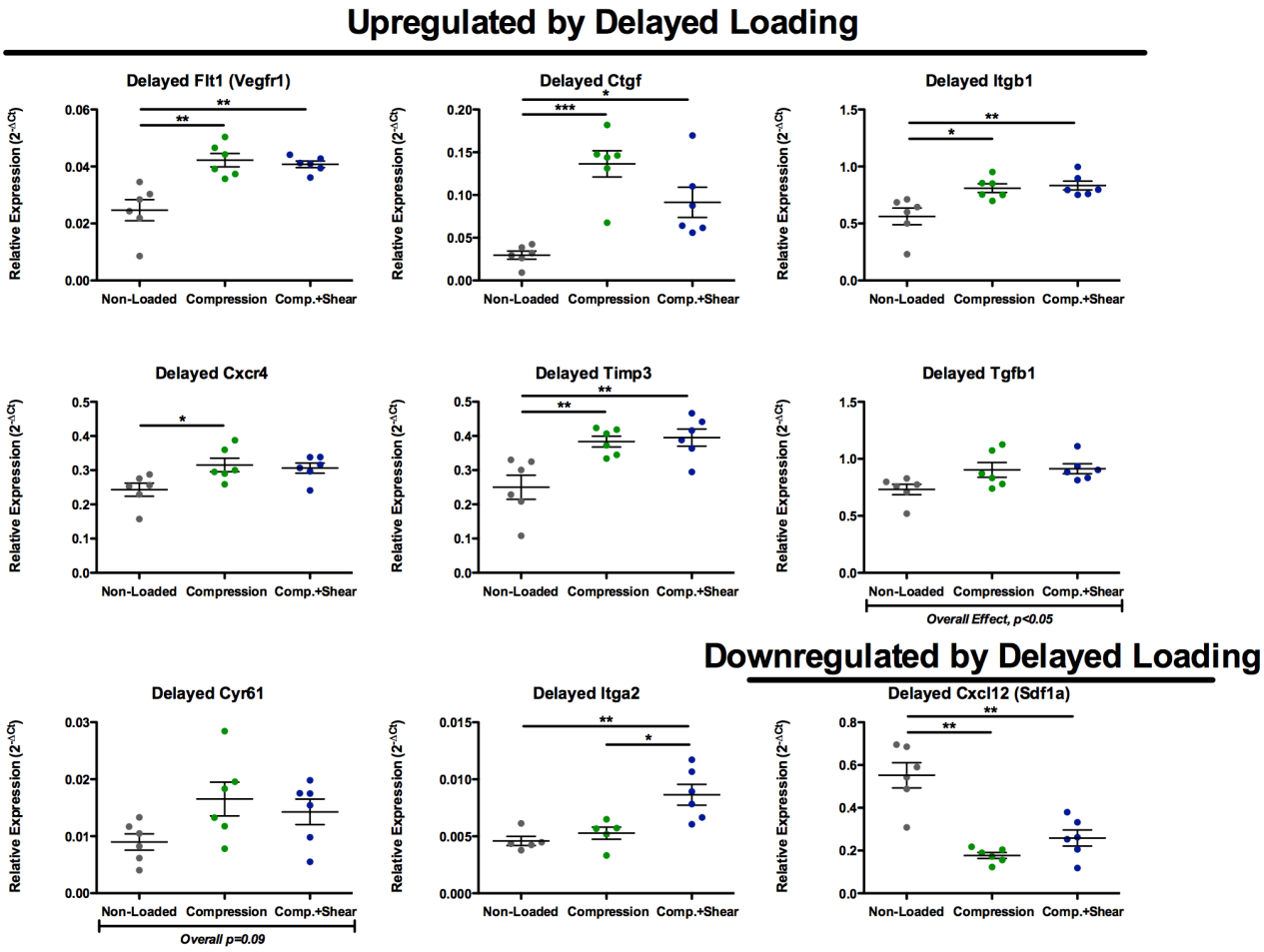

Figure 7.10. Individual genes significantly affected by delayed loading. 1-way ANOVA, Bonferroni post hoc *p<0.05, **p<0.01, ***p<0.001. n=6/group.

A number of these genes are differentially regulated by early vs. delayed loading (Figure 7.8 E). The strongest downregulated contributors to early loading LV2 tend to instead be upregulated by delayed loading, and the strongest upregulated contributors to delayed loading LV2 tend to instead be downregulated by early loading (e.g. Tie1, Mmp14, Timp3; Flt1 or Vegfr1, Itgb1, Cxcr4). There are two strongly upregulated contributors to both early LV2 and delayed LV2: Ctgf and Cyr61, which are canonical targets of the YAP mechanotranduction signaling pathway [276].

Interestingly, of the 43 genes tested, there was only one gene with statistically significant differences in expression by delayed compression vs. compression+shear samples, despite the large morphological differences observed at day 10. Itga2 showed a significant difference between compression and compression+shear samples (Figure 7.10). Itga2 expression was upregulated in compression+shear samples relative to compression only (one-way ANOVA, Bonferroni post hoc $p<0.05$) and to the non-loaded control (post hoc $p<0.01$). There were no genes with expression differences between compression and compression+shear loading at the early time point.

7.3.5 YAP is Involved in MVF Response to Delayed Loading

To investigate the increased YAP target expression observed in the gene expression array, a pharmacological inhibitor of YAP, verteporfin (VP), was employed. Since the gene expression profiles of compression and compression+shear were nearly identical, only compression+shear loading was studied. At the early time point, loading increased expression of Ctgf (overall effect $p<0.01$; Figure 7.11), but there was no statistically

significant effect of VP on early gene expression of either Ctgf or Cyr61. At the delayed time point, delayed loading without VP increased expression of both Ctgf (two-way ANOVA, Bonferroni post hoc $p<0.001$) and Cyr61 (post hoc $p<0.001$) relative to the non-loaded control. VP significantly decreased expression of Ctgf (post hoc $p<0.05$) and Cyr61 (post hoc $p<0.001$) by loaded samples.

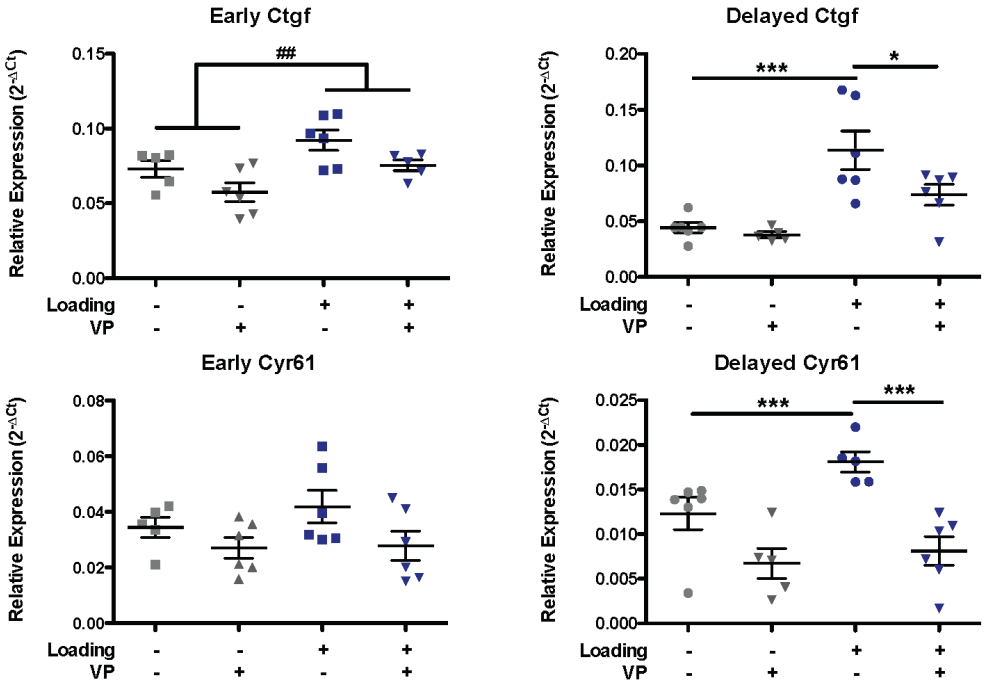

Figure 7.11. Loading-induced expression of YAP target genes with YAP inhibitor VP. 2-way ANOVA, overall effect of loading ## $p<0.01$; Bonferroni post hoc *$p<0.05$, **$p<0.01$, ***$p<0.001$. Delayed Ctgf demonstrated significant interaction effect. n=5-6/group.

7.4 Discussion

Mechanical cues influence tissue regeneration, and although vasculature is known to be mechanically sensitive, remarkably little is known about the effects of abluminal

mechanical stimulation of nascent vessel networks found in healing tissues. Time of loading has previously been shown to be a potent determinant of vascular network formation [136], but regulatory roles of loading parameters such as magnitude and mode remain poorly understood. Here, we tested the effects of dynamic load magnitude, mode, and time of initiation on in vitro MVF growth.

We hypothesized that vascularization would be enhanced by delayed, moderate compression and inhibited by early, high magnitude compression and in regions of shear stress. At all tested strain magnitudes, delayed loading produced longer, more branched vessel networks than early loading. Consistent with our hypothesis, early, high magnitude loading inhibited vessel growth relative to non-loaded controls, and delayed, moderate magnitude loading enhanced vessel growth. However, contrary to our hypothesis, compression+shear loading led to longer, more branched networks than compression alone – particularly at higher strain magnitudes. Differential morphological effects of early vs. delayed 30% compression+shear loading were supported by differences in proliferation. Delayed 30% compression+shear loading significantly increased proliferation, and while early 30% compression+shear did not significantly decrease proliferation relative to its non-loaded control, there was an interaction effect between loading and time. Contrary to our hypothesis, there were no differences in viability or pericyte-vessel attachment due to loading. Gene expression was also differentially regulated by early vs. delayed loading. As hypothesized, genes known to be involved in early stage angiogenesis were downregulated due to early loading, along with many other genes. Genes known to be involved in later stages of angiogenesis, particularly matrix invasion and collective cell migration, were upregulated by delayed loading. Finally, pharmacological inhibition suggests that the YAP

mechanotransduction pathway is involved in the enhanced vascular response due to delayed loading.

Consistent with previous in vivo results [136], all strain magnitudes tested here in vitro showed an overall effect of time of loading, where delayed loading produced greater network length and number of branches. At low strains (5% and 10%), early loading did not affect vessel network formation; however, at a much higher (30%) strain, early loading significantly decreased network length and branching. Together, these data suggest that low magnitude strain may be permissive to early stage angiogenesis, whereas higher magnitude strains disrupt this process. Inhibitory effects of delayed loading were not observed, even at 30% strain. Once a critical stage of vascular network maturity is reached, even high magnitude loading may be permissive to vessel growth. Day 5 was chosen as the inflection point of early vs. delayed loading in the present studies to distinguish between sprout and branch initiation vs. elongation, suggesting that the initial formation of sprouts/branches may be this critical stage. Future work is required to better define a time point or stage of angiogenesis that becomes robust to higher magnitude loads.

Contrary to our hypothesis, compression+shear loading increased vessel length and branching overall compared to compression alone at strains above 5%. While our compression+shear platens were designed to introduce a shear interface zone, the interface of contact between the platen and gel was not visually apparent in the resulting vessel networks, and there was no difference in the spatial distribution of vessels. The compression+shear platens may create shear only at the very superficial surface of the gel but more profoundly change the bulk stress experienced by the gel and likely the local stress and strain gradients. Future computational work may more precisely define these

effects. Considering the platen surface area alone, our compression+shear platens have approximately 36% of the surface area initially in contact with the gels compared to the compression only platens. This difference may have placed the lowest magnitude strains within a similar range of stress, ultimately leading to similar results at 5% strain, but progressively amplified stress differences as strain increased, potentially explaining the morphological differences observed at 10% and 30% strain. However, of the 43 genes tested in our array, only one (Itga2) demonstrated differential expression between delayed compression and compression+shear. These similar gene expression profiles may be due to sampling after only 24 hours of loading; gene expression, and subsequent morphologies, may diverge later within loading. Alternatively, the similar gene expression profiles may suggest that later (after 5 days of loading rather than 24 hours) differences may be primarily mediated by differences in fluid flow patterns, which are difficult to decouple from in vitro loading systems. However, if all effects observed in these experiments were due to an increase in fluid flow and thus nutrient transport, early 30% loading would likely have also had a beneficial effect rather than the inhibitory effect we observed. Interestingly, there were no significant differences between early compression and early compression+shear, suggesting that even if mediated primarily by stress rather than strain, stresses applied by both loading configurations at 30% were inhibitory to early loading.

Looking at the effects of load magnitude in compression only loading reveals a beneficial effect of 5% strain, no statistically significant post-hoc difference between non-loaded and 10% strain, and no effect at 30% strain. These data suggest that there is a “sweet spot” of compressive strain magnitude, even when loading is delayed. In contrast, compression+shear loading increased length and branching at all three magnitudes, and

normalization to the non-loaded control suggests there may be a dose response to compression+shear magnitude that these studies were simply not sufficiently powered to detect. If the observed morphological differences are stress-mediated, the compression+shear platen at 30% strain may have still been within the optimal range that the compression only platen surpassed at 30% strain.

We investigated several cell-level phenomena as possible explanations for the stark morphological changes induced by dynamic 30% compression+shear loading: viability, proliferation, and perivascular-endothelial cell interactions. We hypothesized that early loading may have inhibited network formation by decreasing cell viability or destabilizing pericyte-vessel attachment. However, there were no differences in cell viability or perivascular coverage by αSMA+ cells due to early or delayed loading. Overall viability was higher at day 7 of culture than at day 3. Some cell death may occur shortly after the isolation of MVF, and these dead cells likely remain entrapped within the gel as the live cells proliferate and increase in number. Quantification of perivascular coverage remained at 75-80% at all time points examined, and qualitatively, vessels maintained pericyte coverage along their length except for growing sprout tips. Endothelial cells appear to lead sprout invasion of the matrix, and pericyte proliferation and thus coverage may occur secondarily in response to the primary proliferation and extension of endothelial cells in both non-loaded and loaded constructs. We also hypothesized that cell proliferation may have mirrored the morphological results, with early loading decreasing proliferation but delayed loading increasing proliferation. Indeed, delayed loading increased proliferation. While there was no statistically significant post hoc difference between early loaded and non-loaded samples, there was a significant interaction effect of time and loading. This

suggests that early and delayed loading differentially affect proliferation, with delayed loading having a stimulatory effect and early loading having a (more modest) dampening effect. The proliferation results support the changes in length and branching; however, the underlying biological mechanisms for these changes remained unclear.

To broadly probe a number of processes involved in angiogenesis (e.g. sprout tip cell selection, matrix invasion, etc.), we utilized a high throughput gene expression array. Gene expression profiles of non-loaded vs. loaded MVF were parsed using PSLDA. Overall, more genes were downregulated by early loading, and more genes upregulated by delayed loading. This was true across for genes known to be involved in early stage angiogenesis, e.g. genes known to be involved in sprout tip cell selection, and those known to be involved in later stages, e.g. matrix invasion and collective cell migration.

The strongest contributor to the early loading gene expression was the downregulation of Tie1, an orphan receptor that regulates angiogenic sprouting through Angpt/Tie2 signaling. Tie1 is expressed by active sprout tip cells and is strongly downregulated in quiescent endothelial cells [34], suggesting that early loading shifts endothelial cells to a more quiescent state. Two other genes associated with tip cells were also downregulated by early loading: Cxcr4 and Mmp14. Cxcr4 is expressed by activated tip cells [277] and may also play a role in sprout anastomosis [30]. The ligand for Cxcr4, Cxcl12 or Sdf1, was also downregulated by early loading. Mmp14 is expressed by tip cells that lead the invasion of surrounding matrix [30, 33]. Timp3 is able to inhibit all MMPs [278], and the fact that it was also downregulated by early loading suggests that the homeostatic balance of MMP-Timp activity may be perturbed by early loading. While a number of proteases were downregulated by early loading, the two ECM protein genes

included in our array, Coll1a1 and Fn, were upregulated according to PLSDA. Rather than invading the surrounding gel matrix, these cells may have laid down more of their own matrix as a function of being less migratory. Interestingly, Vegfa was also upregulated by early loading. While Vegfa is a necessary component of the sprouting process, it alone is not sufficient to induce sprouting; the balance of other factors, especially angiopoietins 1 and 2, is also a key determinant of whether angiogenesis will occur [279]. The increase in Vegfa may be a compensatory response of MVF pushed into a more quiescent state by early loading. Alternatively, there is evidence that endothelial cells can produce an anti-angiogenic isoform of Vegfa [280]. The two genes most strongly upregulated in response to early loading are Ctgf and Cyr61, which are both canonical targets of the YAP mechanotransduction pathway [276].

In response to delayed loading, the strongest contributor to the gene expression profile represented by PLSDA was the upregulation of Flt1 or Vegfr1. By increasing expression of Vegfr1, delayed loading may increase the sensitivity of MVF to pro-angiogenic Vegf signaling. This may be in contrast with early loading, in which Vegfa upregulation was not accompanied by Vegfr1 or Vegfr2 upregulation. Also in contrast with early loading, delayed loading led to strong upregulation of both Cxcr4 and Timp3 and a more modest upregulation of Mmp14 in the PLSDA gene expression profile. Together, these divergent effects of early vs. delayed loading suggest that tip cell activation may be the mechanism through which loading affects neovascularization. Although Cxcr4 was differentially affected by early vs. delayed loading, its ligand Cxcl12 or Sdf1a was strongly downregulated by both loading scenarios. We initially hypothesized that genes known to be involved in cell recruitment such as Cxcl12 or Sdf1a would be upregulated by delayed

loading. The lack of bidirectional signaling between the nascent vessel and free cells, which are absent in this culture model, may decrease cell recruitment signaling of MVF. Additionally, while these genes are known to be involved in cell recruitment, they also play other roles that may be larger in this context. Bcl2, Bax, and Tnf were all negative contributors to the delayed loading LV2. However, the ratio of pro-apoptotic Bax and anti-apoptotic Bcl2 [281] was not significantly different, which is supported by the live/dead stain. Tnf was also a negative contributor to the early loading LV2, suggesting it is not a mediator of differential mechanical effects. Mmp2 and Mmp9 were also negative contributors to both delayed and early loading LV2. Although they are implicated in angiogenesis [31, 32], neovessel-specific Mmp14 [30, 33] may play a more critical role in our model of microvascular sprouting.

Itgb1, which is an essential adhesion molecule for angiogenesis [282], was upregulated by delayed loading. When looking at the overall gene expression profile of delayed loaded MVF, all eight vascularization-associated adhesion molecules included in our array were upregulated. Interestingly, the one molecule that was differentially expressed by delayed compression vs. compression+shear samples was also an integrin, Itga2. The a2 and b1 integrin subunits form a complex that can bind both collagen [283] and decorin [284], the two components of our gel matrices. In our system, integrins a2b1 may couple cells to the mechanically dynamic matrix and thus act as an element of the mechanotrasduction pathway. In delayed loaded samples as in early loaded samples, two of the most strongly upregulated genes were canonical YAP targets Cyr61 and Ctgf.

To more deeply investigate the potential involvement of YAP/TAZ in the neovascular response to compressive loading, we employed a pharmacological YAP

inhibitor, verteporfin (VP). VP prevents the binding of YAP to the rest of the transcriptional complex, thus suppressing YAP activity [275]. Interestingly, we did not observe the same significant upregulation of Cyr61 and Ctgf due to early loading in the VP experiment as in the initial gene expression array. There was a statistically significant overall upregulation of Ctgf in response to early loading, suggesting YAP may also be involved in the early response, but there was no effect of VP on early expression of either Ctgf or Cyr61. These samples contained DMSO to appropriately control for the delivery of VP within DMSO, and DMSO may have altered the baseline response of MVF to early loading. However, VP abrogated the upregulation of both Cyr61 and Ctgf due to delayed loading, implicating YAP signaling in the stimulatory effect of delayed loading. Together, these results suggest that delayed loading activates YAP signaling, perhaps through integrins, which stimulates the upregulation of genes associated with active tip cells, leading to enhanced vascularization. Ctgf and Cyr61 themselves have been shown to increase endothelial cell proliferation, promote cell adhesion, and modulate the expression of MMPs and TIMPs [285]. Future work is required to more precisely investigate the molecular mechanisms at play and why only delayed loading potentiates a beneficial effect on microvascular growth in vitro.

7.5 Conclusions

Mechanics influence tissue regeneration, and although vasculature is known to be mechanically sensitive, this is the first known in vitro study of the effects of compressive loading on nascent vascular networks. We demonstrated that delayed loading increases

vessel network length and branching compared to early loading at all three strain magnitudes tested (5%, 10%, and 30%). The stimulatory effects of delayed loading were potentiated by loading in gels with a smaller diameter platen designed to introduce compression+shear, which was contrary to our hypothesis. Delayed 5%, 10%, and 30% compression+shear increased length and branching above that of non-loaded controls, and early 30% strain, both compression+shear and compression only, diminished network formation. The morphological differences created by early vs. delayed 30% compression+shear were supported by differential effects on cell proliferation. Using a high-throughput array, we identified gene expression profiles associated with early and delayed loading. Genes associated with active tip cells were downregulated by early loading but upregulated by delayed loading. Delayed loading also led to the upregulation of genes involved in cell adhesion and migration. Both early and delayed loading increased the expression of canonical YAP targets Cyr61 and Ctgf, and this effect was abrogated in delayed loading by YAP inhibitor verteporfin (VP). Overall, this work motivates future investigation of delayed mechanical loading as a component of tissue engineering or physical rehabilitation strategies to enhance revascularization following injury as a means of enhancing tissue regeneration.

CHAPTER 8. CONCLUSIONS AND FUTURE DIRECTIONS

8.1 Overall Conclusions

Overall, this thesis has investigated adipose-derived vascular cell sources as bone therapeutics, developed and characterized a novel biomaterial for in vitro and in vivo applications, and increased fundamental knowledge about the effects of abluminal compressive loading on neovascularization. These results can be leveraged to more effectively treat challenging bone injuries, through informing both future tissue engineering strategies and physical rehabilitation regimens.

8.1.1 Specific Aim 1: Evaluate effect of vascular cell source co-delivered with BMP-2 to composite defect model

In Chapter 3, we characterized collagen sponge, a clinically available BMP-2 carrier, as a co-delivery vehicle for both BMP-2 and MVF/SVF. Both MVF and SVF maintained viability in collagen sponge for at least 14 days; however, multicellular MVF first dissociated to single cells before reforming networks. This is in contrast with the sprouting angiogenesis MVF exhibit in collagen gel matrices. Interestingly, MVF dissociation in the presence of exogenous BMP-2 appeared to trigger an increased recovery of BMP-2, both on collagen sponge and on TCPS. The increased BMP-2 recovery was not due to MVF producing additional BMP-2 or increased protease activity. MVF may bind exogenous BMP-2 that is subsequently released upon dissociation. A pilot in vivo experiment was performed to evaluate the effects of MVF+BMP-2, SVF+BMP-2, and

BMP-2 alone delivered by collagen sponge on bone healing with concomitant muscle damage. This pilot study suggested that co-delivering MVF, but not SVF, may increase regenerate bone mechanical properties compared to BMP-2 alone.

In Chapter 4, we conducted a fully powered in vivo study comparing the effects of MVF and an increased dose of BMP-2 on bone healing in a composite bone-muscle defect model. Consistent with our hypothesis, a modestly increased 10 μg dose of BMP-2 improved bone healing relative to a minimally bridging 2.5 μg dose. However, contrary to our hypothesis, MVF did not improve healing and in fact significantly decreased regenerate bone stiffness. Although dissociation of MVF within collagen sponge augmented BMP-2 recovery in vitro, we speculated that MVF dissociation in vivo did not recapitulate this phenomenon and instead likely led to cell death before vascular networks could reform and anastomose with host vasculature. This motivated the development of an alternative biomaterial delivery vehicle.

8.1.2 Specific Aim 2: Develop a biomaterial for in vitro studies and in vivo delivery of microvascular fragments.

MVF are typically cultured in low percentage collagen gels; however, these are not suitable for in vivo MVF delivery. Collagen gels allow robust in vitro network formation, but as the networks grow and exert increasing traction forces on the matrix, the collagen gel will eventually contract and collapse the vascular network within. Thus, dimensional stability was a key design criterion for both in vivo MVF delivery and extended in vitro culture. Additionally, collagen gels exhibit a burst BMP-2 release that is not favorable for

bone regeneration. In Chapter 5, we developed and characterized DCN-supplemented collagen hydrogels as in vitro MVF culture substrates. The addition of DCN increased gel compressive properties and achieved improved dimensional stability without compromising MVF growth. In Chapter 6, we also demonstrated that collagen+DCN gels exhibit a more sustained release of BMP-2 than collagen alone and evaluated collagen+DCN as an in vivo co-delivery vehicle for BMP-2 and MVF. Despite in vitro results showing synergistic effects of BMP-2 and MVF, there was no effect of MVF on bone healing, and MVF significantly decreased early revascularization following injury. Together, Chapters 4 and 6 suggest that freshly isolated, adipose-derived MVF are not viable segmental bone defect therapeutics. However, collagen+DCN gel is a dimensionally stable culture substrate for long-term MVF culture that withstands compressive loading.

8.1.3 Specific Aim 3: Investigate effects of mechanical loading on microvascular growth and remodeling.

In Chapter 7, we utilized MVF as an in vitro model system to study the effects of compressive loading on neovascularization. MVF represent a 3D culture system that allows for cell-cell and cell-matrix interactions, thereby better representing physiologic conditions than traditional 2D monolayer approaches. Although vasculature is a vital component of nearly all tissues and reestablishment of a functional vascular network is required for wound healing to proceed, remarkably little is known about the effects of abluminal forces on vascular growth. We used MVF as a platform to investigate the effects of dynamic compressive strain magnitude, mode, and time of initiation. We demonstrated that delayed

loading led to longer, more extensively branched microvascular networks than early loading at all strain magnitudes tested, and contrary to our hypothesis, the stimulatory effects of delayed loading were potentiated by loading in gels with a smaller diameter platen designed to introduce compression+shear. Early loading exhibited strain magnitude-dependence, and 30% strain, both compression+shear and compression only, inhibited network formation. Gene expression analysis revealed differential mechanoregulation of gene expression profiles by early vs. delayed loading. Interestingly, some of the same genes were differentially affected by early vs. delayed loading; genes associated with active tip cells were downregulated by early loading but upregulated by delayed loading. Delayed loading also led to the upregulation of genes involved in cell adhesion and migration. Both early and delayed loading increased the expression of two canonical YAP targets, Cyr61 and Ctgf, and this effect was abrogated in delayed loading by YAP inhibitor verteporfin (VP), demonstrating YAP's involvement in the pro-angiogenic response to delayed loading.

8.2 Future Directions

8.2.1 MVF and SVF as Therapeutics for Bone

In Chapters 3-4, we investigated MVF and SVF as therapeutics for bone regeneration. Intriguing in vitro BMP-2 recovery results that demonstrated augmented BMP-2 recovery from MVF-containing collagen sponges and promising results of a pilot in vivo experiment led us to focus on MVF; however, SVF have been used clinically as not only a vascular cell source but also a source of osteoprogenitor cells [123]. The MVF dose

used in the studies presented in this thesis was determined by a pilot study, and the SVF dose used was chosen to deliver approximately the same number of cells as the MVF dose. By more rigorously studying both the dose of SVF and its osteogenic potential, SVF may prove to be an attractive therapeutic for segmental bone defects with concomitant muscle damage.

After completion of Chapters 3-4, we speculated that the collagen sponge delivery vehicle promoted MVF dissociation that prevented a beneficial healing response. MVF decreased regenerate bone stiffness, and, while not statistically significant, tended to decrease the absolute value of bone volume as well. After using a different biomaterial delivery system that was specifically tailored to the co-delivery of BMP-2 and MVF, we still observed no beneficial effect of MVF on bone healing in the composite defect model and observed a decrease in vascularization. Additionally, while the implanted GFP+ MVF were identifiable by immunohistochemistry at seven days post-surgery, they appeared as single cells, which we did not observe in collagen+DCN in vitro, and did not appear to be associated with vascular structures.

We harvested MVF from retired breeder rats, which are by definition older. Other groups have reported more robust network formation with MVF from young donor rats [220], perhaps due to increased abundance or potency of progenitor cells, which may improve outcomes. Previous work in our lab that has shown an increased vascular volume with MVF treatment used MVF that were cultured in vitro for four days prior to implantation [116], allowing a provisional network to form. Pre-culturing MVF, which has been shown to accelerate inosculation with the host vasculature [115], may improve their success in large volumetric defects such as segmental bone defects. Future studies may

investigate the delivery of MVF pre-cultured in collagen+DCN gels. However, co-delivery of a consistent BMP-2 dose is a challenge in pre-cultured constructs. Development of a biomaterial capable of stimulus-responsive release of BMP-2 or a strategy to load BMP-2 into existing gels could be investigated. Since we see a negative effect of MVF treatment rather than simply no effect at all, MVF are likely disrupting some part of the endogenous healing process. Adipose-derived MSCs, which MVF do contain (see Figure 3.1), have previously been shown to diminish BMP-2-mediated bone formation [67]. Although adipose-derived MVF have potential for autologous transplantation, MVF isolated from tissue-specific sources (e.g. bone marrow) may prove more successful in bone.

8.2.2 Increased BMP-2 Dose to Treat Bone Injuries with Concomitant Muscle Damage

Although MVF did not improve bone healing with concomitant muscle damage, a modestly increased 10 μg dose of BMP-2 did improve healing compared to a minimally bridging 2.5 μg dose. Although extremely high BMP-2 doses have been linked to a number of adverse effects including heterotopic ossification and an increased inflammatory response [73], we did not observe any mineralization outside the defect area, and levels of both pro- and anti-inflammatory cytokines were lower in the higher BMP-2 dose group. A modestly increased BMP-2 dose may be able to overcome the attenuated bone healing observed with concomitant muscle damage, but future studies to precisely determine species-specific dosing are required.

The mechanisms by which BMP-2 can begin to overcome the bone healing deficit also warrant investigation. The inflammatory stage of wound healing has been shown to

be prolonged in composite defects [40], and future studies investigating inflammatory profiles at earlier time points would be required to more definitively address the composite injury's inflammatory response to various BMP doses. The composite defect model used here exhibits both attenuated bone healing and altered revascularization; BMP-2 can indirectly promote angiogenesis [286], which may be a factor. Increased dose of BMP-2 may also simply amplify the cell recruitment and differentiation signaling it is known to stimulate [59].

While clinically available, collagen sponge exhibits a burst release of BMP-2 [242], which necessitates the usage of supraphysiological doses that have led to adverse effects [73]. We conducted a pilot composite defect study where we delivered both 2.5 μg and 10 μg of BMP-2 in collagen+DCN gels (Figure 8.1). Similar to the dose differences observed when delivered on an acellular collagen sponge, we saw an approximate two-fold increase in failure strength with increased dose. In contrast with the acellular collagen sponge delivery vehicle, we also observed a nearly 30% increase in bone volume with increased BMP-2 dose delivered in acellular collagen+DCN gels. Again, we did not observe mineralization outside the defect area. These data both provide additional support for the use of a moderately increased BMP-2 dose in composite injuries and demonstrate that collagen+DCN is a capable BMP-2 delivery vehicle, even at moderately increased doses. Future work may include fully powered studies using collagen+DCN gels as delivery vehicles for higher dose BMP-2.

Ongoing work is also investigating the use of heparin microparticles to delivery higher dose BMP-2 (e.g. 30 μg) to composite defects. Heparin sequesters positively charged growth factors including BMP-2 and thus allows for a much more controlled,

sustained release of BMP-2 [287]. Defect bone volume, heterotopic bone volume, and the inflammatory response should all be considered in the optimization of BMP-2 dose and delivery vehicle.

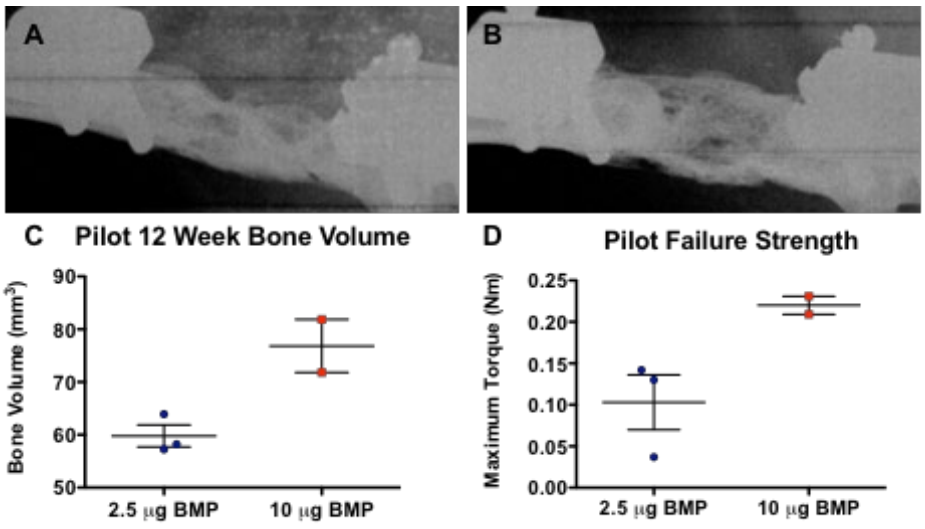

Figure 8.1. Pilot study deliverying 2.5 µg and 10 µg of BMP-2 to composite defect model in collagen+DCN gels. 12-week radiographs of A) 2.5 µg and B) 10 µg BMP-2-treated defects. Relative to 2.5 µg BMP-2, 10 µg BMP-2 tended to increase both C) bone volume and D) failure strength.

8.2.3 Mechanical Regulation of MVF Growth

The in vitro loading setup used in Chapter 7 presents a rich platform for future work, as nearly every parameter could be varied: frequency, strain magnitude, initiation time of loading, duration of loading, and platen design. We consistently used a 1 Hz frequency for all studies. In bone, high frequencies have been shown to potentiate the

response of smaller magnitude strains [151, 152]. Therefore, the effects of high frequency, low magnitude loading on microvascular growth may be of particular interest. Additionally, preliminary data suggests that the frequency parameter is important to the stimulatory effect of loading. At 30% strain, delayed static loading (e.g. frequency of 0 Hz) increased network length and branching relative to early loading but had no effect relative to the non-loaded control.

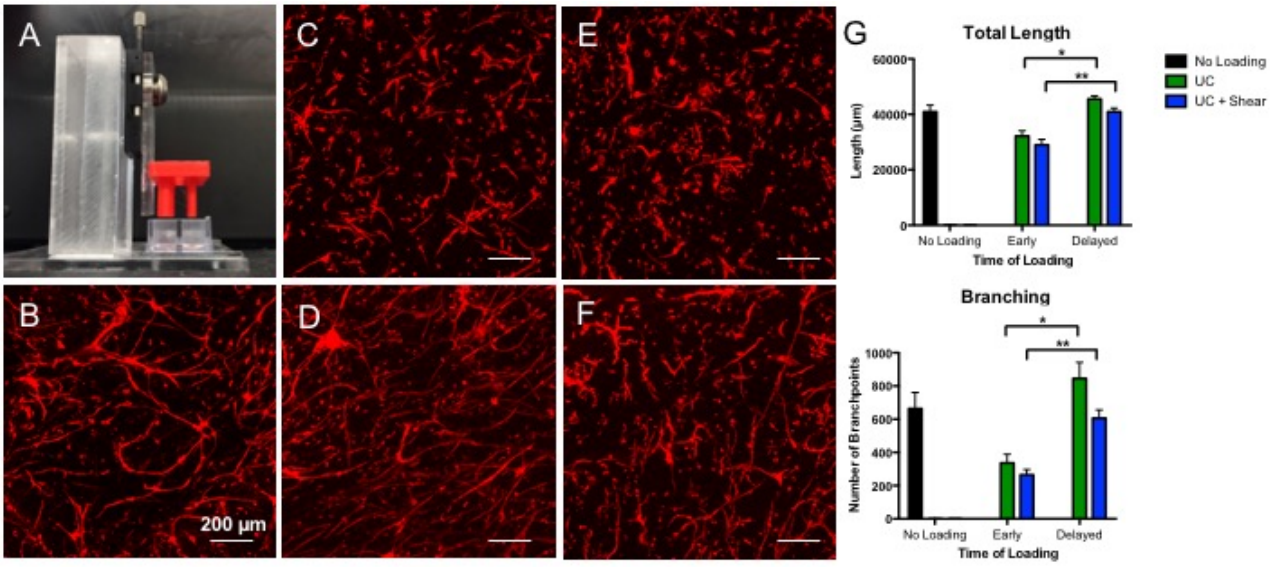

Figure 8.2. Preliminary Static Loading Data. A) Static compression device; the larger diameter platen pegs (left) create unconfined compression (UC), while the smaller diameter pegs (right) create UC with a shear interface zone. Representative day 10 images of B) non-loaded, C) early UC, D) delayed UC, E) early UC+shear, and F) delayed UC+shear. G) Quantification of microvascular network length and branching under static unconfined compression, with or without a shear interface zone, vs. unloaded controls; quantification performed on thresholded maximum intensity z-projections using Fiji AngioAnalyzer plugin; two-way ANOVA, n=4/group; * indicates $p<0.05$, ** $p<0.01$.

Looking at delayed 5%, 10%, and 30% compression only, we observed a significant beneficial effect of 5% strain, no significant increase but higher absolute value at 10%

strain, and no effect at 30% strain, suggesting there is an optimal strain for increasing vascular growth. By investigating additional strain magnitudes, particularly those between 10-30%, this peak may be more precisely identified. Similarly, early loading was inhibitory at 30% strain but not at 5% or 10% strain; the strain threshold at which early loading becomes disruptive could also be more precisely identified by testing strains between 10-30%. To more precisely define what critical step must occur or level of vascular maturity must be achieved for networks to be permissive to loading, loading could be initiated at different time points, particularly those between days 0-5. An interesting experimental group is early loading that is applied continuously throughout the 10 day culture. We chose not to include that group to keep the overall duration of loading consistent between early and delayed loading, but it may provide valuable insights into whether early loading completely impedes or simply delays angiogenesis. Another interesting variation would be to introduce rest periods within loading, e.g. load for 12 hours and rest for 12 hours. This may better mimic physiologic loading due to normal activity, and bone can be effectively restimulated by loading after a rest period as brief as 14 seconds [155, 156].

Contrary to our hypothesis, we saw that compression+shear loading led to increased vascular length and branching at 10% and 30% loading. While we designed the compression+shear platens to introduce a shear interface zone, no interface was visually apparent in the resulting vessel networks, and there was no difference in the spatial distribution of vessels. Ongoing computational work in collaboration with Jeff Weiss's group at the University of Utah led by Steven LaBelle suggests that the compression+shear platens create shear only at the very superficial surface of the gel but do profoundly change the fluid flow patterns into and out of the gel (Figure 8.3). These compression+shear

platens also change the bulk stress experienced by the gel and the local stress and strain gradients, which computational modeling in the Weiss group will help to define. Different platen designs could be optimized with the aid of computational modeling to answer specific questions about the roles of shear, bulk stress vs. strain, and local stress and strain gradients. Computational data may also be useful in narrowing the wide parameter space discussed above.

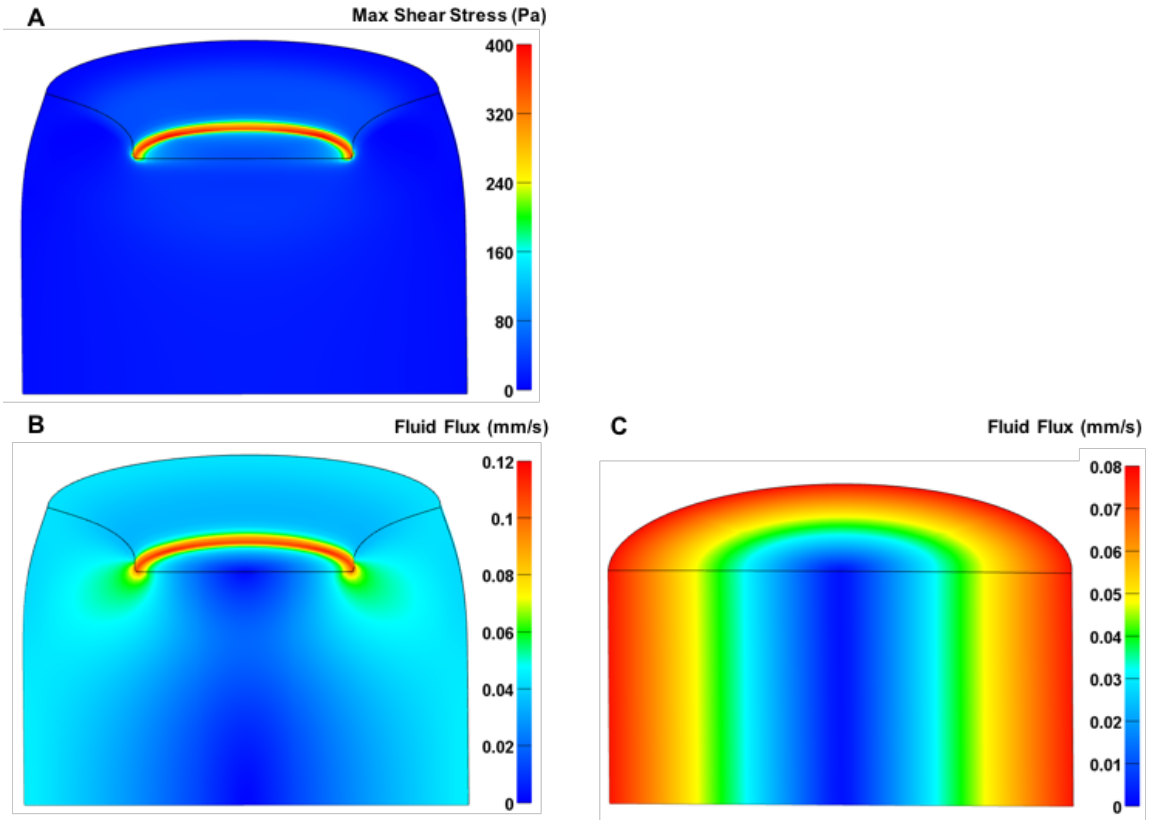

Figure 8.3. Preliminary computational modeling results of loading 3% collagen+DCN gels. A) Maximum shear stress experienced by collagen+DCN gels to 30% strain in compression+shear loading configuration. Fluid flux profiles due to 30% strain in B) compression+shear and C) compression only. *(Figures provided by Steven LaBelle.)*

Within the parameters we did investigate, it would be interesting to assess expression of the same genes probed at 30% strain at 5% and 10% strain. The gene expression profiles leading to a beneficial effect of loading may be similar regardless of strain magnitude (i.e. they achieve the same net effects), or they may differ, suggesting that different strains modulate vascular growth through differing mechanisms. The expression of YAP targets upregulated by 30% strain, Cyr61 and Ctgf, would be of particular interest at lower strains. Early compression+shear loading was not significantly different than the non-loaded group, but the absolute value of length and branching were higher. Exploring gene expression at 10% compression+shear could elucidate whether early loading can have a beneficial effect at the proper parameters.

The involvement of YAP in the response to loading warrants further investigation. Although we initially saw strong upregulation of YAP targets Cyr61 and Ctgf in response to both early and delayed loading, we only saw their strong upregulation in response to delayed loading in the YAP inhibitor study. However, VP did abrogate the upregulation of these genes due to delayed loading, demonstrating that YAP signaling is indeed involved in the response of microvasculature to delayed loading. There was a statistically significant overall upregulation of Ctgf in response to early loading, suggesting YAP may also be involved in the early response, but there was no effect of VP on early expression of either Ctgf or Cyr61. It would be interesting to examine the expression of other genes strongly affected by loading when YAP signaling is inhibited. We made an effort to investigate this, but the inclusion of DMSO appeared to starkly alter the overall baseline gene expression profiles of MVF, both loaded and non-loaded. VP itself also had baseline effects on non-loaded constructs, which is not as surprising; VP inhibits YAP binding to the TEAD

transcriptional complex but also has a number of other effects and is used clinically in combination with photostimulation to ablate endothelial cells [288]. Titrating the concentration of DMSO and precise dose of VP may help alleviate this technical issue, but these questions may have to a wait until a more specific inhibitor of YAP activity is developed. In the meantime, immunohistochemistry can be used to begin investigating the integrins such as Itgb1 that may also play a role in YAP-mediated mechanotransduction. Investigating cytoskeletal effects of loading may also provide insight into the mechanotransduction pathway at play. Ultimately, conventional pathway identification techniques (e.g. kinase inhibitors and western blotting to examine protein phosphorylation) could be used to precisely identify the signaling cascade that generates a microvascular response to dynamic compressive loading.

One advantage of using MVF as a model system is that they are composed of multiple cell types characteristic of mature vasculature. However, this is also a limitation in identifying cell type specific responses to loading. The immunohistochemistry performed in Chapter 7 suggests that the relative abundance of the two most prevalent cell types, SMCs and ECs, does not substantially change over time or in response to loading. However, flow cytometry would be a more precise method of assessing this, and there are additional cell types that could be investigated, including macrophages, which are known to be components of MVF (unpublished data, Jay Hoying; macrophages also comprise around 20% of related adipose-derived SVF [120]) and to play a role in angiogenesis [30, 289]. To begin to understand cell type specific responses to loading, single cell RNA sequencing could be employed.

Once the vascular cell-specific responses are characterized, utilizing a co-culture of MVF with osteoblasts, osteocytes, myoblasts, etc. may provide more tissue-specific insights into the effects of loading on microvascular growth in a more physiologically relevant context. The addition of soluble signals thought to be more tissue-specific (e.g. BMP-2) may be another way to begin to understand inter-tissue crosstalk. MVF cultured in collagen+DCN gels hold great potential as microphysiologic systems that could be used to understand the effects of mechanical cues and chemical cues and could be utilized as a drug screening platform, especially for drugs intended to target pathways convergent with mechanotransduction pathways.

The effects of abluminal compressive loading on neovascularization gained here can begin to inform clinical practice. In particular, the benefits of delayed loading here may inform guidance on how soon patients can and, in fact, should resume load-bearing activities. In combination with well-characterized fixation strategies that apply strain of a known, favorable magnitude, enhanced bone healing may follow enhanced angiogenesis. More broadly, the fundamental understanding of how abluminal compressive forces regulate microvascular growth is relevant to all vascularized tissues and motivates further study of additional abluminal forces.

APPENDIX A. PROTOCOLS

A.1 Microvascular Fragment (MVF) Isolation

Materials

- HBSS + 5% FBS, need about 250ml per isolation
- 1X PBS with Ca and Mg
- Collagenase Type I (Worthington Biochemical)
- DNase (Sigma 11284932001)
- Bovine serum albumin (BSA; Sigma A3294)
- 0.22 um sterile filters (e.g. Steriflip, Millipore SCGP00525)
- Small (50 -125 mL) autoclavable plastic Erlenmeyer flask
- Small Teflon stir bar
- Large aperture steel mesh (McMaster 9322T65)
- 20 μm nylon filter sheet (Small Parts CMN-0020-D)
- 200-500 μm nylon filter sheet (Small Parts B0043D1TVO or CMN-0500-C)
- 50 mL conical tube – sterile
- 15 mL conical tubes – sterile
- Serological pipettes (5 mL, 10 mL, 25 mL)
- Wide bore pipette tips (e.g. Thermo 2079G and 2069G)
- Petri dish (non-TC treated) – sterile
- Curved hemostats (1) – sterile
- Large scissors (2) – sterile
- Small scissors (1) – sterile
- Forceps (2) – sterile
- Male rats – retired breeders as large as possible
- Alcohol-soaked gauze
- Collagen gel solution (see A.2 Collagen ± Decorin Gel Protocol)

Digestion solution

- **Collagenase Type 1** (Clostridial collagenase, Worthington Biochemicals, USA)
    - Lot tested by empirical microvascular yield and quality assessment and in vitro culture testing. Lots SM2P13900 and 45N16191 have worked well.
- Total volume of digestion solution is 1.5 times the fat volume in mL PBS.
- Add 7.5x fat volume of BSA in mg.
- Add 3.5x fat volume of collagenase in mg
- Add 2x fat volume of DNase in mg.
- Mix to dissolve and sterile filter. Prepare right before use. Must be at room temperature when added to fat.
- Example calculation:
  Have 15 mL fat. Use 22.5 mL PBS to dissolve 52.5 mg collagenase, 30 mg DNase, and 112.5 mg BSA.

Methods

Fat Isolation

1. After anesthetizing the animal with isoflurane, lay the animal down in the supine position. Put pressure on the middle of the abdomen area with 2 fingers and wipe animal well with alcohol-soaked gauze – pelvic area first, then feet.
2. Grip animal with hemostats on the skin directly at the base of the penis.
3. Cut the skin below the hemostat with large scissors to expose the testes. Gently draw out the epididymal fat and vessels using forceps and harvest the fat only using small scissors without cutting the large testicular vessels or the epididymal head/tail.
4. Expose the animal's thorax with large scissors and induce a hemo-pneumothorax to euthanize the animal.
5. Harvest the fat and place it in a tube with a known volume of FBS-HBSS (e.g. 20 mL) to measure the fat volume and calculate the appropriate material amounts for the digestion solution.
6. Transfer fat to non-TC treated Petri dish with new, sterile forceps.

7. Manually mince the fat pads using new, sterile large scissors for about 7 minutes to get a homogenous mix that can be drawn up into a 10 mL pipette.
8. Mix the digestion solution with the minced adipose tissue using a 10 mL serological pipette and transfer to small Erlenmeyer flask with a small Teflon stir bar and digest in a 37^{o}C water bath with agitation (shaking water bath or manually shaking vigorously for 7 – 8 minutes).
9. Stop the digestion by adding FBS-HBSS to the digestion solution (at least 1:1 volume).
10. Transfer the digestion solution into 50 mL conical tubes and spin in a clinical centrifuge at 4000 rpm for 4 minutes.
11. Aspirate the supernatant and wash the pellet in further FBS-HBSS, breaking the pellet and re-suspending it in this new wash buffer. Transfer the solution to 15 mL tubes.
12. Spin again at 3000rpm for 3 mins. Repeat this wash step once more.
13. After the above wash, re-suspend the pellet in FBS-HBSS and filter first through a 200-500 μm nylon membrane. Discard the membrane and retain the flowthrough.
14. Filter the flow through a 20 μm filter, supported on a large aperture steel grid, and discard the flow-through.
15. Wash the 20 μm membrane and collect the microvessel fragments retained on top of it. Wash the mesh with 40 – 50 ml of BSA-PBS and collect the solution (10 mL at a time in a petri dish). Count a representative volume (3 drops of 20 μL drawn out into straight lines) from a well-mixed suspension.
16. Pellet the microvessel fragments (3000 rpm for 3 minutes, clinical centrifuge), re-suspend the pellet in about 50 μL of BSA-PBS using a wide-bore pipette tip.
17. Make adequate collagen solution to suspend the fragments at 20,000 fragments/mL of solution. Incubate for 20 – 45 minutes to allow gelation.
18. Cover with serum-free media (1:1 DMEM:F12 base with insulin, transferrin, μnutrients, and VEGF) culture in a humidified incubator at 37 °C with 5% CO_2.
19. Change media on Day 3-4 and every other day thereafter. Angiogenic sprouts should be visible by day 3- 4, and a network of microvessels should be visible within 7 -10 days.

A.2 Collagen ± Decorin Gel Protocol

Materials

- **Fresh** 4X DMEM (Thermo Fisher 31600-026 or -034)
    - 0.37 g HEPES + 0.476 g $NaHCO_3$ per 1 g DMEM powder into 25 mL dH_2O
    - Only need to make ~0.25 g DMEM at a time
    - Use within ~2-3 weeks
    - Sterile filter for use with cells
- Rat tail type I collagen (Corning 354249)
- Deionized water, sterile filtered for use with cells
- Purified decorin (DCN), if using
- ≥1 M NaOH
- 0.22 μm sterile filters for use with cells (e.g. Steriflip, Millipore SCGP00525)
- 50 mL conical tubes
- Wide bore pipette tips (e.g. Thermo 2079G)

Methods

1. Gather all solutions and keep on ice!!!!
2. Calculate amounts needed. Final concentration is typically 3 mg/mL collagen (can be adjusted to achieve different gel stiffness) in 1X DMEM. Make about 0.5-1 mL more collagen than needed due to losses in preparation.
    a. Example calculation:
    Want 1 mL collagen gel total. Need:
    (3 mg/mL)(1 mL)/(9 mg/mL stock) = 0.333 mL collagen stock @ 9 mg/mL
    1 mL/4 = 0.25 mL 4X DMEM
    1 mL – (0.333 mL coll. + 0.25 mL DMEM) = 0.417 mL dH_2O
        i. If using DCN, incorporate at 50 μg/mL. Subtract DCN volume from dH_2O volume added.

3. Add 4X DMEM, collagen stock, and dH_2O into a 50 mL conical, even if making a small volume, and swirl tube to mix. Pipette collagen stock with wide bore tip (or serological pipette for larger volumes).
4. Adjust pH with NaOH as necessary. Yellow/orange is too acidic, but purple is too basic. Try to keep at the color of fresh 1X DMEM: bright light red with a tint of pink.
5. If using decorin, add it *after* adjusting pH. Swirl tube to mix.
6. Resuspend cells with collagen solution at this point if desired. Use wide bore pipette tip and pipette up and down then gently swirl tube to mix.
7. Pipette into well plate, mold, etc. using wide bore pipette tips. Incubate at 37 °C for 20-30 minutes to allow gelation.

A.3 Serum-Free Media for Microvessel Fragments

Prepare aliquots based on 50 mL media prep at a time and store at -20 °C:

1. Transferrin (Sigma T-2252) – Aliquot 0.5 mL of 10 mg/mL in media.
2. Insulin (Sigma I-5500) – Aliquot 0.5 mL at 1 mg/mL in media; can use small volume of 1 N HCl to increase solubility if necessary.
3. Micronutrients – Aliquot 1 mL each with:
    a. 1 µM Progesterone (Sigma P7556)
    b. 5 mM Putrescine (Sigma P7505)
    c. 1.5 µM Sodium selenite (Sigma 55261)
    d. 5 mg/mL Bovine serum albumin (BSA; Sigma A3294)
    e. Resuspend components a-d at known concentration based on amount weighed out. Dilute in media to achieve above concentrations. Add BSA, which can be much more reliably weighed to a specific mass, last.
4. rhVEGF (R&D Systems 293-VE; MVF will grow without, but this accelerates) – Aliquot 5 µL at 100 µg/mL.

For 50 mL of media (50% DMEM + 50% F-12; VWR 10-103-CV), add 1 aliquot each of transferrin, insulin, micronutrients, and rhVEGF. Sterile filter.

Final concentrations in 50% DMEM + 50% F-12 should be:
Transferrin: 100 µg/ml
Insulin: 10 µg/ml
VEGF: 10 ng/mL
Progesterone: 20 nM
Putrescine: 100 µM
Sodium Selenite: 30 nM
BSA: 100 µg/ml

A.4 Rat Vascular Perfusion

Materials:

- 0.9% normal saline
- 0.4% papaverine hydrochloride in 0.9% normal saline
- 10% neutral buffered formalin
- 1 pair small surgical scissors, 1 pair large scissors, 2 hemostats, 1 small curved pair of forceps, additional instruments by personal preference
- 18 gauge 2" long catheter
- needles
- peristaltic pump
- peristaltic pump tubing (Cole-Parmer Masterflex 96410-16)
- small tubing for connecting pump tubing to catheter (Cole-Parmer 95802-02)
- male and female luer lock connectors as needed
- diaper pads
- gauze and cotton swabs
- 2-0 needle-less suture
- Safety goggles
- Lab coat
- CaviWipes
- 50 mL conicals
- 20 mL syringes
- Contrast agent solutions (current preferred contrast solution is Microfil MV-122 – www.flowtech-inc.com – yellow colored lead chromate compound) – includes Microfil compound, diluent, and catalyst

Procedure:

Prepare solutions I

- 0.4% papaverine hydrochloride in 0.9% normal saline
- 0.9% normal saline (~200 mL/rat)

9 g sodium chloride

1000 mL DI water

- 10% neutral buffered formalin (~150 mL/rat)

Perfusion I – Saline (to clear blood), Papaverine (to dilate vessels), and Formalin (to perfusion fix vessels)

1. Within chemical fume hood, set up the peristaltic pump, check the flow, and bleed all air out of the line using the saline solution. You may have to start flow by siphoning the saline through the tubing using a syringe.
2. Euthanize animal or induce anesthesia at 5% isoflurane in an induction chamber.
    a. If anesthetized switch animal over to the face mask at 2% isoflurane.
    b. Check for pedal withdrawal reflex using the toe pinch. When this reflex is not observed, the animal has reached a deep surgical plane and the procedure can begin.
3. Using needles, pin animals hands and feet to Styrofoam. Legs should be as straight as possible.
4. Using scissors, cut transversely through the skin & muscles just below the xyphoid process of the rib cage to expose the diaphragm.
5. Gently cut the diaphragm, taking care not to puncture the heart or underlying vessels.
6. Cut through the rib cage to allow opening of the chest cavity. A large hemostat can be used to help keep the chest cavity open by clamping to xyphoid and positioning the instrument as necessary.
7. Carefully dissect the heart free of the connective tissue holding it to the rib cage.
8. Using small blunt tip forceps, pass a piece of 2-0 suture behind the aorta.
9. While the heart is still pumping, insert the 18g catheter into the left ventricle (apex of the heart). Blood should begin to back out of the catheter.
10. Carefully advance the soft catheter end up into the ascending aorta while backing the needle out.
11. Using a single loop with the 2-0 suture, constrict the aorta around the catheter within its lumen to prevent back-flow later in the perfusion process.

12. Transfer the animal pinned to Styrofoam to a metal rack placed on top of a plastic collection tub within chemical fume hood.
13. Attach the connection tubing to the catheter, making sure to minimize any air in the tubing.
14. Cut the inferior vena cava and the external muscle wall to allow fluids to drain.
15. Immediately, turn on the pump, pefusing with saline ~50 mL
    a. Perfusion volume is an estimate. The goal is to perfuse until vessels are clear. The liver should blanch quite quickly. Kidneys can be inspected to evaluate perfusion also. Average rat blood volume is 25 mL.
    b. Note: stop pump when switching solutions to avoid air bubbles in the perfusion tubing.
16. Perfuse with 0.4% papaverine ~50 mL to dilate vessels.
17. Perfuse with saline ~50 mL to flush out papaverine. If papaverine and NBF come into contact, the papaverine will precipitate out!
18. Perfuse with 10% NBF ~100 mL. Again, perfusion volume is an estimate. The goal is to perfuse until the extremities are fully fixed. Inflation of the lungs is an indicator of backflow in the system. After ~100 ml, one may observe muscle twitching and/or relative inflation of the GI system, which is not abnormal.
19. Final saline perfusion - reconnect saline to clear formalin, ~25-50 mL

Prepare Solutions II

- Contrast agent solutions (~20 mL/rat)

  Just prior to contrast agent perfusion (during final saline perfusion):

  - In a 50 mL conical, combine:

    20 mL Microfil MV-122

    10 mL diluent (dilution can be up to preference, recommended no more than 1:1, diluent:MV)

    1 mL catalyst
  - Immediately before injection, shake well to mix.
  - Fill 20 mL syringe with catalyzed Microfil, eliminate air bubbles as much as possible

Perfusion II – Microfil Contrast Agent

1. Disconnect perfusion pump tubing from catheter
2. Connect 20 mL syringe with catalyzed Microfil solution to catheter.
3. Carefully inject Microfil into animal, maintaining steady pressure.
    - Caution: Pressurized Microfil may cause ruptures in fixed vessels and may squirt out at high pressure so be sure to perform this step in the fume hood while wearing safety goggles and protective clothing
    - All vessels should yellow, turning the musculature and internal organs including liver, kidneys, etc quite yellow as well
4. Allow Microfil to polymerize at least 2 hrs or overnight at 4 °C before harvesting tissues.
5. Clean any surface that has come in contact with lead-containing Microfil with CaviWipes. Dispose of all Microfil waste in biohazard bag in biohazard box labeled “chemotherapeutic waste”. Dispose of perfusion fluids drained from rat in waste bottle and label appropriately.

A.5 Confocal Imaging for MVF Quantification

I. Power on the system, Zeiss 700 Confocal, and open Zen 2012. After software has loaded click “Start System” and wait for hardware to initialize.

II. System Setup
    A. Click on the Acquisition Mode tab, click “Show all”
        1. Enlarge scan area to max size by pulling the corners
        2. Make sure that Direction is set to →
    B. Click the “Smart Setup” button
        1. Choose rhodamine red and the “Smartest” setup (adjust for other fluorophores)
    C. Set 555 nm laser to 20.0

III. Find Sample
    A. Under Locate menu, choose correct objective lens (5x)
    B. Place circular slide and slide holder (with gel) onto stage
    C. Choose red light and the lower fluorescent lens button
    D. Use joystick and to find gel, then focus on an area
    E. Return to Acquisition Mode and increase gain to visualize sample

IV. Z-Stack
    A. Under Acquisition Mode check the z-stack box
    B. Click “Show all” under the Z-Stack tab
    C. Set up z-stack
        1. Find the bottom of the sample and click “Set First”
        2. Scroll up until the Range reads 200 um by clicking “Set Last”
        3. Set interval to 5 um (within Nyquist sampling range, and creates isotropic voxel size; adjust for different objectives)
    D. Set up Correction
        1. Check the “Use Correction” box
        2. Click the circle with an F in it (the first slice, previously set)
        3. Adjust gain to clear any noise
        4. Click the “Add” button

5. Repeat for the top layer
6. Select “save …” and save the correction file

V. Tile Scan

A. Under Acquisition Mode check the Tile Scan box

B. Click “Show all” under the Tile Scan tab

C. Go to the Convex hull tab

1. Use the joystick to find an edge of the gel (top, bottom, left, or right)
2. Click the “Add” button
3. Find the other three points and add them
4. Find the center by guess and check
5. Once the five points are added, find the midpoint between the center and right side of gel and add it

D. Go to Centered grid tab

1. Exit Live imaging
2. Select 2 horizontal and 1 vertical
3. Uncheck z-stack and click “Run Experiment” to see if the edge is visible in the scan
4. Click “Scan Overview Image” at the bottom of the tab and collect 3 horizontal and one vertical snap. Save.
5. Re-check z-stack and run experiment

VI. Save file in Data drive with appropriate name

VII. Shut Down

A. Close software

B. Remove sample

C. Log off computer

D. If last person for the day, turn off components

A.6 Quantification of MVF Confocal Image Stacks of MVF

I. FEI Amira for Cell Biology:

1. Import stitched .tif stack into Amira and set voxel size to 5 x 5 x 5 um (5X).
2. Image Pre-processing
    a. 3D median filter
        i. Under project view, right click the > on the .tif box and type “median filter” in the search bar
        ii. Under “interpretation”→ 3D (not XY planes)
        iii. Project View sidebar should look like this:

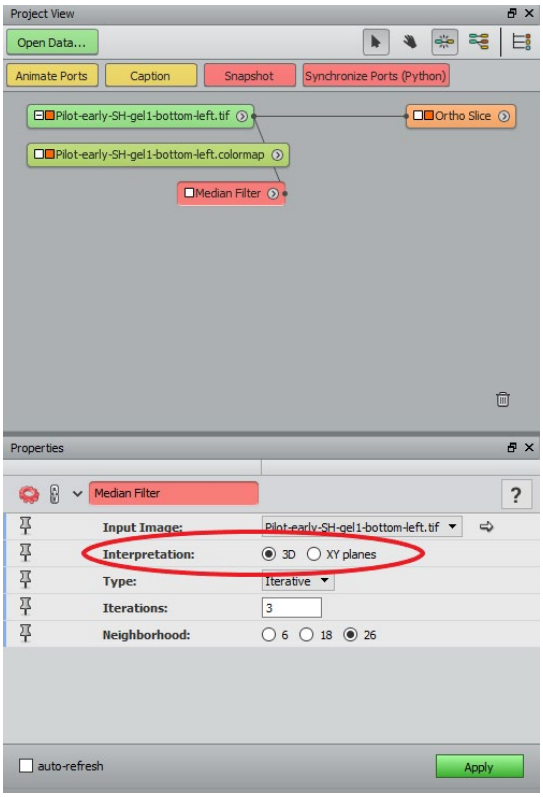

        iv. Click “Apply”

    b. Blind 3D Deconvolution
        i. Click the > of the .filtered box and search for “Deconvolution” (Image processing→ Frequency Domain→ Deconvolution)

ii. Under parameters, set border width to 0,0,0; iterations to 15; initial estimate to input data; overrelaxation to fixed; regularization to none; and method to blind.

iii. Under microscope, set PSF to no source, numerical aperture (NA) = 0.16, wavelength = 0.520 um, refractive index of collagen = 1.35, and mode to confocal.

iv. 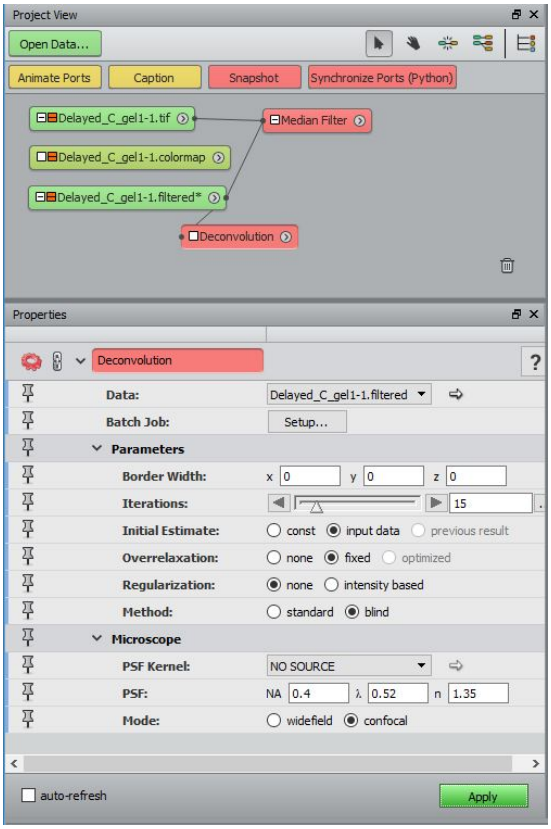

v. Click “Apply”

3. Threshold deconvolved image. Interactive thresholding – change lower bound of Intensity Range to conservatively apply threshold to remove noise while preserving segment connectivity. Verify threshold by visually comparing with raw image; pay special attention to beginning and end slices.

a. 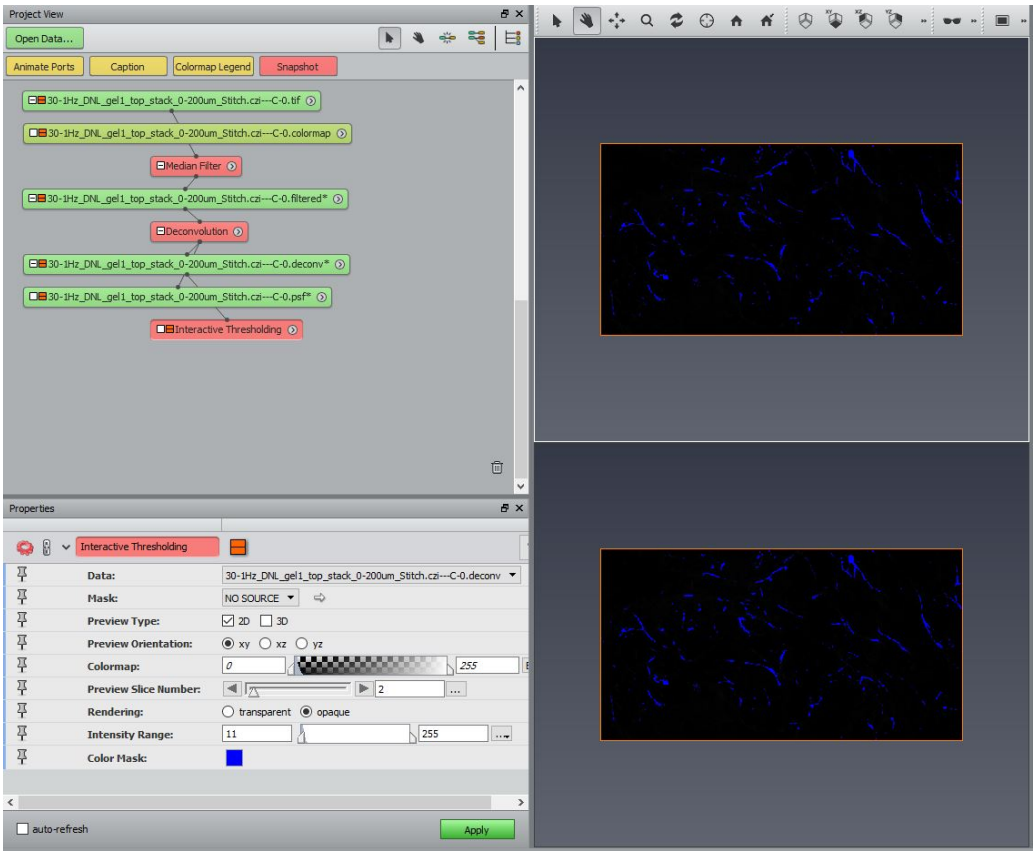

4. Remove Islands
    a. Select > of .thresholded and go to Segmentation tab
    b. Ensure Exterior is assigned to gel and Interior (or Material1) is assigned to the vessels
    c. Change the color of Exterior to black by clicking on color square to left of Exterior text, and change the color of Interior to white
    d. Select Interior by clicking “select” to its right

e. 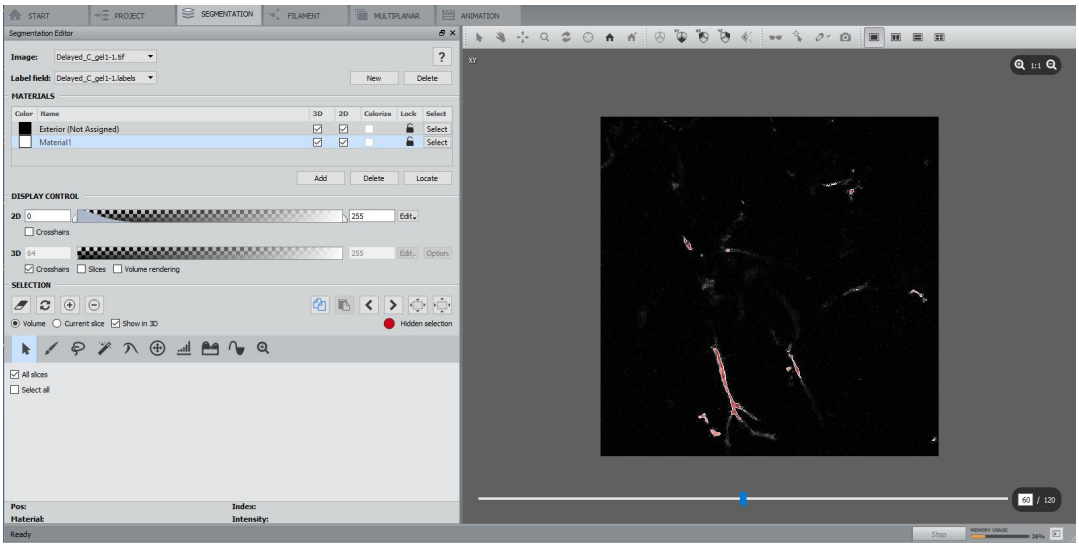

f. Click on Segmentation menu (top bar of dropdowns, right of File Edit etc.) and select Remove Islands…

g. Consider as islands all connected regions smaller than 30 voxels and select Apply to: All slices

h. 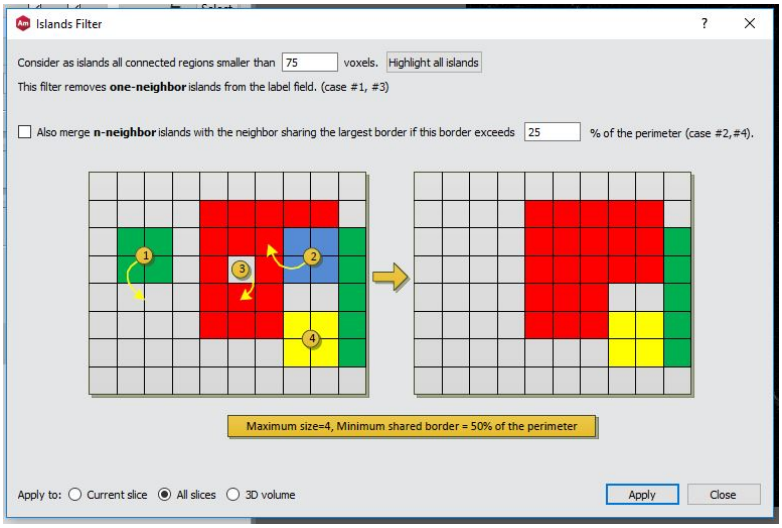

5. Save as .tif file (Click on .thresholded file→ export data as→ use “3D .tif” as your file type)

II. FARSIGHT Toolkit

1. Load Amira preprocessed Image into Farsight Tracing System 0.4.4 (“Load Image”, middle RH panel). Different views available above image itself. Click Next (bottom R).

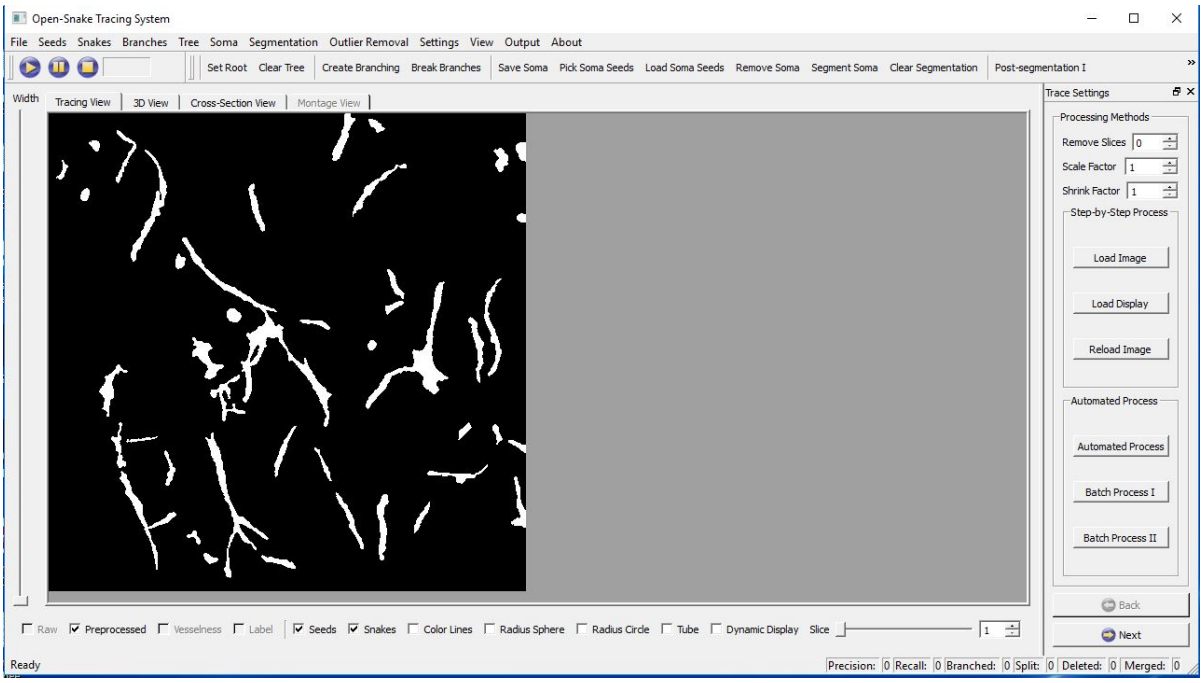

2. Default settings ok (threshold = 1 used here since image was thresholded in Amira). Click Preprocessing. This finds the seeds from which to create snakes and can take on the order of minutes. Click Next.

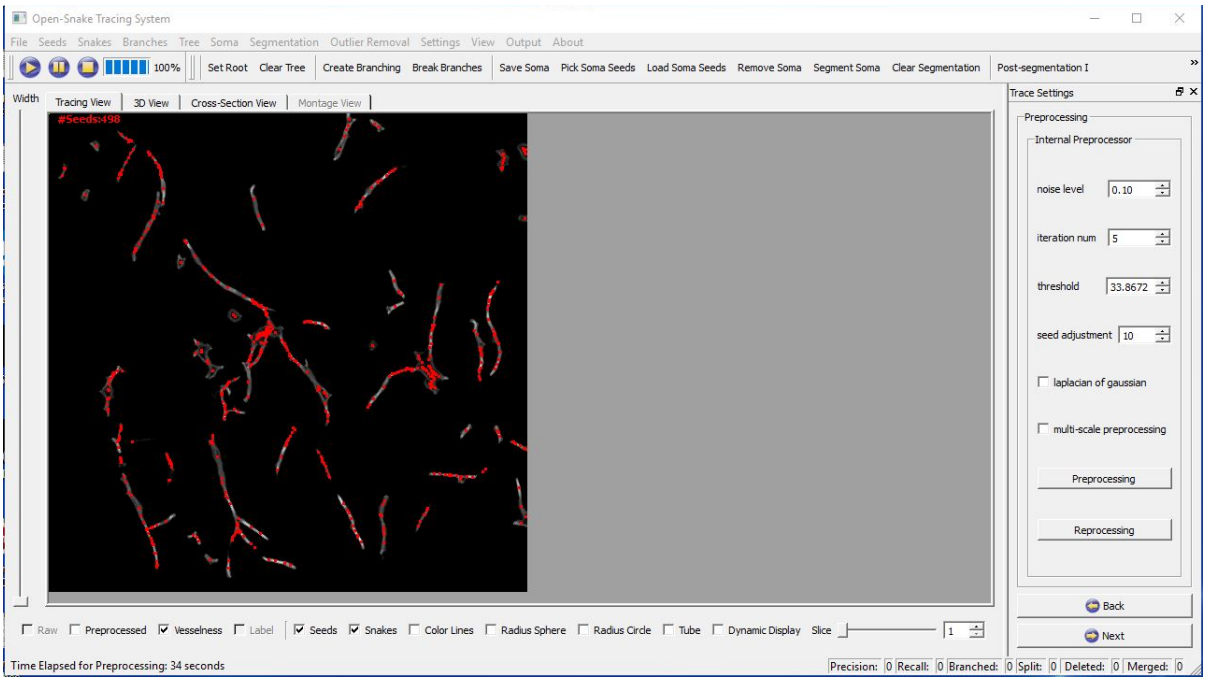

3. Select “4-D Open Snake (Elliptic)” from the top drop down and “Vessel Tube Coding” from the second drop down. Set min length to 30. Other default settings are fine. Click Tracing. On Tracing view, you can watch the snakes trace in real time. You can also watch the “progress bar” in the upper left corner. When done, click Next.

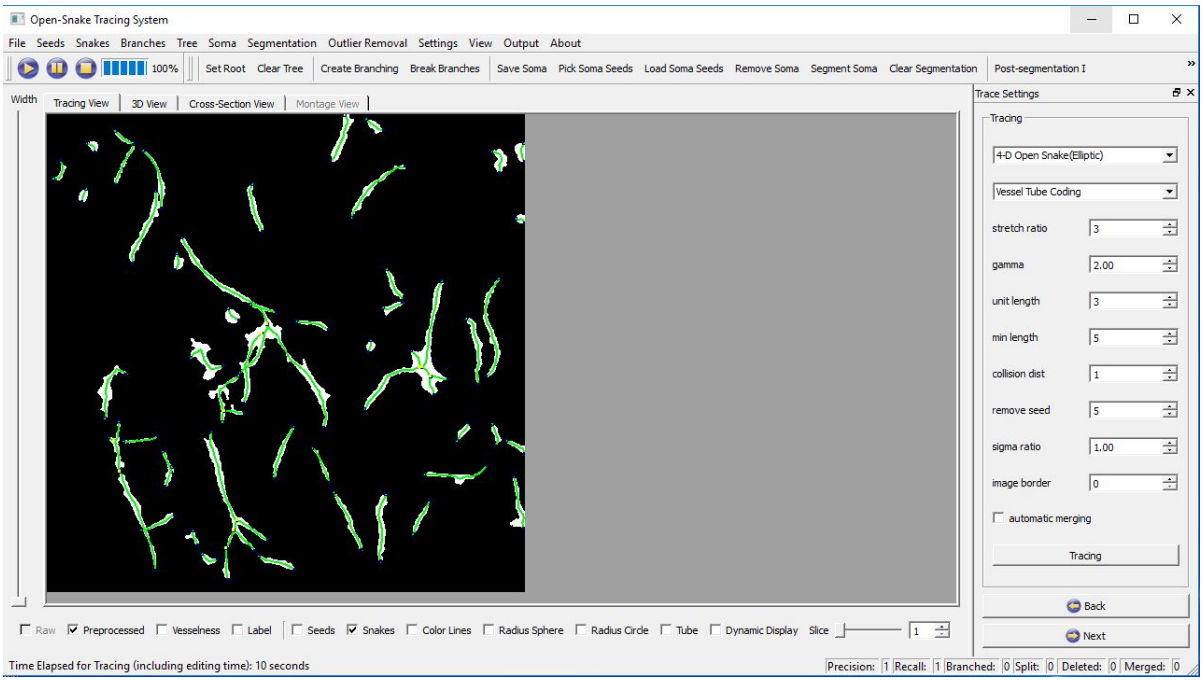

4. Output .swc file by clicking Output Raw SWC. Can also tick boxes below image to show radius circles, radius spheres, etc. and export these images from the Output menu at very top.

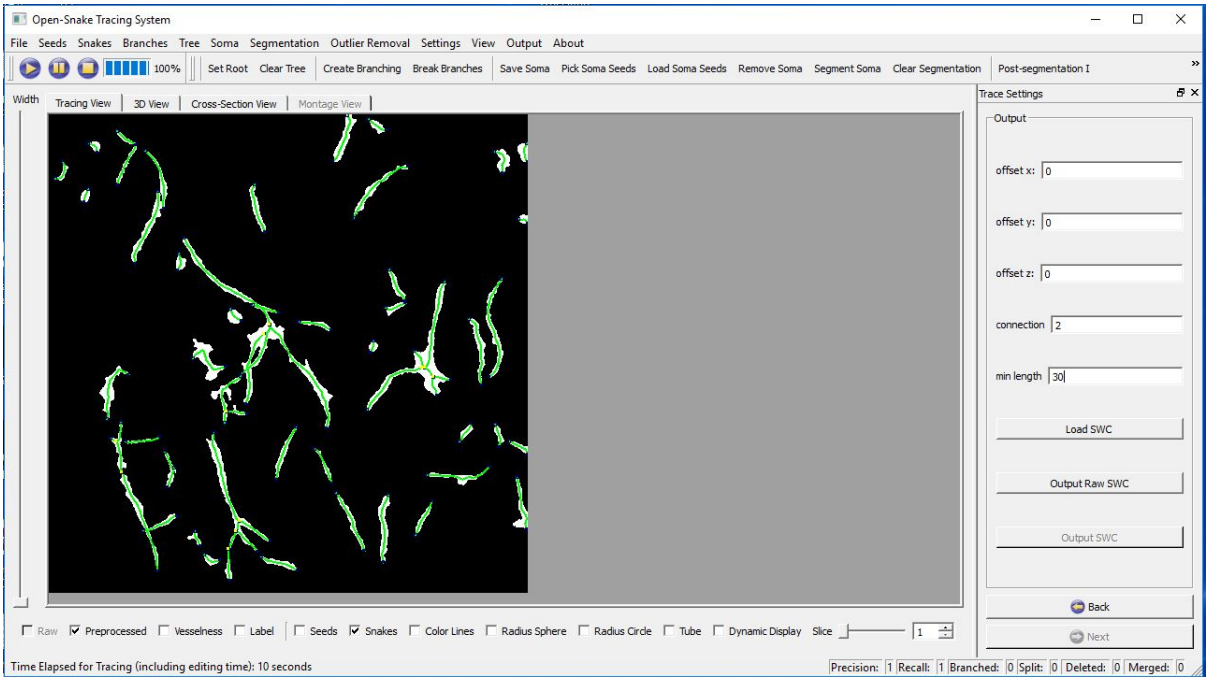

5. Open TraceEdit 0.4.5. Load .swc (yellow) and image files (red) and click Start.

6. Visually confirm agreement between image file and .swc tracing. Note: can delete snakes due to artifact (e.g. bubble on surface of gel) by right clicking and pressing delete in upper left.

7. Analysis -> Cell Analysis outputs (x,y,z) coordinates, segment length, branch points, radius, volume, surface area, etc. Export -> Save as… .xls

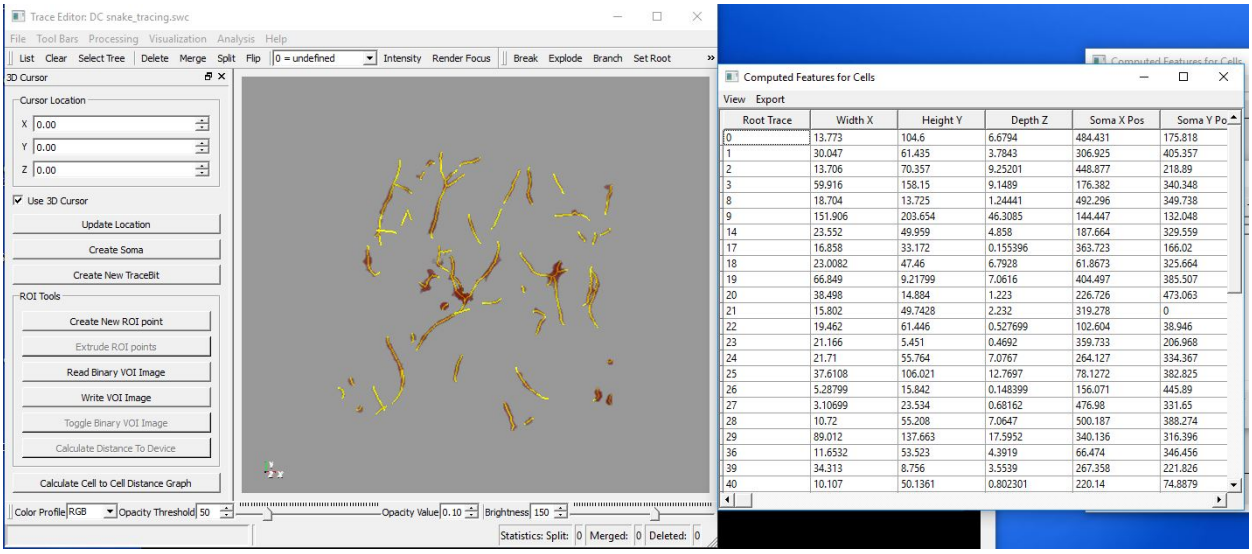

REFERENCES

1. Morgan, E.F., G.L. Barnes, and T.A. Einhorn, *The bone organ system: form and function*, in *Osteoporosis*. 2013, Elsevier. p. 3-20.

2. Brini, M., et al., *Intracellular calcium homeostasis and signaling.* Met Ions Life Sci, 2013. **12**: p. 119-68.

3. Mori, G., et al., *The Interplay between the bone and the immune system.* Clin Dev Immunol, 2013. **2013**: p. 720504.

4. Charbord, P., *Bone marrow mesenchymal stem cells: historical overview and concepts.* Hum Gene Ther, 2010. **21**(9): p. 1045-56.

5. Boskey, A.L., *Biomineralization: conflicts, challenges, and opportunities.* J Cell Biochem Suppl, 1998. **30-31**: p. 83-91.

6. Franz-Odendaal, T.A., B.K. Hall, and P.E. Witten, *Buried alive: how osteoblasts become osteocytes.* Dev Dyn, 2006. **235**(1): p. 176-90.

7. Arsenault, A.L., *Vascular canals in bovine cortical bone studied by corrosion casting.* Calcified tissue international, 1990. **47**(5): p. 320-325.

8. Calori, G.M., et al., *Treatment of long bone non-unions with polytherapy: indications and clinical results.* Injury, 2011. **42**(6): p. 587-90.

9. Hoffman, M. and D.M. Monroe, *Coagulation 2006: a modern view of hemostasis.* Hematol Oncol Clin North Am, 2007. **21**(1): p. 1-11.

10. Einhorn, T.A. and L.C. Gerstenfeld, *Fracture healing: mechanisms and interventions.* Nat Rev Rheumatol, 2015. **11**(1): p. 45-54.

11. Filipowska, J., et al., *The role of vasculature in bone development, regeneration and proper systemic functioning.* Angiogenesis, 2017.

12. Marsell, R. and T.A. Einhorn, *The biology of fracture healing.* Injury, 2011. **42**(6): p. 551-5.

13. Stoeger, T., et al., *In situ gene expression analysis during BMP2-induced ectopic bone formation in mice shows simultaneous endochondral and intramembranous ossification.* Growth Factors, 2002. **20**(4): p. 197-210.

14. Enoch, S. and D.J. Leaper, *Basic science of wound healing.* Surgery (Oxford), 2008. **26**(2): p. 31-37.

15. Lu, C., et al., *Ischemia leads to delayed union during fracture healing: a mouse model.* J Orthop Res, 2007. **25**(1): p. 51-61.

16. Hyzy, S.L., et al., *Inhibition of angiogenesis impairs bone healing in an in vivo murine rapid resynostosis model.* J Biomed Mater Res A, 2017. **105**(10): p. 2742-2749.

17. Liu, C. and A.B. Castillo, *Targeting Osteogenesis-Angiogenesis Coupling for Bone Repair.* J Am Acad Orthop Surg, 2018. **26**(7): p. e153-e155.

18. Maes, C., et al., *Osteoblast precursors, but not mature osteoblasts, move into developing and fractured bones along with invading blood vessels.* Dev Cell, 2010. **19**(2): p. 329-44.

19. Marenzana, M. and T.R. Arnett, *The Key Role of the Blood Supply to Bone.* Bone Res, 2013. **1**(3): p. 203-15.

20. Kusumbe, A.P., S.K. Ramasamy, and R.H. Adams, *Coupling of angiogenesis and osteogenesis by a specific vessel subtype in bone.* Nature, 2014. **507**(7492): p. 323-328.

21. Pugsley, M.K. and R. Tabrizchi, *The vascular system. An overview of structure and function.* J Pharmacol Toxicol Methods, 2000. **44**(2): p. 333-40.

22. Adair, T.H. and J.-P. Montani. *Angiogenesis*. in *Colloquium Series on Integrated Systems Physiology: From Molecule to Function*. 2010. Morgan & Claypool Life Sciences.

23. Yuan, S. and R. Rigor, *Chapter 2, Structure and Function of Exchange Microvessels.* Regulation of Endothelial Barrier Function, 2010.

24. Kolka, C.M. and R.N. Bergman, *The barrier within: endothelial transport of hormones.* Physiology (Bethesda), 2012. **27**(4): p. 237-47.

25. Reitsma, S., et al., *The endothelial glycocalyx: composition, functions, and visualization.* Pflugers Arch, 2007. **454**(3): p. 345-59.

26. Yu, Q.C., et al., *Identification of blood vascular endothelial stem cells by the expression of protein C receptor.* Cell Res, 2016. **26**(10): p. 1079-1098.

27. Bergers, G. and S. Song, *The role of pericytes in blood-vessel formation and maintenance.* Neuro Oncol, 2005. **7**(4): p. 452-64.

28. Caplan, A.I., *All MSCs are pericytes?* Cell Stem Cell, 2008. **3**(3): p. 229-30.

29. Patan, S., *Vasculogenesis and angiogenesis as mechanisms of vascular network formation, growth and remodeling.* J Neurooncol, 2000. **50**(1-2): p. 1-15.

30. Geudens, I. and H. Gerhardt, *Coordinating cell behaviour during blood vessel formation.* Development, 2011. **138**(21): p. 4569-83.

31. Otrock, Z.K., et al., *Understanding the biology of angiogenesis: review of the most important molecular mechanisms.* Blood Cells Mol Dis, 2007. **39**(2): p. 212-20.

32. Raza, S.L. and L.A. Cornelius, *Matrix metalloproteinases: pro- and anti-angiogenic activities.* J Investig Dermatol Symp Proc, 2000. **5**(1): p. 47-54.

33. Friedl, P. and D. Gilmour, *Collective cell migration in morphogenesis, regeneration and cancer.* Nat Rev Mol Cell Biol, 2009. **10**(7): p. 445-57.

34. Savant, S., et al., *The Orphan Receptor Tie1 Controls Angiogenesis and Vascular Remodeling by Differentially Regulating Tie2 in Tip and Stalk Cells.* Cell Rep, 2015. **12**(11): p. 1761-73.

35. Zura, R., et al., *Epidemiology of Fracture Nonunion in 18 Human Bones.* JAMA Surg, 2016. **151**(11): p. e162775.

36. Westgeest, J., et al., *Factors Associated With Development of Nonunion or Delayed Healing After an Open Long Bone Fracture: A Prospective Cohort Study of 736 Subjects.* J Orthop Trauma, 2016. **30**(3): p. 149-55.

37. Mehta, S., et al., *Low-intensity pulsed ultrasound (LIPUS) can decrease the economic burden of fracture non-union.* J Med Econ, 2015. **18**(7): p. 542-9.

38. Gustilo, R.B., R.L. Merkow, and D. Templeman, *The management of open fractures.* J Bone Joint Surg Am, 1990. **72**(2): p. 299-304.

39. Zalavras, C.G., et al., *Management of open fractures and subsequent complications.* J Bone Joint Surg Am, 2007. **89**(4): p. 884-95.

40. Hurtgen, B.J., et al., *Severe muscle trauma triggers heightened and prolonged local musculoskeletal inflammation and impairs adjacent tibia fracture healing.* J Musculoskelet Neuronal Interact, 2016. **16**(2): p. 122-34.

41. Pollot, B.E., et al., *Decellularized extracellular matrix repair of volumetric muscle loss injury impairs adjacent bone healing in a rat model of complex musculoskeletal trauma.* J Trauma Acute Care Surg, 2016. **81**(5 Suppl 2 Proceedings of the 2015 Military Health System Research Symposium): p. S184-S190.

42. Willett, N.J., et al., *Attenuated human bone morphogenetic protein-2-mediated bone regeneration in a rat model of composite bone and muscle injury.* Tissue Eng Part C Methods, 2013. **19**(4): p. 316-25.

43. Li, M.T., *Treatment Strategy for Composite Limb Trauma, Doctoral Dissertation*, in *Biomedical Engineering*. 2015, Georgia Institute of Technology

44. Ruehle, M.A., et al., *Decorin-supplemented collagen hydrogels for the co-delivery of bone morphogenetic protein-2 and microvascular fragments to a composite bone-muscle injury model with impaired vascularization.* Acta Biomater, 2019.

45. Schwartz, A.M., et al., *Building better bone: the weaving of biologic and engineering strategies for managing bone loss.* J Orthop Res, 2017.

46. Egol, K.A., et al., *Bone grafting: sourcing, timing, strategies, and alternatives.* Journal of orthopaedic trauma, 2015. **29**: p. S10-S14.

47. Dawson, J., et al., *The reamer-irrigator-aspirator as a device for harvesting bone graft compared with iliac crest bone graft: union rates and complications.* J Orthop Trauma, 2014. **28**(10): p. 584-90.

48. Laurencin, C., Y. Khan, and S.F. El-Amin, *Bone graft substitutes.* Expert Rev Med Devices, 2006. **3**(1): p. 49-57.

49. Gruskin, E., et al., *Demineralized bone matrix in bone repair: history and use.* Adv Drug Deliv Rev, 2012. **64**(12): p. 1063-77.

50. Godina, M., *Early microsurgical reconstruction of complex trauma of the extremities.* Plast Reconstr Surg, 1986. **78**(3): p. 285-92.

51. MacKenzie, E.J., et al., *Long-term persistence of disability following severe lower-limb trauma. Results of a seven-year follow-up.* J Bone Joint Surg Am, 2005. **87**(8): p. 1801-9.

52. Bosse, M.J., et al., *An analysis of outcomes of reconstruction or amputation after leg-threatening injuries.* N Engl J Med, 2002. **347**(24): p. 1924-31.

53. Fairhurst, M.J., *The function of below-knee amputee versus the patient with salvaged grade III tibial fracture.* Clin Orthop Relat Res, 1994(301): p. 227-32.

54. Rosenbloom, B.N., et al., *Systematic review of persistent pain and psychological outcomes following traumatic musculoskeletal injury.* J Pain Res, 2013. **6**: p. 39-51.

55. MacKenzie, E.J., et al., *Factors influencing the decision to amputate or reconstruct after high-energy lower extremity trauma.* J Trauma, 2002. **52**(4): p. 641-9.

56. Kempen, D.H., et al., *Growth factor interactions in bone regeneration.* Tissue Eng Part B Rev, 2010. **16**(6): p. 551-66.

57. Vantucci, C.E., K. Roy, and R.E. Guldberg, *Immunomodulatory strategies for immune dysregulation following severemusculoskeletal trauma.* Journal of Immunology and Regenerative Medicine, 2018. **2**: p. 21-35.

58. Einhorn, T.A., *Clinical applications of recombinant human BMPs: early experience and future development.* J Bone Joint Surg Am, 2003. **85-A Suppl 3**: p. 82-8.

59. Dimitriou, R., E. Tsiridis, and P.V. Giannoudis, *Current concepts of molecular aspects of bone healing.* Injury, 2005. **36**(12): p. 1392-404.

60. Geesink, R.G., N.H. Hoefnagels, and S.K. Bulstra, *Osteogenic activity of OP-1 bone morphogenetic protein (BMP-7) in a human fibular defect.* J Bone Joint Surg Br, 1999. **81**(4): p. 710-8.

61. Oest, M.E., et al., *Quantitative assessment of scaffold and growth factor-mediated repair of critically sized bone defects.* J Orthop Res, 2007. **25**(7): p. 941-50.

62. Lan, J., et al., *The effect of combination of recombinant human bone morphogenetic protein-2 and basic fibroblast growth factor or insulin-like growth factor-I on dental implant osseointegration by confocal laser scanning microscopy.* J Periodontol, 2006. **77**(3): p. 357-63.

63. Vonau, R.L., et al., *Combination of growth factors inhibits bone ingrowth in the bone harvest chamber.* Clin Orthop Relat Res, 2001(386): p. 243-51.

64. Heckman, J.D., et al., *Bone morphogenetic protein but not transforming growth factor-beta enhances bone formation in canine diaphyseal nonunions implanted with a biodegradable composite polymer.* J Bone Joint Surg Am, 1999. **81**(12): p. 1717-29.

65. Jones, E. and X. Yang, *Mesenchymal stem cells and bone regeneration: current status.* Injury, 2011. **42**(6): p. 562-8.

66. Dupont, K.M., et al., *Human stem cell delivery for treatment of large segmental bone defects.* Proc Natl Acad Sci U S A, 2010. **107**(8): p. 3305-10.

67. Dosier, C.R., et al., *Effect of cell origin and timing of delivery for stem cell-based bone tissue engineering using biologically functionalized hydrogels.* Tissue Eng Part A, 2015. **21**(1-2): p. 156-65.

68. Allen, A.B., et al., *Environmental manipulation to promote stem cell survival in vivo: use of aggregation, oxygen carrier, and BMP-2 co-delivery strategies.* Journal of Materials Chemistry B, 2016. **4**(20): p. 3594-3607.

69. Boden, S.D., et al., *Use of recombinant human bone morphogenetic protein-2 to achieve posterolateral lumbar spine fusion in humans: a prospective, randomized clinical pilot trial: 2002 Volvo Award in clinical studies.* Spine (Phila Pa 1976), 2002. **27**(23): p. 2662-73.

70. Govender, S., et al., *Recombinant human bone morphogenetic protein-2 for treatment of open tibial fractures: a prospective, controlled, randomized study of four hundred and fifty patients.* J Bone Joint Surg Am, 2002. **84-A**(12): p. 2123-34.

71. Geiger, M., R.H. Li, and W. Friess, *Collagen sponges for bone regeneration with rhBMP-2.* Adv Drug Deliv Rev, 2003. **55**(12): p. 1613-29.

72. Cho, T.J., L.C. Gerstenfeld, and T.A. Einhorn, *Differential temporal expression of members of the transforming growth factor beta superfamily during murine fracture healing.* J Bone Miner Res, 2002. **17**(3): p. 513-20.

73. James, A.W., et al., *A Review of the Clinical Side Effects of Bone Morphogenetic Protein-2.* Tissue Eng Part B Rev, 2016. **22**(4): p. 284-97.

74. Kolambkar, Y.M., et al., *Spatiotemporal delivery of bone morphogenetic protein enhances functional repair of segmental bone defects.* Bone, 2011. **49**(3): p. 485-92.

75. Kolambkar, Y.M., et al., *An alginate-based hybrid system for growth factor delivery in the functional repair of large bone defects.* Biomaterials, 2011. **32**(1): p. 65-74.

76. Park, Y.J., et al., *Immobilization of bone morphogenetic protein-2 on a nanofibrous chitosan membrane for enhanced guided bone regeneration.* Biotechnol Appl Biochem, 2006. **43**(Pt 1): p. 17-24.

77. Park, K.H., et al., *Bone morphogenic protein-2 (BMP-2) loaded nanoparticles mixed with human mesenchymal stem cell in fibrin hydrogel for bone tissue engineering.* J Biosci Bioeng, 2009. **108**(6): p. 530-7.

78. Kim, J., et al., *Bone regeneration using hyaluronic acid-based hydrogel with bone morphogenic protein-2 and human mesenchymal stem cells.* Biomaterials, 2007. **28**(10): p. 1830-7.

79. Melke, J., et al., *Silk fibroin as biomaterial for bone tissue engineering.* Acta Biomater, 2016. **31**: p. 1-16.

80. Liu, H.W., et al., *Heterobifunctional poly(ethylene glycol)-tethered bone morphogenetic protein-2-stimulated bone marrow mesenchymal stromal cell differentiation and osteogenesis.* Tissue Eng, 2007. **13**(5): p. 1113-24.

81. Jeon, O., et al., *Enhancement of ectopic bone formation by bone morphogenetic protein-2 released from a heparin-conjugated poly(L-lactic-co-glycolic acid) scaffold.* Biomaterials, 2007. **28**(17): p. 2763-71.

82. Shrivats, A.R., M.C. McDermott, and J.O. Hollinger, *Bone tissue engineering: state of the union.* Drug Discov Today, 2014. **19**(6): p. 781-6.

83. Burg, K.J., S. Porter, and J.F. Kellam, *Biomaterial developments for bone tissue engineering.* Biomaterials, 2000. **21**(23): p. 2347-59.

84. Bose, S. and S. Tarafder, *Calcium phosphate ceramic systems in growth factor and drug delivery for bone tissue engineering: a review.* Acta Biomater, 2012. **8**(4): p. 1401-21.

85. Branco da Cunha, C., et al., *Influence of the stiffness of three-dimensional alginate/collagen-I interpenetrating networks on fibroblast biology.* Biomaterials, 2014. **35**(32): p. 8927-36.

86. Venkatesan, J., et al., *Alginate composites for bone tissue engineering: a review.* Int J Biol Macromol, 2015. **72**: p. 269-81.

87. Kim, S.S., et al., *Poly(lactide-co-glycolide)/hydroxyapatite composite scaffolds for bone tissue engineering.* Biomaterials, 2006. **27**(8): p. 1399-409.

88. Lafage-Proust, M.H., et al., *Assessment of bone vascularization and its role in bone remodeling.* Bonekey Rep, 2015. **4**: p. 662.

89. Cartmell, S.H., et al., *Effects of medium perfusion rate on cell-seeded three-dimensional bone constructs in vitro.* Tissue Eng, 2003. **9**(6): p. 1197-203.

90. Gerstenfeld, L.C., et al., *Fracture healing as a post-natal developmental process: molecular, spatial, and temporal aspects of its regulation.* J Cell Biochem, 2003. **88**(5): p. 873-84.

91. Zhang, W., et al., *VEGF and BMP-2 promote bone regeneration by facilitating bone marrow stem cell homing and differentiation.* Eur Cell Mater, 2014. **27**: p. 1-11; discussion 11-2.

92. Subbiah, R., et al., *Osteogenic/angiogenic dual growth factor delivery microcapsules for regeneration of vascularized bone tissue.* Adv Healthc Mater, 2015. **4**(13): p. 1982-92.

93. Peng, H., et al., *VEGF improves, whereas sFlt1 inhibits, BMP2-induced bone formation and bone healing through modulation of angiogenesis.* J Bone Miner Res, 2005. **20**(11): p. 2017-27.

94. Hernandez, A., et al., *In vivo osteogenic response to different ratios of BMP-2 and VEGF released from a biodegradable porous system.* J Biomed Mater Res A, 2012. **100**(9): p. 2382-91.

95. Geuze, R.E., et al., *A differential effect of bone morphogenetic protein-2 and vascular endothelial growth factor release timing on osteogenesis at ectopic and orthotopic sites in a large-animal model.* Tissue Eng Part A, 2012. **18**(19-20): p. 2052-62.

96. Patel, Z.S., et al., *Dual delivery of an angiogenic and an osteogenic growth factor for bone regeneration in a critical size defect model.* Bone, 2008. **43**(5): p. 931-40.

97. Suzuki, Y., et al., *BMPs promote proliferation and migration of endothelial cells via stimulation of VEGF-A/VEGFR2 and angiopoietin-1/Tie2 signalling.* J Biochem, 2008. **143**(2): p. 199-206.

98. Bouletreau, P.J., et al., *Hypoxia and VEGF up-regulate BMP-2 mRNA and protein expression in microvascular endothelial cells: implications for fracture healing.* Plast Reconstr Surg, 2002. **109**(7): p. 2384-97.

99. Kempen, D.H., et al., *Effect of local sequential VEGF and BMP-2 delivery on ectopic and orthotopic bone regeneration.* Biomaterials, 2009. **30**(14): p. 2816-25.

100. Garcia, J.R., A.Y. Clark, and A.J. Garcia, *Integrin-specific hydrogels functionalized with VEGF for vascularization and bone regeneration of critical-size bone defects.* J Biomed Mater Res A, 2016. **104**(4): p. 889-900.

101. Seebach, C., et al., *Endothelial progenitor cells and mesenchymal stem cells seeded onto beta-TCP granules enhance early vascularization and bone healing in a critical-sized bone defect in rats.* Tissue Eng Part A, 2010. **16**(6): p. 1961-70.

102. Liu, Y., et al., *Contrasting effects of vasculogenic induction upon biaxial bioreactor stimulation of mesenchymal stem cells and endothelial progenitor cells cocultures in three-dimensional scaffolds under in vitro and in vivo paradigms for vascularized bone tissue engineering.* Tissue Eng Part A, 2013. **19**(7-8): p. 893-904.

103. Wang, L., et al., *Osteogenesis and angiogenesis of tissue-engineered bone constructed by prevascularized beta-tricalcium phosphate scaffold and mesenchymal stem cells.* Biomaterials, 2010. **31**(36): p. 9452-61.

104. Yu, H., et al., *Improved tissue-engineered bone regeneration by endothelial cell mediated vascularization.* Biomaterials, 2009. **30**(4): p. 508-17.

105. Tsigkou, O., et al., *Engineered vascularized bone grafts.* Proc Natl Acad Sci U S A, 2010. **107**(8): p. 3311-6.

106. Levit, R.D., et al., *Cellular encapsulation enhances cardiac repair.* J Am Heart Assoc, 2013. **2**(5): p. e000367.

107. Hoying, J.B., C.A. Boswell, and S.K. Williams, *Angiogenic potential of microvessel fragments established in three-dimensional collagen gels.* In Vitro Cell Dev Biol Anim, 1996. **32**(7): p. 409-19.

108. Laschke, M.W., et al., *Effects of cryopreservation on adipose tissue-derived microvascular fragments.* J Tissue Eng Regen Med, 2017.

109. Nunes, S.S., et al., *Angiogenic potential of microvessel fragments is independent of the tissue of origin and can be influenced by the cellular composition of the implants.* Microcirculation, 2010. **17**(7): p. 557-67.

110. Krishnan, L., et al., *Interaction of angiogenic microvessels with the extracellular matrix.* Am J Physiol Heart Circ Physiol, 2007. **293**(6): p. H3650-8.

111. Krishnan, L., et al., *Effect of mechanical boundary conditions on orientation of angiogenic microvessels.* Cardiovasc Res, 2008. **78**(2): p. 324-32.

112. Edgar, L.T., et al., *Mechanical interaction of angiogenic microvessels with the extracellular matrix.* J Biomech Eng, 2014. **136**(2): p. 021001.

113. Edgar, L.T., et al., *Extracellular matrix density regulates the rate of neovessel growth and branching in sprouting angiogenesis.* PLoS One, 2014. **9**(1): p. e85178.

114. Shepherd, B.R., et al., *Rapid perfusion and network remodeling in a microvascular construct after implantation.* Arterioscler Thromb Vasc Biol, 2004. **24**(5): p. 898-904.

115. Laschke, M.W., et al., *Short-term cultivation of in situ prevascularized tissue constructs accelerates inosculation of their preformed microvascular networks after implantation into the host tissue.* Tissue Eng Part A, 2011. **17**(5-6): p. 841-53.

116. Li, M.T., et al., *Skeletal myoblast-seeded vascularized tissue scaffolds in the treatment of a large volumetric muscle defect in the rat biceps femoris muscle.* Tissue Eng Part A, 2017.

117. Pilia, M., et al., *Transplantation and perfusion of microvascular fragments in a rodent model of volumetric muscle loss injury.* Eur Cell Mater, 2014. **28**: p. 11-23; discussion 23-4.

118. Frueh, F.S., et al., *Prevascularization of dermal substitutes with adipose tissue-derived microvascular fragments enhances early skin grafting.* Sci Rep, 2018. **8**(1): p. 10977.

119. Frueh, F.S., et al., *Adipose Tissue-Derived Microvascular Fragments Improve Vascularization, Lymphangiogenesis, and Integration of Dermal Skin Substitutes.* J Invest Dermatol, 2017. **137**(1): p. 217-227.

120. Ramakrishnan, V.M. and N.L. Boyd, *The Adipose Stromal Vascular Fraction as a Complex Cellular Source for Tissue Engineering Applications.* Tissue Eng Part B Rev, 2017.

121. Zimmerlin, L., et al., *Stromal vascular progenitors in adult human adipose tissue.* Cytometry A, 2010. **77**(1): p. 22-30.

122. Nunes, S.S., et al., *Generation of a functional liver tissue mimic using adipose stromal vascular fraction cell-derived vasculatures.* Sci Rep, 2013. **3**: p. 2141.

123. Saxer, F., et al., *Implantation of Stromal Vascular Fraction Progenitors at Bone Fracture Sites: From a Rat Model to a First-in-Man Study.* Stem Cells, 2016. **34**(12): p. 2956-2966.

124. Frost, H.M., *The Utah paradigm of skeletal physiology: an overview of its insights for bone, cartilage and collagenous tissue organs.* J Bone Miner Metab, 2000. **18**(6): p. 305-16.

125. Lanyon, L.E., et al., *Mechanically adaptive bone remodelling.* J Biomech, 1982. **15**(3): p. 141-54.

126. Duncan, R.L. and C.H. Turner, *Mechanotransduction and the functional response of bone to mechanical strain.* Calcif Tissue Int, 1995. **57**(5): p. 344-58.

127. Claes, L.E., et al., *Effects of mechanical factors on the fracture healing process.* Clin Orthop Relat Res, 1998(355 Suppl): p. S132-47.

128. Ignatius, A., et al., *Tissue engineering of bone: effects of mechanical strain on osteoblastic cells in type I collagen matrices.* Biomaterials, 2005. **26**(3): p. 311-8.

129. Lacroix, D. and P.J. Prendergast, *A mechano-regulation model for tissue differentiation during fracture healing: analysis of gap size and loading.* J Biomech, 2002. **35**(9): p. 1163-71.

130. Perren, S.M., *Physical and biological aspects of fracture healing with special reference to internal fixation.* Clin Orthop Relat Res, 1979(138): p. 175-96.

131. Cheal, E.J., et al., *Role of interfragmentary strain in fracture healing: ovine model of a healing osteotomy.* J Orthop Res, 1991. **9**(1): p. 131-42.

132. Engler, A.J., et al., *Matrix elasticity directs stem cell lineage specification.* Cell, 2006. **126**(4): p. 677-89.

133. Mauney, J.R., et al., *Mechanical stimulation promotes osteogenic differentiation of human bone marrow stromal cells on 3-D partially demineralized bone scaffolds in vitro.* Calcif Tissue Int, 2004. **74**(5): p. 458-68.

134. Rubin, C.T. and L.E. Lanyon, *Regulation of bone mass by mechanical strain magnitude.* Calcif Tissue Int, 1985. **37**(4): p. 411-7.

135. Frost, H.M., *Bone's mechanostat: a 2003 update.* Anat Rec A Discov Mol Cell Evol Biol, 2003. **275**(2): p. 1081-101.

136. Boerckel, J.D., et al., *Mechanical regulation of vascular growth and tissue regeneration in vivo.* Proc Natl Acad Sci U S A, 2011. **108**(37): p. E674-80.

137. Goodship, A.E. and J. Kenwright, *The influence of induced micromovement upon the healing of experimental tibial fractures.* J Bone Joint Surg Br, 1985. **67**(4): p. 650-5.

138. Claes, L.E., et al., *Effect of dynamization on gap healing of diaphyseal fractures under external fixation.* Clin Biomech (Bristol, Avon), 1995. **10**(5): p. 227-234.

139. Epari, D.R., et al., *Instability prolongs the chondral phase during bone healing in sheep.* Bone, 2006. **38**(6): p. 864-70.

140. Claes, L., et al., *Influence of size and stability of the osteotomy gap on the success of fracture healing.* J Orthop Res, 1997. **15**(4): p. 577-84.

141. Megas, P., *Classification of non-union.* Injury, 2005. **36 Suppl 4**: p. S30-7.

142. Miller, G.J., L.C. Gerstenfeld, and E.F. Morgan, *Mechanical microenvironments and protein expression associated with formation of different skeletal tissues during bone healing.* Biomech Model Mechanobiol, 2015. **14**(6): p. 1239-53.

143. Claes, L.E. and C.A. Heigele, *Magnitudes of local stress and strain along bony surfaces predict the course and type of fracture healing.* J Biomech, 1999. **32**(3): p. 255-66.

144. Betts, D.C. and R. Muller, *Mechanical regulation of bone regeneration: theories, models, and experiments.* Front Endocrinol (Lausanne), 2014. **5**: p. 211.

145. Ilizarov, G.A., *The tension-stress effect on the genesis and growth of tissues: Part II. The influence of the rate and frequency of distraction.* Clinical orthopaedics and related research, 1989(239): p. 263-285.

146. Hente, R., et al., *The influence of cyclic compression and distraction on the healing of experimental tibial fractures.* J Orthop Res, 2004. **22**(4): p. 709-15.

147. Lanyon, L.E. and C.T. Rubin, *Static vs dynamic loads as an influence on bone remodelling.* J Biomech, 1984. **17**(12): p. 897-905.

148. Danion, F., et al., *Stride variability in human gait: the effect of stride frequency and stride length.* Gait Posture, 2003. **18**(1): p. 69-77.

149. McBride, S.H. and M.J. Silva, *Adaptive and Injury Response of Bone to Mechanical Loading.* Bonekey Osteovision, 2012. **1**.

150. Hsieh, Y.F. and C.H. Turner, *Effects of loading frequency on mechanically induced bone formation.* J Bone Miner Res, 2001. **16**(5): p. 918-24.

151. Rubin, C., et al., *Anabolism. Low mechanical signals strengthen long bones.* Nature, 2001. **412**(6847): p. 603-4.

152. Goodship, A.E., T.J. Lawes, and C.T. Rubin, *Low-magnitude high-frequency mechanical signals accelerate and augment endochondral bone repair: preliminary evidence of efficacy.* J Orthop Res, 2009. **27**(7): p. 922-30.

153. Forwood, M.R., et al., *Increased bone formation in rat tibiae after a single short period of dynamic loading in vivo.* Am J Physiol, 1996. **270**(3 Pt 1): p. E419-23.

154. Rubin, C.T. and L.E. Lanyon, *Regulation of bone formation by applied dynamic loads.* J Bone Joint Surg Am, 1984. **66**(3): p. 397-402.

155. Robling, A.G., et al., *Improved bone structure and strength after long-term mechanical loading is greatest if loading is separated into short bouts.* J Bone Miner Res, 2002. **17**(8): p. 1545-54.

156. Robling, A.G., D.B. Burr, and C.H. Turner, *Recovery periods restore mechanosensitivity to dynamically loaded bone.* J Exp Biol, 2001. **204**(Pt 19): p. 3389-99.

157. Gardner, M.J., et al., *In vivo cyclic axial compression affects bone healing in the mouse tibia.* J Orthop Res, 2006. **24**(8): p. 1679-86.

158. Chiu, J.J. and S. Chien, *Effects of Disturbed Flow on Vascular Endothelium: Pathophysiological Basis and Clinical Perspectives.* Physiological Reviews, 2011. **91**(1): p. 327-387.

159. Nerem, R.M., et al., *The study of the influence of flow on vascular endothelial biology.* Am J Med Sci, 1998. **316**(3): p. 169-75.

160. Dewey, C.F., Jr., et al., *The dynamic response of vascular endothelial cells to fluid shear stress.* J Biomech Eng, 1981. **103**(3): p. 177-85.

161. Eskin, S.G., et al., *Response of Cultured Endothelial-Cells to Steady Flow.* Microvascular Research, 1984. **28**(1): p. 87-94.

162. Levesque, M.J. and R.M. Nerem, *The Elongation and Orientation of Cultured Endothelial-Cells in Response to Shear-Stress.* Journal of Biomechanical Engineering-Transactions of the Asme, 1985. **107**(4): p. 341-347.

163. Davies, P.F., et al., *Influence of hemodynamic forces on vascular endothelial function. In vitro studies of shear stress and pinocytosis in bovine aortic cells.* J Clin Invest, 1984. **73**(4): p. 1121-9.

164. Noris, M., et al., *Nitric oxide synthesis by cultured endothelial cells is modulated by flow conditions.* Circ Res, 1995. **76**(4): p. 536-43.

165. Frangos, J.A., et al., *Flow effects on prostacyclin production by cultured human endothelial cells.* Science, 1985. **227**(4693): p. 1477-9.

166. Helmlinger, G., B.C. Berk, and R.M. Nerem, *Calcium responses of endothelial cell monolayers subjected to pulsatile and steady laminar flow differ.* Am J Physiol, 1995. **269**(2 Pt 1): p. C367-75.

167. Ishida, T., et al., *Fluid shear stress-mediated signal transduction: how do endothelial cells transduce mechanical force into biological responses?* Ann N Y Acad Sci, 1997. **811**: p. 12-23; discussion 23-4.

168. Sumpio, B.E., et al., *Mechanical stress stimulates aortic endothelial cells to proliferate.* J Vasc Surg, 1987. **6**(3): p. 252-6.

169. Sumpio, B.E., et al., *Alterations in aortic endothelial cell morphology and cytoskeletal protein synthesis during cyclic tensional deformation.* J Vasc Surg, 1988. **7**(1): p. 130-8.

170. Naruse, K. and M. Sokabe, *Involvement of stretch-activated ion channels in Ca2+ mobilization to mechanical stretch in endothelial cells.* Am J Physiol, 1993. **264**(4 Pt 1): p. C1037-44.

171. Iba, T., I. Mills, and B.E. Sumpio, *Intracellular cyclic AMP levels in endothelial cells subjected to cyclic strain in vitro.* J Surg Res, 1992. **52**(6): p. 625-30.

172. Awolesi, M.A., W.C. Sessa, and B.E. Sumpio, *Cyclic strain upregulates nitric oxide synthase in cultured bovine aortic endothelial cells.* J Clin Invest, 1995. **96**(3): p. 1449-54.

173. Wang, D.L., et al., *Mechanical strain increases endothelin-1 gene expression via protein kinase C pathway in human endothelial cells.* J Cell Physiol, 1995. **163**(2): p. 400-6.

174. Carosi, J.A., S.G. Eskin, and L.V. McIntire, *Cyclical strain effects on production of vasoactive materials in cultured endothelial cells.* J Cell Physiol, 1992. **151**(1): p. 29-36.

175. Zhao, S., et al., *Synergistic effects of fluid shear stress and cyclic circumferential stretch on vascular endothelial cell morphology and cytoskeleton.* Arterioscler Thromb Vasc Biol, 1995. **15**(10): p. 1781-6.

176. Shukla, A., et al., *Endothelial cells as mechanical transducers: enzymatic activity and network formation under cyclic strain.* Mech Chem Biosyst, 2004. **1**(4): p. 279-90.

177. Yung, Y.C., et al., *Cyclic tensile strain triggers a sequence of autocrine and paracrine signaling to regulate angiogenic sprouting in human vascular cells.* Proc Natl Acad Sci U S A, 2009. **106**(36): p. 15279-84.

178. LaValley, D.J. and C.A. Reinhart-King, *Matrix stiffening in the formation of blood vessels.* Advances in Regenerative Biology, 2014. **1**(1): p. 25247.

179. Pelham, R.J., Jr. and Y. Wang, *Cell locomotion and focal adhesions are regulated by substrate flexibility.* Proc Natl Acad Sci U S A, 1997. **94**(25): p. 13661-5.

180. Discher, D.E., P. Janmey, and Y.L. Wang, *Tissue cells feel and respond to the stiffness of their substrate.* Science, 2005. **310**(5751): p. 1139-43.

181. Reinhart-King, C.A., M. Dembo, and D.A. Hammer, *Cell-cell mechanical communication through compliant substrates.* Biophys J, 2008. **95**(12): p. 6044-51.

182. Yeh, Y.T., et al., *Matrix stiffness regulates endothelial cell proliferation through septin 9.* PLoS One, 2012. **7**(10): p. e46889.

183. Lo, C.M., et al., *Cell movement is guided by the rigidity of the substrate.* Biophys J, 2000. **79**(1): p. 144-52.

184. Califano, J.P. and C.A. Reinhart-King, *A Balance of Substrate Mechanics and Matrix Chemistry Regulates Endothelial Cell Network Assembly.* Cellular and Molecular Bioengineering, 2008. **1**(2): p. 122.

185. Ingber, D.E. and J. Folkman, *Mechanochemical switching between growth and differentiation during fibroblast growth factor-stimulated angiogenesis in vitro: role of extracellular matrix.* J Cell Biol, 1989. **109**(1): p. 317-30.

186. Joung, I.S., et al., *Cyclic strain modulates tubulogenesis of endothelial cells in a 3D tissue culture model.* Microvasc Res, 2006. **71**(1): p. 1-11.

187. Rosenfeld, D., et al., *Morphogenesis of 3D vascular networks is regulated by tensile forces.* Proc Natl Acad Sci U S A, 2016. **113**(12): p. 3215-20.

188. Hak, D.J., et al., *Delayed union and nonunions: epidemiology, clinical issues, and financial aspects.* Injury, 2014. **45 Suppl 2**: p. S3-7.

189. Grosso, A., et al., *It Takes Two to Tango: Coupling of Angiogenesis and Osteogenesis for Bone Regeneration.* Front Bioeng Biotechnol, 2017. **5**: p. 68.

190. Lv, F.J., et al., *Concise review: the surface markers and identity of human mesenchymal stem cells.* Stem Cells, 2014. **32**(6): p. 1408-19.

191. Morikawa, S., et al., *Abnormalities in pericytes on blood vessels and endothelial sprouts in tumors.* Am J Pathol, 2002. **160**(3): p. 985-1000.

192. Basu, S., et al., *Purification of specific cell population by fluorescence activated cell sorting (FACS).* J Vis Exp, 2010(41).

193. Boerckel, J.D., et al., *Effects of protein dose and delivery system on BMP-mediated bone regeneration.* Biomaterials, 2011. **32**(22): p. 5241-51.

194. Krishnan, L., et al., *Delivery vehicle effects on bone regeneration and heterotopic ossification induced by high dose BMP-2.* Acta Biomater, 2017. **49**: p. 101-112.

195. Nunes, S.S., et al., *Implanted microvessels progress through distinct neovascularization phenotypes.* Microvasc Res, 2010. **79**(1): p. 10-20.

196. Feng, C., et al., *Efficacy and Persistence of Allogeneic Adipose-Derived Mesenchymal Stem Cells Combined with Hyaluronic Acid in Osteoarthritis After Intra-articular Injection in a Sheep Model.* Tissue Eng Part A, 2017.

197. Laschke, M.W., et al., *In vitro osteogenic differentiation of adipose-derived mesenchymal stem cell spheroids impairs their in vivo vascularization capacity inside implanted porous polyurethane scaffolds.* Acta Biomater, 2014. **10**(10): p. 4226-35.

198. Zhao, X., et al., *Three-Dimensional Aggregates Enhance the Therapeutic Effects of Adipose Mesenchymal Stem Cells for Ischemia-Reperfusion Induced Kidney Injury in Rats.* Stem Cells Int, 2016. **2016**: p. 9062638.

199. Baer, P.C., *Adipose-derived mesenchymal stromal/stem cells: An update on their phenotype in vivo and in vitro.* World J Stem Cells, 2014. **6**(3): p. 256-65.

200. Hettiaratchi, M.H., et al., *Competitive Protein Binding Influences Heparin-Based Modulation of Spatial Growth Factor Delivery for Bone Regeneration.* Tissue Eng Part A, 2017. **23**(13-14): p. 683-695.

201. Priddy, L.B., et al., *Oxidized alginate hydrogels for bone morphogenetic protein-2 delivery in long bone defects.* Acta Biomater, 2014. **10**(10): p. 4390-9.

202. Matsubara, H., et al., *Vascular tissues are a primary source of BMP2 expression during bone formation induced by distraction osteogenesis.* Bone, 2012. **51**(1): p. 168-80.

203. Fritz, D.T., et al., *Conservation of Bmp2 post-transcriptional regulatory mechanisms.* J Biol Chem, 2004. **279**(47): p. 48950-8.

204. Li, W.A., et al., *Detection of femtomole quantities of mature cathepsin K with zymography.* Anal Biochem, 2010. **401**(1): p. 91-8.

205. Nauth, A., et al., *Heterotopic ossification in orthopaedic trauma.* J Orthop Trauma, 2012. **26**(12): p. 684-8.

206. Laschke, M.W. and M.D. Menger, *Adipose tissue-derived microvascular fragments: natural vascularization units for regenerative medicine.* Trends Biotechnol, 2015. **33**(8): p. 442-8.

207. Chang, C.C., et al., *Determinants of microvascular network topologies in implanted neovasculatures.* Arterioscler Thromb Vasc Biol, 2012. **32**(1): p. 5-14.

208. Hurtgen, B.J., et al., *Impairment of early fracture healing by skeletal muscle trauma is restored by FK506.* BMC Musculoskelet Disord, 2017. **18**(1): p. 253.

209. Boerckel, J.D., et al., *Effects of in vivo mechanical loading on large bone defect regeneration.* J Orthop Res, 2012. **30**(7): p. 1067-75.

210. Opal, S.M. and V.A. DePalo, *Anti-inflammatory cytokines.* Chest, 2000. **117**(4): p. 1162-72.

211. Gautschi, O.P., S.P. Frey, and R. Zellweger, *Bone morphogenetic proteins in clinical applications.* ANZ J Surg, 2007. **77**(8): p. 626-31.

212. Potter, B.K., et al., *Heterotopic ossification following traumatic and combat-related amputations. Prevalence, risk factors, and preliminary results of excision.* J Bone Joint Surg Am, 2007. **89**(3): p. 476-86.

213. Cipriano, C.A., S.G. Pill, and M.A. Keenan, *Heterotopic ossification following traumatic brain injury and spinal cord injury.* J Am Acad Orthop Surg, 2009. **17**(11): p. 689-97.

214. Jackson, W.M., et al., *Putative heterotopic ossification progenitor cells derived from traumatized muscle.* J Orthop Res, 2009. **27**(12): p. 1645-51.

215. Nair, A.B. and S. Jacob, *A simple practice guide for dose conversion between animals and human.* J Basic Clin Pharm, 2016. **7**(2): p. 27-31.

216. Zara, J.N., et al., *High doses of bone morphogenetic protein 2 induce structurally abnormal bone and inflammation in vivo.* Tissue Eng Part A, 2011. **17**(9-10): p. 1389-99.

217. Utvag, S.E., et al., *Influence of extensive muscle injury on fracture healing in rat tibia.* J Orthop Trauma, 2003. **17**(6): p. 430-5.

218. Nakano, M., et al., *Effect of autotransplantation of microvessel fragments on experimental random-pattern flaps in the rat.* Eur Surg Res, 1998. **30**(3): p. 149-60.

219. Ruehle, M.A., et al., *Decorin-containing collagen hydrogels as dimensionally stable scaffolds to study the effects of compressive mechanical loading on angiogenesis.* MRS Communications, 2017. **7**(3): p. 466-471.

220. Laschke, M.W., et al., *Adipose tissue-derived microvascular fragments from aged donors exhibit an impaired vascularisation capacity.* Eur Cell Mater, 2014. **28**: p. 287-98.

221. Ruehle, M.A., et al., *Aggregate mesenchymal stem cell delivery ameliorates the regenerative niche for muscle repair.* J Tissue Eng Regen Med, 2018.

222. Chien, S., *Effects of disturbed flow on endothelial cells.* Annals of Biomedical Engineering, 2008. **36**(4): p. 554-562.

223. Huang-Lee, L.L., D.T. Cheung, and M.E. Nimni, *Biochemical changes and cytotoxicity associated with the degradation of polymeric glutaraldehyde derived crosslinks.* J Biomed Mater Res, 1990. **24**(9): p. 1185-201.

224. Vogel, K.G. and J.A. Trotter, *The effect of proteoglycans on the morphology of collagen fibrils formed in vitro.* Coll Relat Res, 1987. **7**(2): p. 105-14.

225. Danielson, K.G., et al., *Targeted disruption of decorin leads to abnormal collagen fibril morphology and skin fragility.* J Cell Biol, 1997. **136**(3): p. 729-43.

226. Robinson, P.S., et al., *Influence of decorin and biglycan on mechanical properties of multiple tendons in knockout mice.* J Biomech Eng, 2005. **127**(1): p. 181-5.

227. Pins, G.D., et al., *Self-assembly of collagen fibers. Influence of fibrillar alignment and decorin on mechanical properties.* Biophys J, 1997. **73**(4): p. 2164-72.

228. Reese, S.P., C.J. Underwood, and J.A. Weiss, *Effects of decorin proteoglycan on fibrillogenesis, ultrastructure, and mechanics of type I collagen gels.* Matrix Biol, 2013. **32**(7-8): p. 414-23.

229. Choi, H.U., et al., *Characterization of the dermatan sulfate proteoglycans, DS-PGI and DS-PGII, from bovine articular cartilage and skin isolated by octyl-sepharose chromatography.* J Biol Chem, 1989. **264**(5): p. 2876-84.

230. Davies Cde, L., et al., *Decorin inhibits endothelial migration and tube-like structure formation: role of thrombospondin-1.* Microvasc Res, 2001. **62**(1): p. 26-42.

231. Zhang, Z., et al., *Recombinant Human Decorin Inhibits TGF-b1 Induced Contraction of Collagen Lattice by Keloid Fibroblasts.* Wounds, 2009. **21**(2): p. 47-56.

232. Zhang, Z., et al., *Recombinant human decorin inhibits TGF-beta1-induced contraction of collagen lattice by hypertrophic scar fibroblasts.* Burns, 2009. **35**(4): p. 527-37.

233. Paderi, J.E., et al., *Collagen-binding peptidoglycans: a biomimetic approach to modulate collagen fibrillogenesis for tissue engineering applications.* Tissue Eng Part A, 2009. **15**(10): p. 2991-9.

234. Diamant, J., et al., *Collagen; ultrastructure and its relation to mechanical properties as a function of ageing.* Proc R Soc Lond B Biol Sci, 1972. **180**(1060): p. 293-315.

235. Schonherr, E., et al., *Decorin deficiency leads to impaired angiogenesis in injured mouse cornea.* J Vasc Res, 2004. **41**(6): p. 499-508.

236. Grant, D.S., et al., *Decorin suppresses tumor cell-mediated angiogenesis.* Oncogene, 2002. **21**(31): p. 4765-77.

237. Jarvelainen, H.T., et al., *Expression of decorin by sprouting bovine aortic endothelial cells exhibiting angiogenesis in vitro.* Exp Cell Res, 1992. **203**(2): p. 395-401.

238. Santra, M., et al., *Ectopic decorin expression up-regulates VEGF expression in mouse cerebral endothelial cells via activation of the transcription factors Sp1, HIF1alpha, and Stat3.* J Neurochem, 2008. **105**(2): p. 324-37.

239. Hildebrand, A., et al., *Interaction of the small interstitial proteoglycans biglycan, decorin and fibromodulin with transforming growth factor beta.* Biochem J, 1994. **302 (Pt 2)**: p. 527-34.

240. Ferdous, Z., et al., *Decorin-transforming growth factor- interaction regulates matrix organization and mechanical characteristics of three-dimensional collagen matrices.* J Biol Chem, 2007. **282**(49): p. 35887-98.

241. Krishnan, L., N.J. Willett, and R.E. Guldberg, *Vascularization strategies for bone regeneration.* Ann Biomed Eng, 2014. **42**(2): p. 432-44.

242. Park, J.Y., et al., *3D printing technology to control BMP-2 and VEGF delivery spatially and temporally to promote large-volume bone regeneration.* Journal of Materials Chemistry B, 2015. **3**(27): p. 5415-5425.

243. Matuszewski, P.E., et al., *Regional variation in human supraspinatus tendon proteoglycans: decorin, biglycan, and aggrecan.* Connect Tissue Res, 2012. **53**(5): p. 343-8.

244. Sarkar, M.R., et al., *Bone formation in a long bone defect model using a platelet-rich plasma-loaded collagen scaffold.* Biomaterials, 2006. **27**(9): p. 1817-23.

245. Uhrig, B.A., et al., *Recovery from hind limb ischemia enhances rhBMP-2-mediated segmental bone defect repair in a rat composite injury model.* Bone, 2013. **55**(2): p. 410-7.

246. Allen, A.B., et al., *In vivo bioluminescent tracking of mesenchymal stem cells within large hydrogel constructs.* Tissue Eng Part C Methods, 2014. **20**(10): p. 806-16.

247. Raida, M., et al., *Role of bone morphogenetic protein 2 in the crosstalk between endothelial progenitor cells and mesenchymal stem cells.* Int J Mol Med, 2006. **18**(4): p. 735-9.

248. Finkenzeller, G., S. Hager, and G.B. Stark, *Effects of bone morphogenetic protein 2 on human umbilical vein endothelial cells.* Microvasc Res, 2012. **84**(1): p. 81-5.

249. Fiedler, L.R. and J.A. Eble, *Decorin regulates endothelial cell-matrix interactions during angiogenesis.* Cell Adh Migr, 2009. **3**(1): p. 3-6.

250. Jarvelainen, H., A. Sainio, and T.N. Wight, *Pivotal role for decorin in angiogenesis.* Matrix Biol, 2015. **43**: p. 15-26.

251. Schonherr, E., et al., *Paracrine or virus-mediated induction of decorin expression by endothelial cells contributes to tube formation and prevention of apoptosis in collagen lattices.* Eur J Cell Biol, 1999. **78**(1): p. 44-55.

252. Tonnesen, M.G., X. Feng, and R.A. Clark, *Angiogenesis in wound healing.* J Investig Dermatol Symp Proc, 2000. **5**(1): p. 40-6.

253. Barrientos, S., et al., *Clinical application of growth factors and cytokines in wound healing.* Wound Repair Regen, 2014. **22**(5): p. 569-78.

254. Jung, H.J., M.B. Fisher, and S.L. Woo, *Role of biomechanics in the understanding of normal, injured, and healing ligaments and tendons.* Sports Med Arthrosc Rehabil Ther Technol, 2009. **1**(1): p. 9.

255. Nelson, E.A. and S.E. Bell-Syer, *Compression for preventing recurrence of venous ulcers.* Cochrane Database Syst Rev, 2014(9): p. CD002303.

256. Barnes, L.A., et al., *Mechanical Forces in Cutaneous Wound Healing: Emerging Therapies to Minimize Scar Formation.* Adv Wound Care (New Rochelle), 2018. **7**(2): p. 47-56.

257. Gerhardt, H., et al., *VEGF guides angiogenic sprouting utilizing endothelial tip cell filopodia.* J Cell Biol, 2003. **161**(6): p. 1163-77.

258. Wang, S., et al., *Intercellular Tension Negatively Regulates Angiogenic Sprouting of Endothelial Tip Cells via Notch1-Dll4 Signaling.* Adv Biosyst, 2017. **1**(1-2).

259. Loerakker, S., et al., *Mechanosensitivity of Jagged-Notch signaling can induce a switch-type behavior in vascular homeostasis.* Proc Natl Acad Sci U S A, 2018. **115**(16): p. E3682-E3691.

260. Dao Thi, M.U., et al., *Investigating metalloproteinases MMP-2 and MMP-9 mechanosensitivity to feedback loops involved in the regulation of in vitro angiogenesis by endogenous mechanical stresses.* Acta Biotheor, 2012. **60**(1-2): p. 21-40.

261. Haage, A., et al., *Matrix metalloproteinase-14 is a mechanically regulated activator of secreted MMPs and invasion.* Biochem Biophys Res Commun, 2014. **450**(1): p. 213-8.

262. Alenghat, F.J. and D.E. Ingber, *Mechanotransduction: all signals point to cytoskeleton, matrix, and integrins.* Sci STKE, 2002. **2002**(119): p. pe6.

263. Wang, K.C., et al., *Flow-dependent YAP/TAZ activities regulate endothelial phenotypes and atherosclerosis.* Proc Natl Acad Sci U S A, 2016. **113**(41): p. 11525-11530.

264. Wang, X., et al., *YAP/TAZ Orchestrate VEGF Signaling during Developmental Angiogenesis.* Dev Cell, 2017. **42**(5): p. 462-478 e7.

265. Mason, D.E., et al., *YAP and TAZ limit cytoskeletal and focal adhesion maturation to enable persistent cell motility.* J Cell Biol, 2019.

266. Kim, J., et al., *YAP/TAZ regulates sprouting angiogenesis and vascular barrier maturation.* J Clin Invest, 2017. **127**(9): p. 3441-3461.

267. Claes, L., et al., *The mode of interfragmentary movement affects bone formation and revascularization after callus distraction.* PLoS One, 2018. **13**(8): p. e0202702.

268. Prendergast, P., R. Huiskes, and K. Søballe, *Biophysical stimuli on cells during tissue differentiation at implant interfaces.* Journal of biomechanics, 1997. **30**(6): p. 539-548.

269. McDaniel, J.S., et al., *Characterization and multilineage potential of cells derived from isolated microvascular fragments.* J Surg Res, 2014. **192**(1): p. 214-22.

270. Wang, Y., A. Narayanaswamy, and B. Roysam. *Novel 4-D open-curve active contour and curve completion approach for automated tree structure extraction*. in *CVPR 2011*. 2011. IEEE.

271. Luisi, J., et al., *The FARSIGHT trace editor: an open source tool for 3-D inspection and efficient pattern analysis aided editing of automated neuronal reconstructions.* Neuroinformatics, 2011. **9**(2-3): p. 305-15.

272. Reese, S.P., et al., *Nanoscale Imaging of Collagen Gels with Focused Ion Beam Milling and Scanning Electron Microscopy.* Biophys J, 2016. **111**(8): p. 1797-1804.

273. Moser, B., et al., *Fluorescence colocalization microscopy analysis can be improved by combining object-recognition with pixel-intensity-correlation.* Biotechnol J, 2017. **12**(1).

274. Weinstock, L., et al., *Fingolimod Phosphate Inhibits Astrocyte Inflammatory Activity in Mucolipidosis IV.* Hum Mol Genet, 2018.

275. Liu-Chittenden, Y., et al., *Genetic and pharmacological disruption of the TEAD-YAP complex suppresses the oncogenic activity of YAP.* Genes Dev, 2012. **26**(12): p. 1300-5.

276. Zhao, B., et al., *TEAD mediates YAP-dependent gene induction and growth control.* Genes Dev, 2008. **22**(14): p. 1962-71.

277. Strasser, G.A., J.S. Kaminker, and M. Tessier-Lavigne, *Microarray analysis of retinal endothelial tip cells identifies CXCR4 as a mediator of tip cell morphology and branching.* Blood, 2010. **115**(24): p. 5102-10.

278. Brew, K. and H. Nagase, *The tissue inhibitors of metalloproteinases (TIMPs): an ancient family with structural and functional diversity.* Biochim Biophys Acta, 2010. **1803**(1): p. 55-71.

279. Plank, M.J., B.D. Sleeman, and P.F. Jones, *A mathematical model of tumour angiogenesis, regulated by vascular endothelial growth factor and the angiopoietins.* J Theor Biol, 2004. **229**(4): p. 435-54.

280. Eswarappa, S.M., et al., *Programmed translational readthrough generates antiangiogenic VEGF-Ax.* Cell, 2014. **157**(7): p. 1605-18.

281. Perlman, H., et al., *An elevated bax/bcl-2 ratio corresponds with the onset of prostate epithelial cell apoptosis.* Cell Death Differ, 1999. **6**(1): p. 48-54.

282. Carlson, T.R., et al., *Cell-autonomous requirement for beta1 integrin in endothelial cell adhesion, migration and survival during angiogenesis in mice.* Development, 2008. **135**(12): p. 2193-202.

283. Raines, E.W., *The extracellular matrix can regulate vascular cell migration, proliferation, and survival: relationships to vascular disease.* International journal of experimental pathology, 2000. **81**(3): p. 173-182.

284. Fiedler, L., et al., *Decorin regulates endothelial cell motility on collagen I through activation of insulin-like growth factor I receptor and modulation of a2b1 integrin activity.* J Biol Chem, 2008. **283**: p. 17406-17415.

285. Brigstock, D.R., *Regulation of angiogenesis and endothelial cell function by connective tissue growth factor (CTGF) and cysteine-rich 61 (CYR61).* Angiogenesis, 2002. **5**(3): p. 153-65.

286. Pearson, H.B., et al., *Effects of BMP-2 on neovascularization during large bone defect regeneration.* Tissue Eng Part A, 2019.

287. Hettiaratchi, M.H., et al., *Enhanced in vivo retention of low dose BMP-2 via heparin microparticle delivery does not accelerate bone healing in a critically sized femoral defect.* Acta Biomater, 2017. **59**: p. 21-32.

288. Brodowska, K., et al., *The clinically used photosensitizer Verteporfin (VP) inhibits YAP-TEAD and human retinoblastoma cell growth in vitro without light activation.* Exp Eye Res, 2014. **124**: p. 67-73.

289. Spiller, K.L., et al., *The role of macrophage phenotype in vascularization of tissue engineering scaffolds.* Biomaterials, 2014. **35**(15): p. 4477-88.